The Aerodynamics of Bird Flight

by David Michael Kaplan

AERODYNAMICS OF BIRD FLIGHT

A Thesis

Presented to the Faculty of the Graduate School

of Cornell University

in Partial Fulfillment of the Requirements for the Degree of

Master of Science

by

David Michael Kaplan

August 2010

ABSTRACT

We investigate methods for physically-based simulation of aerodynamic forces acting on a flapping bird in free-flight. We make use of two previous studies as the basis for our work; Jeffery Wang's digital Ivory-billed woodpecker model, and Brendan Holt's high-speed kinematic motion capture data of a Red-winged blackbird (*Agelaius phoeniceus*) in free flight. These studies provide an extensive framework in which to model a high-resolution, morphologically accurate Red-winged blackbird, which we animate to undergo a physically accurate wingbeat motion. To complete the geometric picture, we laser scan individual feathers to obtain the complete wing geometry. Adapting the detailed character rig of the Ivory-billed woodpecker to suit the smaller Red-winged blackbird, motion picture techniques allow us to pose and animate the digital bird to match the motion captured joint kinematics. Several methods of aerodynamic simulation were considered, including wind tunnel testing and computational fluid dynamics (CFD), before ultimately implementing a quasi-steady blade element model. Performing aerodynamic simulations on this animated mesh yields forces on the bird which support the validity of the model. Although the model is unable to account for the entire weight of the bird, it is within the bounds of error and provides an interactive first order estimate.

BIOGRAPHICAL SKETCH

David Kaplan was born on April 3rd 1984 and grew up in Needham, Massachusetts. He attended high school at Concord Academy in Concord, Massachusetts. He was accepted to the University of Colorado at Boulder, and studied aerospace engineering there for one year before transferring to Cornell University in the fall of 2003. He graduated from Cornell University with a B.S. in Mechanical and Aerospace Engineering in May of 2006. He joined the Program of Computer Graphics in September of 2006.

ACKNOWLEDGEMENTS

I would like to thank Don Greenberg above all others for making this work possible. It is Don's addiction to invention and his deep faith in the power of combining disciplines that has spurred his years of research and keeps him going still. His keen academic, political, and administrative prowess, made the Ivory-billed woodpecker project a reality and paved the way for this work and others.

Don and I share many things including a background in mechanical engineering, attention to design, a love for the outdoors, and a belief in the power of storytelling. One thing we do not share, however, is a common sense of timing. I thank him sincerely for bearing with my latent sense of direction and supporting me though continually delayed progress.

In the fall of 2004 I joined a group of misfits competing in the DARPA Grand Challenge, advised by Mechanical Engineering professor Ephrahim Garcia. Since that project Garcia and I have stayed in touch, and he was the only person I considered when looking for a minor advisor. I thank him for his candor and humor.

Thanks to my fellow masters students: Brendan Holt, Todd Harvey, and Konstantin Shkurko. Brendan somehow managed to complete his degree only one year tardy. While Todd and I toiled on, and Konstantin came aboard. Just recently Konstantin finished his work, and he and Brendan are off to embark on different Ph.D. programs and I wish them well. Todd, good luck completing your impressive thesis and I'm sure you will find what you are looking for either in the visual effects industry or in academia.

Thanks also to Kimberly Bostwick and the Cornell Laboratory of Ornithology. Kim's eagerness to collaborate made Brendan's thesis a reality.

I am grateful to the entire Program of Computer Graphics for its support. Hurf

Sheldon's open door across the hallway has been the source of many memorable conversations. Linda Stephenson and Peggy Andersen keep the lab running, and I appreciate all of their hard work. Jeff Wang, now animating pandas and dragons at DreamWorks Animation, was my TA and colleague, and I am grateful for his Ivory-billed woodpecker (still extinct) project, for teaching me animation, and for helping us to teach animation. Thanks also to Steve Marschner, Doug James, Jane Wang, Jon Moon, Jaroslav Krivanek, Wenzel Jakob, Jeff Budsberg, Nasheet Zaman, Fola Akinola, and Martin Berggren.

Thank you to all my friends who have lived with me in the house at 204 Delaware, especially Pete Moran. Pete has been a wonderful friend and I wish him luck as he begins an M.F.A. program next year in New Haven. Sorry for leaving so many dishes in the sink. Thanks also to Aaron, Brian, Noah, Frank, and Christian. Finally, thanks to Kristine Heiney for being my companion this year.

Thanks to all my friends at the Appalachian Mountain Club and everyone I met through Cornell Outdoor Education. Thank you to my parents, Steve and Erica, for fostering in me a love of science, math, and art, and for supporting me through this endeavor.

This research was funded by the Program of Computer Graphics, the Department of Architecture, and the Department of Computer Science at Cornell University, and the National Science Foundation ITR/AP CCF-0205438.

CONTENTS

LIST OF TABLES

LIST OF FIGURES

CHAPTER 1

INTRODUCTION

Modeling bird flight is a complex and challenging problem, and one that has intrigued researchers for years. Understanding how birds fly carries with it important implications including insight into the basic nature of fluid flow, as well as the potential to vastly increase the efficiency of powered flight. The study of bird flight is unique in that it spans several disciplines, and draws from many bodies of knowledge. Specifically, our study depended on the relationship between ornithology, aerospace engineering, and computer graphics.

As a primarily observational biological science, ornithology covers topics including avian anatomy and physiology. The biological community has documented and characterized flapping bird flight in great detail, including studies investigating such phenomena as neuromuscular impulses, joint kinematics, and wake vortices. However, little emphasis has been placed on creating an aerodynamic model of flight from these studies.

Aerospace engineering, which applies the concepts of fluid mechanics to flight, focuses primarily on developing simulation methods and simulating the flow of air around wings to compute forces. Most aerodynamic studies have not traditionally been concerned with deforming or flapping wings, instead devoting resources to optimizing fixed-wing studies in steady-state conditions. Furthermore, much of the research has been conducted on relatively simple geometries.

Both of these disciplines, ornithology and aerospace engineering, can leverage the strengths of the other to simulate bird flight. The discipline which enables prior research from these two diverse communities to be combined, the one which makes our study possible, is computer graphics. Historically motivated by the motion picture industry, computer graphics provides techniques for motion capture

of moving bodies as well as a vital framework for manipulating complex geometric data.

Our goal is to predict the aerodynamic forces on a flapping bird wing. We start in Chapter 2 by reviewing key concepts in aerodynamics, as well as ornithological terminology. Chapter 3 summarizes previous studies of bird flight from both the biological and engineering fields, including an important study by Jia-chi Wu and Zoran Popovic entitled "Realistic Modeling of Bird Flight Animations" [WP03]. In this study, Wu and Popovic created a kinematic model with accurate degrees of freedom and represented each feather as a single polygon. Given a predetermined flight path, they applied a blade element model with arbitrary parameters, and were able to create very visually realistic results. We try to improve upon this approach by constructing a virtual bird from scientifically-measured high resolution geometry, and implement a blade element model which has been experimentally vetted. We can validate our model by comparing the lift force predicted with the weight of the bird.

Chapter 4 describes the process of creating the geometric model, including the laser scanning of feathers. We build on two excellent recently-completed studies to construct our model. The first work is a morphologically accurate and animatable computer generated bird created by Jeffery Wang [Wan07]. This model gives an anatomic framework for a bird's geometry and a physiologically-based joint rig with which to pose and animate the model. Second, we make use of Brendan Holt's recent high-speed motion capture study of a Red-winged blackbird's (*Agelaius phoeniceus*) wingbeat [Hol09]. Wang's and Holt's work naturally complement each other, and we utilize them to illustrate how the geometry of a Red-winged blackbird's wing deforms during a wingbeat.

Chapter 5 explores the aerodynamic simulation methods considered. Compu-

tational fluid dynamics and wind tunnel testing were both considered before a quasi-numeric blade element approach was adopted. We derive a force model and explain how appropriate coefficients are chosen. Chapter 6 presents the results of using this model to simulate the wingbeat constructed in Chapter 4. We conclude with Chapter 7 which discusses the validity of the model and proposes future improvements.

CHAPTER 2

BACKGROUND

In this chapter we will review the two disciplines on which our study is built; Aerospace engineering, and ornithology. Aerospace engineering is reviewed in two sections. The first section focuses on the basics of fluid mechanics and how fluid behaves. The second section reviews aerodynamics, which is the study of fluid dynamics as applied to wings and the forces generated on wings. Finally, the third section of this chapter draws from ornithology and biology to detail avian anatomy.

2.1 Fluid Mechanics

It is important to have a working vocabulary and understanding of the terms and variables used in aerodynamics. Because aerodynamics is built on the foundation of fluid mechanics we will briefly review some basic fluid dynamic principles in order to better understand aerodynamic models and how they apply to animal flight.

2.1.1 Terms and Definitions

For the study of aerodynamics, velocity and pressure are the two most important fluid properties. Velocity is a term which is comprised of a unit vector and a magnitude, and indicates the speed and direction of an infinitesimal fluid element. Pressure is defined as a force per unit area, and is roughly a measure of the intensity with which the fluid molecules are moving and colliding with each other. Pressure is a scalar and exerts a force normal to an external object.

According to the laws of solid mechanics, when pressure is exerted on a differential element by neighboring elements, a tensile or compressive stress is created in the element. A shear stress can also exist on a differential element when a force

parallel to a boundary, instead of normal to it, is applied. In two dimensions this causes a rectangular element to deform into a parallelogram. These stresses exists not only in solid elements, but in fluid ones. When two differential fluid elements move in any direction which is not directly toward or away from each other, a shear is created. If this occurs near the boundary with an external object, a shear force will be exerted on that object. Just as fluid pressure exerts a force on an object normal to the boundary, fluid shear exerts a force which is parallel to the boundary.

Together, pressure and shear stress are solely responsible for all external fluid forces on objects. Lift and drag and any other forces which are said to be caused by fluid interaction are simply decompositions of the force resulting from the integral of the pressure and shear stresses over a boundary.

2.1.2 Reynolds Number

Fluid flow is a particularly challenging problem because the nature of fluid changes depending on the scale on which it acts. Fluid has a viscosity which tends to resist motion and damp out nonuniform velocities. The degree of viscosity and the size of any objects interacting with the flow greatly influences how the fluid behaves. To a very small object in air such as a bacteria or the wing of a fruit fly, the viscous forces are dominant and moving through the air at this scale can be likened to swimming through honey. Conversely, a very large object such as a Boeing 747 jetliner exhibits none of this type of motion-impeding friction, the dominant resistance from the air on a large body is not viscous but inertial as the body must push a relatively larger mass of air out of its way. To quantify this behavior, we use the dimensionless Reynold's number (Re). The Reynold's number is a ratio of the inertial to viscous forces in the fluid, and indicates the

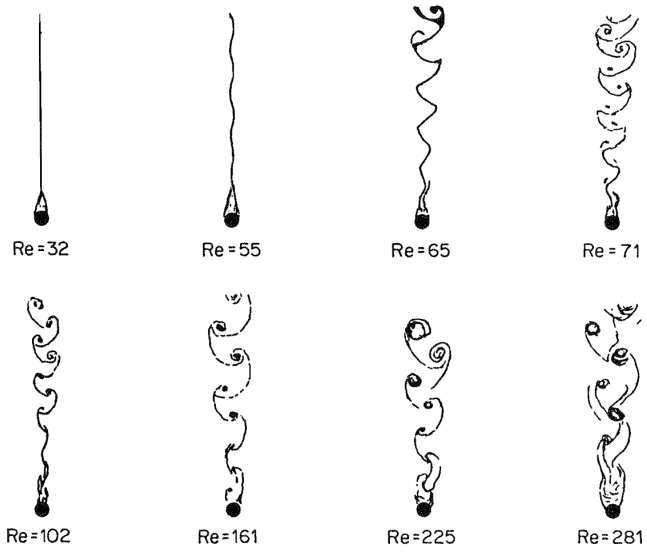

Figure 2.1: Streaklines indicate how fluid behaves as it flows past a cylinder at increasing Reynold's numbers; showing laminar flow in the first two cases and then a transition to turbulent flow and vortex shedding.[WS84]

smoothness or turbulence of the flow. It is defined as:

$$Re = \frac{\rho U l}{\mu} \tag{2.1}$$

Here, ρ is the density of the fluid, U is the velocity of the flow, l is the characteristic length of the object of interest, and μ is the dynamic viscosity of the fluid. This type of dimensionless analysis is extremely useful as it allows us to conduct similar experiments in different fluids or on different scales.

Low Reynold's numbers indicate that the flow is smooth, or laminar. Laminar flow is a distinct regime of fluid flow where the streamlines of fluid are all parallel and there is little disruption. As the Reynold's number increases beyond laminar flow, there is a transition to turbulent flow. Rough or turbulent flow is characterized by chaotic swirling vortices. Turbulent flow is generally recognized as $Re \gtrsim 10^4$. The exact limits of the laminar and turbulent regimes vary depending on additional conditions. For example, fluid flow in a smooth pipe will remain

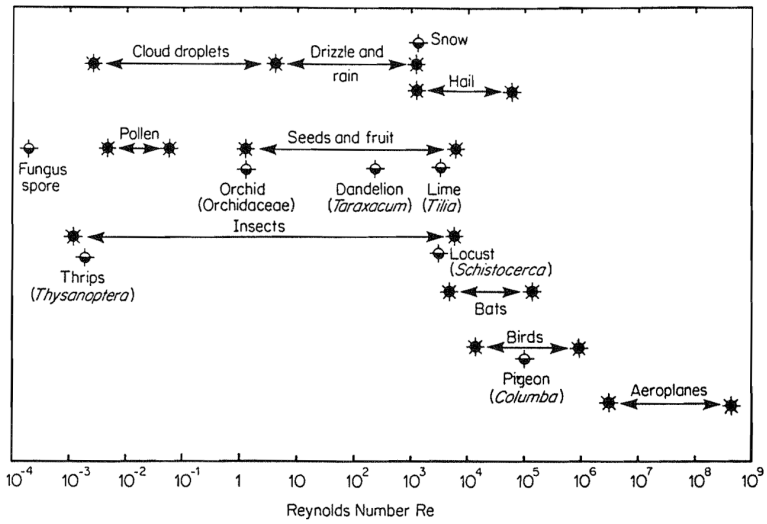

Figure 2.2: The domain of Reynold's Numbers relevant to locomotion through air. The ranges of flying organisms as well as some inanimate objects are plotted with respect to their Reynold's Numbers. [WS84]

laminar into higher Reynold's numbers, while the rough laces of a rotating baseball are designed to induce turbulent flow at lower Reynold's numbers.

Figure 2.2 shows the ranges of Reynold's numbers of insects, bats, birds, and airplanes along with several other objects. As we can see, insect flight spans many orders of magnitude of Reynold's numbers. Nearly all insect species, except for the Hawkmoth with its large wings, fly neatly in the regime of laminar flow. Airplanes operate under the turbulent conditions of high Reynold's number flight. Bird flight falls between these ranges, existing at Reynold's numbers between roughly 10^4 and 10^6. Hummingbirds and small songbirds represent the lower boundary, and large gliding birds such as eagles, hawks, and gulls represent the upper boundary. It is clear that a transition from the laminar to turbulent flow must occur somewhere in the range of bird flight. Contrary to classical aerodynamics however, this break is not abrupt and birds do not fall neatly into one category or the other. While a hummingbird has similar wing shape and kinematics to many insects, and a

soaring gull flies much the same as an airplane does, nearly all birds demonstrate some flight characteristics of both regimes, and are difficult to classify. This is one of the major factors which makes studying bird flight so difficult, as it is unclear what assumptions, about Reynold's number regime are valid.

2.1.3 Navier-Stokes Equation

The Navier-Stokes equation is the governing equation of all fluid flow (Equation 2.2). The formula is born out of the continuity constraint, that mass must be conserved, and the momentum constraint which applies Newton's second law to fluids. Its derivation is covered in many texts [And01, Whi02, Sed65, KBD35]. It often has no analytic solution because it is non-linear, but it provides the basis for numerical solutions.

$$\frac{\partial \boldsymbol{V}}{\partial t} + \boldsymbol{V} \cdot \nabla \boldsymbol{V} = -\nabla \boldsymbol{p} + \mu \nabla^2 \boldsymbol{V} + \rho \boldsymbol{g} \tag{2.2}$$

Here, $\boldsymbol{V}$ is the velocity field, $\boldsymbol{p}$ is the pressure field, $\boldsymbol{g}$ is the acceleration due to gravity, and the constants ρ and μ are the density and dynamic viscosity of the fluid, respectively.

2.1.4 Circulation and Vorticity

Both laminar and turbulent flows are subject to swirls, eddies, and vortices as the flow interacts with objects. These transient artifacts can become important elements of the flow. Many wings are able to take advantage of these dynamic elements. In order to measure the vorticity ξ of a fluid field, we take the curl of the velocity field.

$$\xi = \nabla \times \mathbf{V} \tag{2.3}$$

Vorticity however only gives us a quantification of the flow's rotation at an infinitesimal point. To consider a broader volume, such as the rotation around a wing, we introduce the circulation Γ:

$$\Gamma = \oint \mathbf{V} \cdot d\mathbf{s} \tag{2.4}$$

Here, $\boldsymbol{s}$ denotes the surface of the body. Thus, the closed line integral of the dot product of the velocity and the the surface normal gives the circulation. In three dimensions, this becomes:

$$\Gamma = \oint \xi \cdot d\mathbf{A} = \oiint (\nabla \times \mathbf{V}) \cdot d\mathbf{A} \tag{2.5}$$

Circulation is an important concept because it can be used to calculate the lift on a wing. Often circulation is impossible to measure, but in the cases where it is measurable it leads to direct knowledge of the upward force on a body.

2.1.5 Boundary Layers

The last important fluid dynamics concept to review is the boundary layer. Whether the flow is of high or low Reynold's number, a boundary layer always exists between the fluid and a solid object. Far from the object, the fluid moves with a constant velocity known as the free-stream velocity, which is often notated as U_∞ or V_∞. However, close to the object the fluid will move slower due to the viscous effects of the fluid interacting with the solid wall. This phenomenon, first discovered by Ludwig Prandtl in 1904, is known as the *no-slip condition.*

The no-slip condition states that every infinitesimal fluid element in contact with a boundary must move with the same velocity as that boundary due to

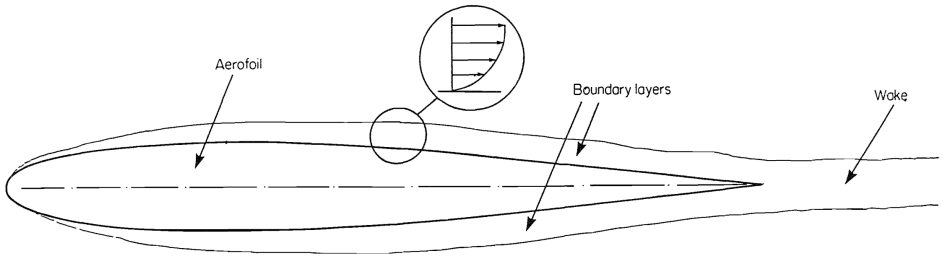

Figure 2.3: Boundary layer around an airfoil showing the velocity profile within the boundary layer and the thickness of the boundary layer itself.[WS84]

friction. In a reference frame where the object is stationary and the fluid is moving, the velocity of the fluid will be zero along the boundary with the object. How quickly the velocity returns to the free stream velocity as one moves away from the wall depends on many factors, but is known as the *boundary layer thickness* (δ). The boundary layer is generally recognized to extend from the object to the point at which the fluid velocity is moving at ninety-nine percent of the free-stream velocity. This distance defines the thickness of the boundary layer. The boundary layer is generally very thin when compared to the scale of the body creating the boundary. Figure 2.3 illustrates the boundary layer around an airfoil. The magnified portion shows the velocity profile inside the boundary layer.

2.2 Aerodynamics

Aerodynamics is the branch of fluid mechanics concerned with the dynamics of air around free moving bodies. Aerodynamics often focuses on the airfoil as the object of interest, as airfoils are highly efficient at generating forces. In this section we will introduce the terminology and concepts of airfoils, and the basic model for describing the aerodynamic forces which act on an airfoil.

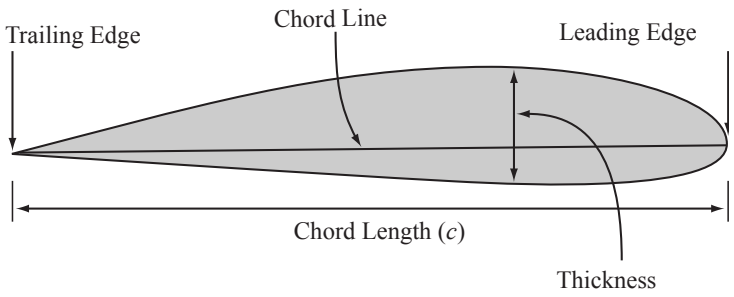

Figure 2.4: Airfoil Terminology

2.2.1 Nomenclature

Airfoils are the fundamental two-dimensional cross sections of rigid body aerodynamics. Figure 2.4 shows a sample airfoil and its labeled properties. The leading edge and trailing edge are the most forward and rearward points on the airfoil, respectively. The chord line connects the two edges, and has a chord length c. The chord is an approximate measure of the length of the wing. Span is the term which indicates the width of the wing (i.e. out of the page), if the wing is three-dimensional. The shape of a three dimensional wing from the top is known as the planform. The planform area gives the area of the wing. For a rectangular wing the planform area is the chord multiplied by the span. Airfoils can also have a degree of camber, which indicates the amount of bend of the airfoil. Airfoils with zero camber are symmetric.

2.2.2 The Kutta Condition

One of the properties of airfoils which makes them so efficient at generating lift is the sharp and tapered trailing edge. This has the effect of causing circulation which increases lift. Figure 2.5 demonstrates this phenomenon. The upper left airfoil in the figure is moving through a velocity field with no circulation. Here, we note the stagnation points, points on a body where the velocity is zero. These are the

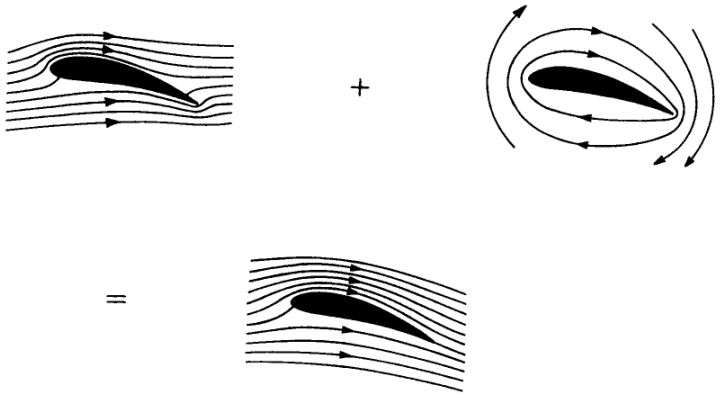

Figure 2.5: Flow with no circulation (upper left) added to pure circulation (upper right) results in a flowfield around an airfoil which satisfies the Kutta condition of moving the rear stagnation point to the trailing edge (bottom).[Ell84e]

points where the streamlines appear to intersect the airfoil, either because the flow is splitting to go over the top and bottom surfaces at the leading edge, or because it is rejoining at the trailing edge. In the upper left figure, the rear stagnation point is on the top surface of the airfoil, a near physical impossibility. The upper right airfoil in the figure shows the effect that circulation has on the flow. In this case, it adds a clockwise rotation to the flow and moves the rear stagnation point toward the trailing edge. The bottom airfoil in the figure illustrates the result of the summed uniform and circulating flows, moving the stagnation points to their proper locations.

This circulation illustrates the Kutta condition. Proposed by Martin Wilhelm Kutta in the early twentieth century, the observation states that bodies with sharp trailing edges will develop exactly enough circulation to move the rear stagnation point to the trailing edge. This requires artificial circulation be imposed on simulations in order to move the stagnation points on a body to their known locations.

Following the Kutta condition, the Kutta-Joukowski theorem (Equation 2.6) states that the lift force acting on a body is proportional to the circulation and

free stream velocity. Thus, greater circulation creates greater lift.

$$L = \rho U_\infty \Gamma \tag{2.6}$$

2.2.3 Steady State Aerodynamics

With an understanding of how fluid flows around an airfoil, we can now examine how forces develop on an airfoil. The net force on any body is found by integrating the pressure around the airfoil with respect to the differential surface length or area. By integrating the pressure around the boundary of an airfoil, we determine the net force acting at a point known as the center of pressure. Figure 2.6 shows a typical pressure profile around an airfoil. Force due to pressure always acts normal to the boundary. The figure shows the net forces from the top and bottom surfaces, F_1 and F_2 respectively. The points 1 and 2 at which these forces act, known as the centers of pressure, indicate the location at which the integrated force acts with no moment. By convention, the moment acting on an airfoil is taken about the quarter-chord point. Therefore, unless points 1 and 2 in the figure are coincident, there will be a net moment on this airfoil.

Figure 2.7 shows the same concept but with magnitude of pressure plotted versus chord position for the top and bottom surfaces. In this example, the pressures are first differenced with the pressure of still air, known as the far-field pressure. In this way, the pressure on the top surface of the airfoil becomes negative across most of its length, and the pressure on the bottom surface mostly positive. This leads to a net upward force on the airfoil.

The force resulting from the pressure distribution on an airfoil can be understood by decomposing that force into orthogonal components. Figure 2.8 shows an airfoil illustrating the geometric relationship between the relevant aerodynamic

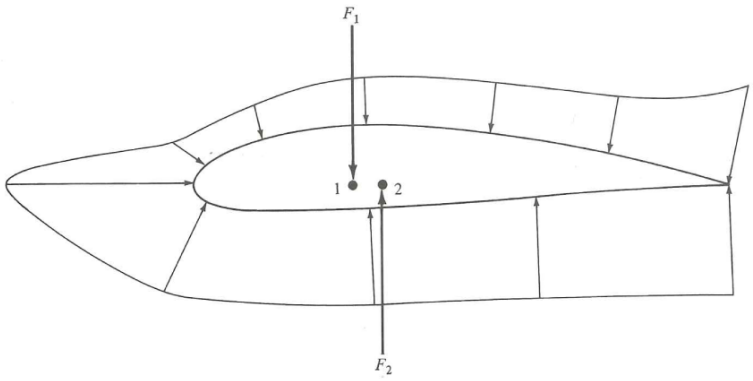

Figure 2.6: Pressure profile on an airfoil. F_1 represents the force due to pressure on the top surface, and F_2 represents force due to pressure on the bottom surface. Points 1 and 2 represent the centers of pressure about which each force acts with no moment. [And00]

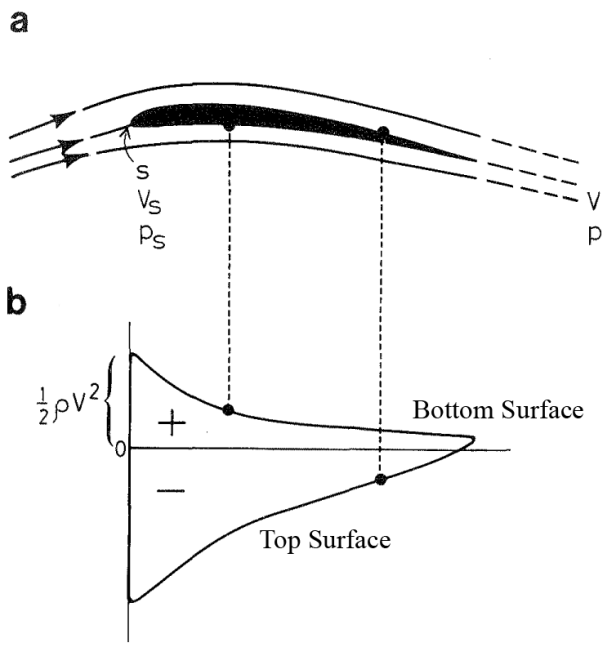

Figure 2.7: A graphical representation of the pressures on the top and bottom surface of an airfoil, plotted against the horizontal position. The pressures indicated here are relative to some far-field pressure p_∞. [Nor90]

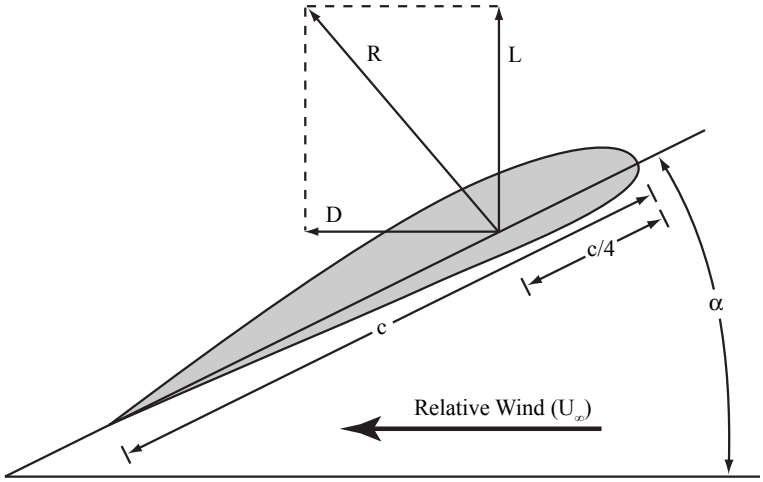

Figure 2.8: Angle of attack and force decomposition on an airfoil

terms. The free stream velocity is given as U_∞. The angle of attack α is the angle between the airfoil chord c and the relative wind. The total force on the airfoil is given by the total force vector R. R can be understood by decomposing it into components of lift L and drag D. Lift acts normal to the relative wind, and drag acts in the direction of relative wind. There can also be a moment about the airfoil which torques the wing. By convention, the forces and moment are all taken to act about the quarter-chord point, as indicated in the figure. The projection of the resultant force R to its lift and drag components is given in Equations 2.7.

$$\begin{aligned} L &= R\cos\alpha \\ D &= R\sin\alpha \end{aligned} \tag{2.7}$$

When measuring the lift and drag forces on an airfoil, it is often convenient to non-dimensionalize these forces. By creating non-dimensional lift and drag terms, these terms become independent of factors such as air density, airspeed, and wing planform area. These non-dimensional terms, the coefficient of lift C_L and coefficient of drag C_D, allow an easy reference of airfoil performance without

specifying speed, wing size, or altitude (density). The equations for coefficient of lift and drag are shown in Equations 2.8 and 2.9. Here, ρ is the density of the fluid (assumed to be incompressible and therefore constant), U is the free stream velocity, L and D are the lift and drag forces respectively at a particular angle of attack, and A is the planform area. This is the two-dimensional form of the equation; in three dimensions the chord length c is replaced by the area A.

$$C_L = \frac{L}{\frac{1}{2}\rho U^2 c} \tag{2.8}$$

$$C_D = \frac{L}{\frac{1}{2}\rho U^2 c} \tag{2.9}$$

This allows coefficients of lift and drag to be calculated for a given airfoil as solely a function of angle of attack. Figure 2.9 shows a sample section lift coefficient curve. The airfoil here is the NACA 2412 section, a particular airfoil shape. In the lower angles of attack, the airfoil is well behaved and flow stays laminar and attached to the boundary. However, at high angles of attack airfoils exhibit a behavior known as *stall* when the boundary layer separates turbulently from the top surface causing a sharp decrease in lift. This airfoil stalls around sixteen degrees angle of attack. The more turbulent a flow or the higher the Reynold's Number, the more likely boundary layer separation is to occur. A separated boundary layer causes much higher drag on the object due to the higher shear stresses created. For this reason, it is highly undesirable. High Reynold's numbers and high angles of attack are the most likely causes of boundary layer separation. Note that as with most airfoil studies, data is only taken between the two stall points, in this case roughly negative and positive twenty degrees. Once an airfoil stalls it is not operating in its useful flight range, and therefore data at high angles of attack are not relevant to fixed wing flight.

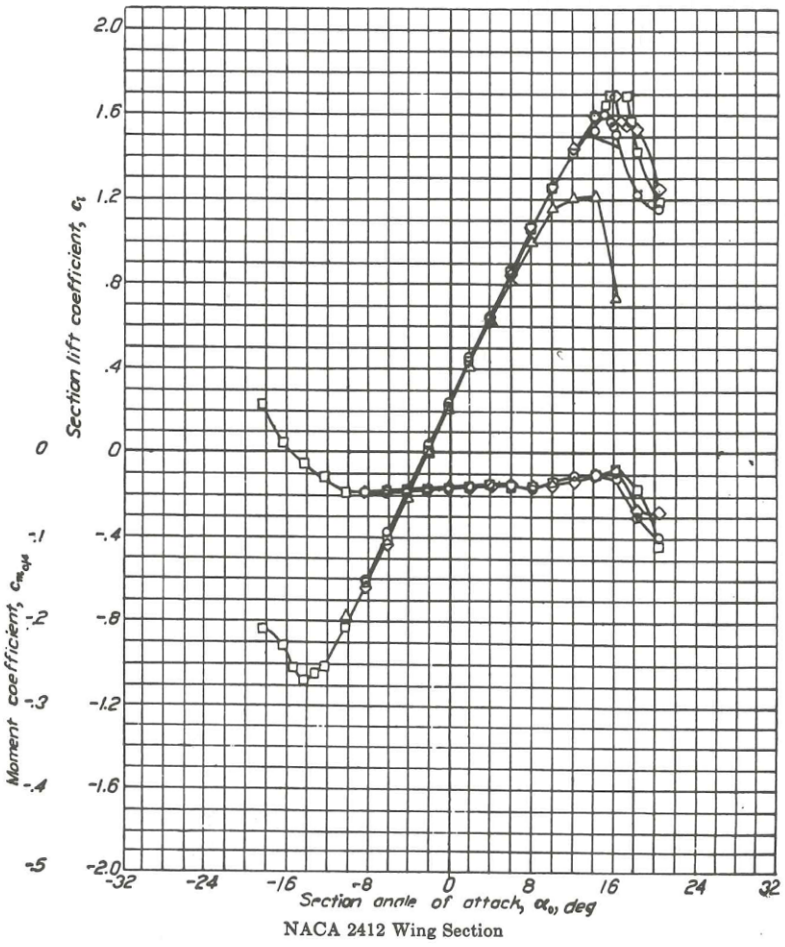

Figure 2.9: Section lift coefficient and moment coefficient for a NACA 2412 airfoil[And00]

2.2.4 The Blade Element Model

Reversing the non-dimensional approach above gives us the blade element model. The blade element model is the most widely used model in aerodynamics. It is a two-dimensional quasi-steady state model that abstracts difficult aerodynamic concepts into non-dimensional coefficients. Typically, a specific airfoil is tested in a wind tunnel to experimentally record its coefficient values at different angles of attack. Thus the blade element model allows lift and drag values to be obtained at any angle of attack. The resulting coefficients apply only to that airfoil, and any information about the shape of the wing is encoded in those coefficients. Solving for lift and drag in Equation 2.8, gives us the lift and drag forces predicted by the blade element model (Equation 2.10). Here, the prime designation indicates that the forces are two-dimensional section forces. To obtain the three-dimensional force, we multiply the section forces by the span l. The span multiplied by the chords gives the area ($A = c\,l$), therefore we replace the span term with the area.

$$L' = \frac{1}{2}\rho U^2 C_L(\alpha)\, c \tag{2.10}$$

$$D' = \frac{1}{2}\rho U^2 C_D(\alpha)\, c \tag{2.11}$$

In this equation, the two-dimensional section coefficients are given instead of coefficients pertaining to three-dimensional airfoils (c_l and c_d instead of C_L and C_D). Here, we substitute the lift per span L' and drag per span D' instead of the total lift and drag. Likewise, the chord c appears in the denominators instead of the planform area.

2.2.5 The Quasi-Steady State

Wings which do not change velocity or angle of attack are said to operate in a steady state. The conditions on the airfoil will be the same at every instant in

time. In contrast, flapping wings or the wings of an aircraft undergoing a turning maneuver have changing flow conditions and are subject to the effects of unsteady flow. While no flying object ever exists in a truly steady state environment, one of the major assumptions of aerodynamics is that in many cases, unsteady flight can be modeled by a series of steady state models. This is the *quasi-steady state* assumption. In this way, a system of changing flow conditions is modeled as isolated steady state systems at each time step.

2.3 Avian Morphology

To understand avian flight we must understand the anatomy of the bird. The wings are complex biomechanical systems which rely on feathers as their primary means of interacting with the air. We will briefly review the skeletal system of the wing and the structure of feathers. Avian anatomy is very well documented in books by Chamberlain[Cha43], Lucas and Stettenheim[LS72], and Proctor and Lynch[PL93].

2.3.1 Feather Structure

There are several different types of feathers that occur in avian anatomy as shown in Figure 2.10. We are specifically concerned with flight feathers, also known as *Remiges*, which are only found on the wings. These feathers are rigid and stiffer than other feathers, designed to be aerodynamic and transmit force instead of providing insulation.

Figure 2.11 shows the structure of a typical feather. The feather is built around the central shaft or quill, known as the *rachis*. Stemming from each side of the rachis are filaments known as *barbs*. On the portion of the feather proximal to

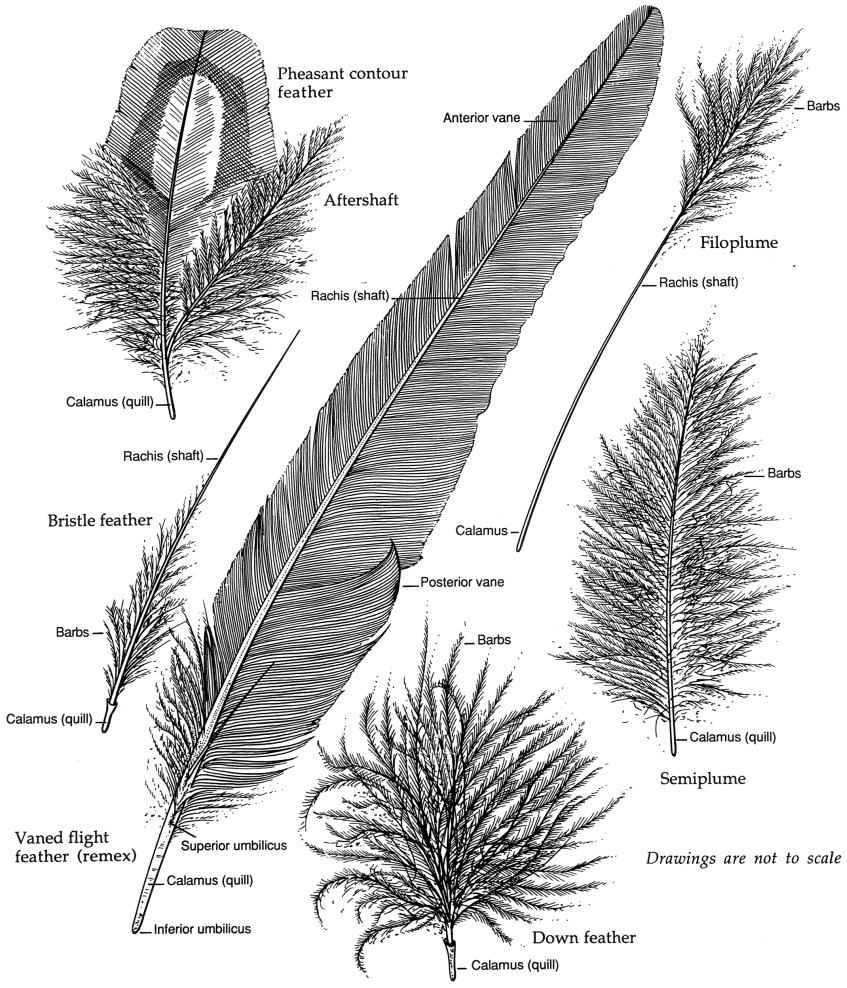

Figure 2.10: Different types of feathers[PL93]

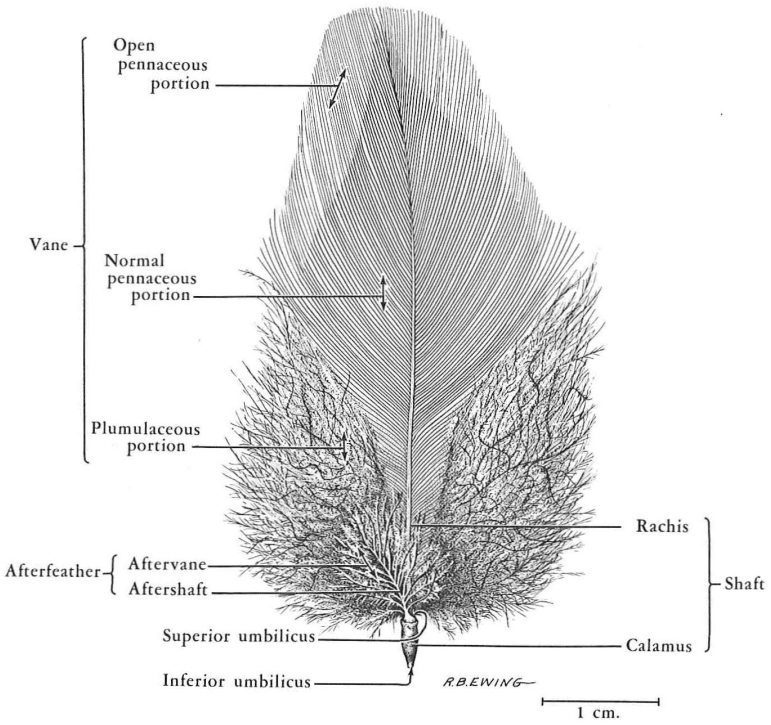

Figure 2.11: Avian feather structure[LS72]

the base, or calamus, the barbs are non-uniform and comprise the *plumulaceous* or downy section. Moving distally along the rachis, the plumulaceous barbs give way to organized and parallel *pennaceous* barbs. The remiges are comprised entirely of pennaceous barbs and contain no plumulaceous portion. The pennaceous barbs form two vanes, one on each side of the rachis. These vanes are asymmetric in profile and curvature for flight feathers.

Figure 2.12 shows a flight feather comprised of pennaceous barbs, and illustrates the three-fold fractal nature of feathers. Off of each barb, *barbules* extend, and each barbule contains microscopic *barbulets*. The barbulets allow the barbules of neighboring barbs to interlock and create a surface which will hold together and resist tension. Although the surface created is porous on the microscopic level, we will treat it as impermeable to macroscopic fluid pressure from air. This is a reasonable assumption given the no-slip condition of boundary layers which states

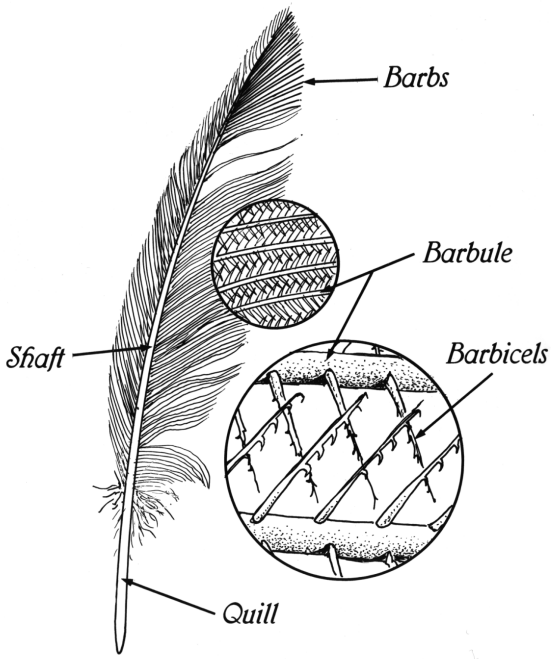

Figure 2.12: Microfeatures of a flight feather showing barbs, barbules, and barbulets[Goo92]

that the air molecules in contact with the barbules must move with them. This will create a boundary layer that, while very thin, will remain attached to the barbules.

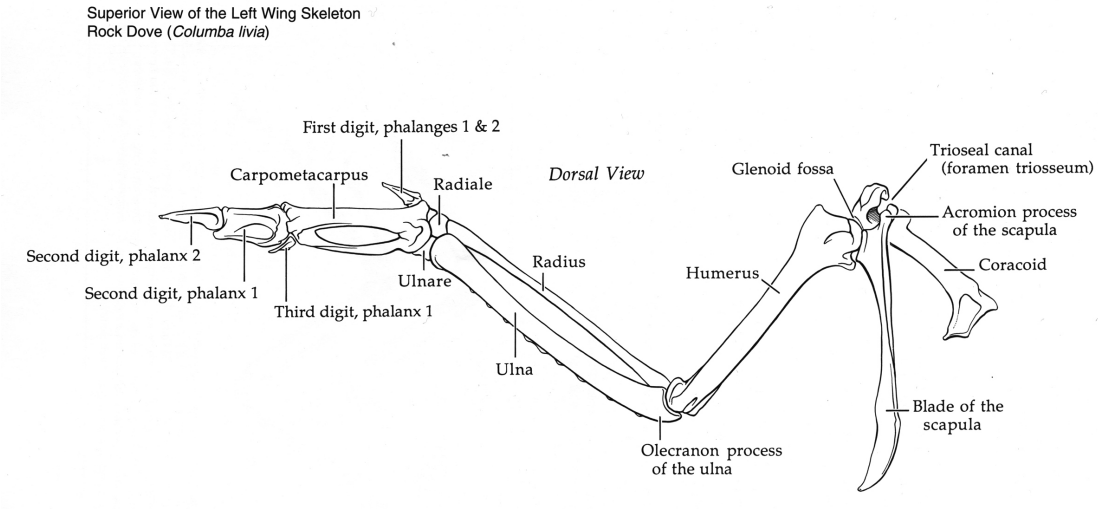

Figure 2.13: Sample skeletal system of a Rock Dove wing[PL93]

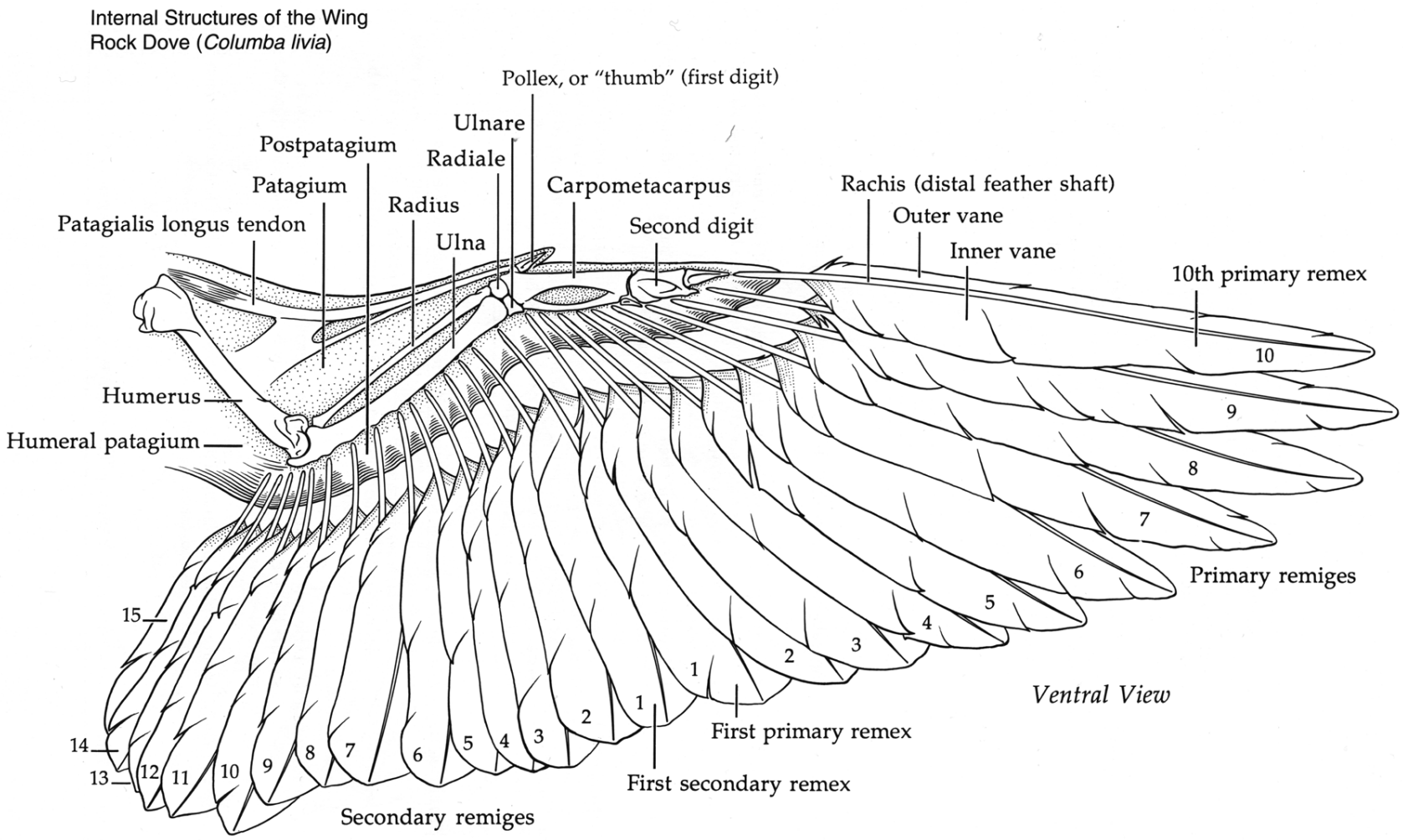

Figure 2.14: Anatomy of a Rock Dove wing showing bones and flight feathers.[PL93]

2.3.2 Wing Anatomy

Figure 2.13 shows the skeletal wing of a Rock Dove. The arm bones of a bird are similar to those of humans. The upper arm is comprised of the *humerus* bone, the forearm is comprised of the *radius* and *ulna*, and the hand is made up of several digits called the *carpometacarpus* and the *phalanx*. The radius and ulna allow for a degree of twist along the forearm. The wrist and hand, comprised of several bones, are collectively referred to as the hand-wing because there is little joint movement among the phalanx digits beyond the wrist.

Figure 2.14 shows the full wing with feathers as well as the skeleton. The wing consists of two types of flight feathers, primary feathers and secondary feathers. The primary feathers extend from the hand-wing are more active in the production of aerodynamic forces. The secondary feathers extend from the forearm and are closer to the body of the bird. They are less likely to separate and form more of a continuous surface. The follicle of each feather is anchored nearly to the bone with a set of ligaments.

Primary feathers are stiffer and asymmetric. The secondary flight feathers (secondaries) undergo less deformation, overlap more, and are more symmetric. Note that the feathers are numbered starting where the primary and secondary feathers meet. The index of the primary feathers increases distally toward the hand, and secondaries increase in number proximally toward the arm. Different species have different numbers of primary and secondary feathers.

CHAPTER 3

PREVIOUS WORKS

In this chapter we will review relevant flight studies from several different disciplines. We will begin by reviewing the primarily observational biological studies of hovering insect flight and forward bird flight. Insect flight shares many aerodynamic similarities with bird flight, and provides an ideal introduction to bird flight because it deals with more of the unsteady aerodynamic effects of wings. Next, we will explore the biological studies of bird flight; including capturing kinematic motion, force estimates, and pressure measurements. We will then shift our focus to engineering studies which sought to measure properties of bird wings using traditional direct force measurement approaches. Finally, we will detail two studies in the computer graphics field which sought to simulate bird flight using physically-based aerodynamics.

3.1 Insect Flight

The aerodynamics of insect flight have been studied far more thoroughly than bird flight, and although the aerodynamic mechanisms differ somewhat, insect flight is an excellent starting point for investigating the aerodynamics of flapping wing flight. Insect flight studies are interesting because their low Reynold's number flight regime combined with a reliance on wing rotation demands a scrutinization of unsteady aerodynamic effects. In contrast to birds and bats which fly at Reynold's numbers on the order of $10^4 - 10^5$, insects fly with Reynold's numbers on the order of $10^1 - 10^3$. The relatively smoother and more laminar nature of the flow around insect wings means that interesting flow artifacts such as vortices and separation can be taken advantage of. At higher Reynold's numbers, these flow artifacts are likely to degrade into turbulence from which energy cannot be recovered. Hovering

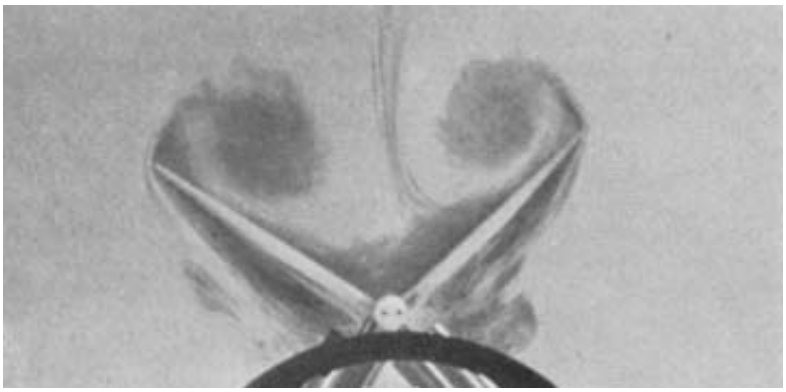

Figure 3.1: Dye in the fluid reveals the leading edge vortices around two model wings undergoing the fling phase of a clap and fling wingbeat[Max79]

flight is investigated most often as a pure form of flight and is the most rigorous test case. If an aerodynamic model can predict forces accurately for hovering, it should also be able to predict forward flight forces.

Weis-Fogh investigated hovering flight in 1972 by examining the net power required for hovering in the fruitfly *Drosophila*, as well as hummingbirds[WF72]. He assumed a sinusoidal wing movement, and calculated an average coefficient of lift over the entire wing stroke through a calculation which required knowing the weight of the specimen. A year later, after careful observation, he proposed a novel method by which insects generate lift which he called the *clap and fling*[WF73, Lig73]. The clap and fling describes a motion whereby insects clap their wings together on the apex of the upstroke, and then fling the leading edges of the wings open before the trailing edges separate to start the downstroke. This forms a pair of leading edge vortices which stay attached to each wing, increasing circulation and providing far more lift than can be accounted for by the quasi-steady state model.

In a detailed review of insect flight, Ellington's 1984 series of articles investigated the morphology, kinematics, aerodynamics, and power requirements for a number of species of insects[Ell84a, Ell84c, Ell84b, Ell84d, Ell84e, Ell84f]. Elling-

ton determined that the quasi-steady model is insufficient for predicting lift, proposed a new model for lift production by vortices, and compared the results of this model to the known power required for flight. However, Ellington conceded that insufficient knowledge of circulation profiles necessitates a calculation of mean lift coefficient using the weight of the insect.

Continuing the study of fruitfly hovering, Sane and Dickinson's 2001 experiment on an an actuated model of a *drosophila* wing takes the next step by attempting to record instantaneous lift and drag coefficients from a physical wing[SD01]. Sane and Dickinson's results for each test are accurate and thorough, but they found force coefficients to vary greatly due to minute changes in the kinematics of the wingbeat.

Sane and Dickinson found that although the lift and drag forces measured proved great enough to support the weight of the insect, the instantaneous forces differed greatly from those predicted by the quasi-steady state model. Figure 3.2b shows the instantaneous lift and drag profiles for one test wingbeat. The deviation between the measured forces (solid lines) and predicted forces (dashed lines) indicates the importance of wing rotation dynamics. In a subsequent article, Sane and Dickinson examined the prediction of these unsteady forces by looking at wing rotation in greater detail. In this study, the same model wing was rotated about different axes while translating, in an attempt to develop coefficients of rotation to improve the quasi-steady model[SD02]. It is clear from Sane and Dickinson's work that transient forces vary greatly with small changes in wingbeat kinematics, and predicting them is a difficult task.

Andersen et al. improved upon previous unsteady force models by rigorously examining the behavior of a falling flat plate[APW05]. They used high-speed video to quantify the trajectory of a plate falling with a Reynold's number on the order

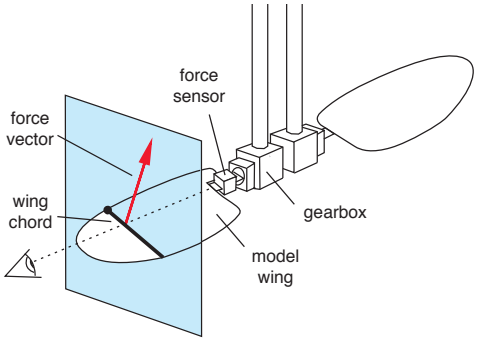

(a) Actuated model fruitfly wing showing wing planform and servo motors immersed in fluid[MHD99]

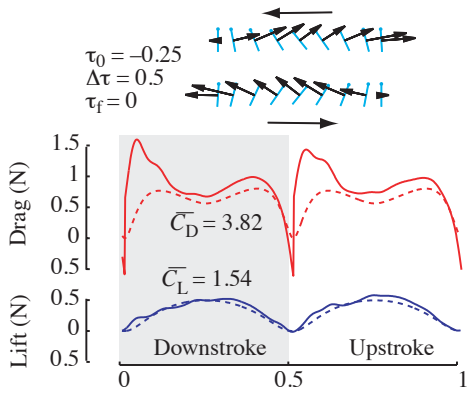

(b) Instantaneous lift and drag forces measured by the robotic fruitfly wing from one of many trials. The solid line indicates the forces measured from the experiment, while the dashed line indicates the forces predicted by a blade element analysis[SD01]

Figure 3.2: Schematic and sample results of Sane and Dickinson's robotic *drosophila* wing

of 10^3. Using their measurements as well as direct numerical solutions, they revised the flat plate aerodynamic force model to include the effects of acceleration and rotation, in addition to the traditional input of translation.

This model was validated by Berman and Wang in their 2007 study examining hovering of a fruitfly, bumblebee, and hawkmoth[BW07]. Using an optimization algorithm to create kinematics which maximize lift and minimize energy expenditure, Berman and Wang found that the quasi-steady forces predicted by Andersen et al.'s model matched the weight of the insects well. For the fruitfly, the model predicted three tenths of a percent more force than the weight of the insect. For the bumblebee, it predicted five percent less force, and for the hawkmoth it over-predicted by fifteen percent.

3.2 Avian Flight

When comparing insect flight to bird flight, many similarities can be extended from one flight regime to the other. Crucial to the investigation into any type of flapping flight is the importance of quantifying the kinematics of the wing; that is, specifying as precisely and accurately as possible the motion of the wing and its joints in all degrees of freedom.

3.2.1 Kinematics

While scientists can qualitatively observe bird flight and draw useful conclusions, it is necessary to precisely measure the motion of a bird's flapping motion in order to fully understand avian flight and perform numerical simulations. To date, only a few techniques have proven adequate for capturing useful data describing a bird's motion and the airflow around it. Dial et al. employed high speed x-ray

videography, also known as cineradiography, to capture the motion of a starling flying in a wind tunnel[DJJ91]. The bird had had steel pins surgically implanted in the wing prior to flight to aid the researchers in determining joint angles when analyzing the x-ray film. Although only one camera was used and thus coordinates of the pins had to be estimated in the third dimension, this study was one of the first to attempt to quantitatively plot wing joint angles with respect to time for a wingbeat. While lacking some numerical precision, Figure 3.3b shows the orientations of the three bones of the wing.

3.2.2 Wake Visualization

Cineradiography is a valuable tool for measuring joint positions and muscle activity, but it is sometimes necessary to observe the effects of a wing on the surrounding air. Nearly the only technique for doing so is known as digital particle image velocimetry (DPIV). DPIV allows for the visualization of fluid flow by using a strobe light or laser to illuminate helium-filled neutrally-buoyant soap bubbles suspended in the flow. The tiny bubbles act as point sources of light as they reflect the illumination from the source light. They can then be imaged by a stereoscopic pair of cameras. The small spatial parallax between the cameras produce correlated projections of the scene in each images where the slight differences in position of the bubbles allows their three dimensional coordinates to be computed. Because the bubbles travel some finite distance during the time the camera shutter is open, a short trail is left on the film from which velocity can be computed, giving a complete picture of the velocity field[SRP84].

Figure 3.4 shows the DPIV pair of stereo images of a kestrel in flight. The vortex structure of the wake can be seen as the cyclone-like feature in the bottom of the frames. DPIV is a powerful tool for imaging fluid in the wake of a bird,

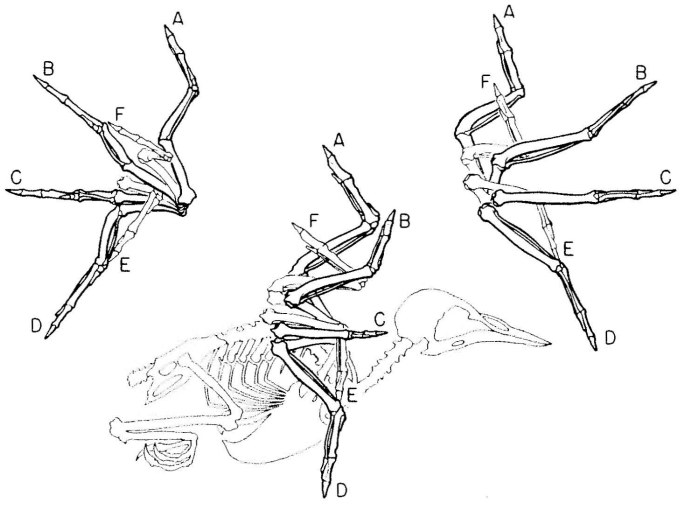

(a) Side view sketches of a Starling's skeletal wing poses from Dial et al.'s radiographic study[DJJ91]

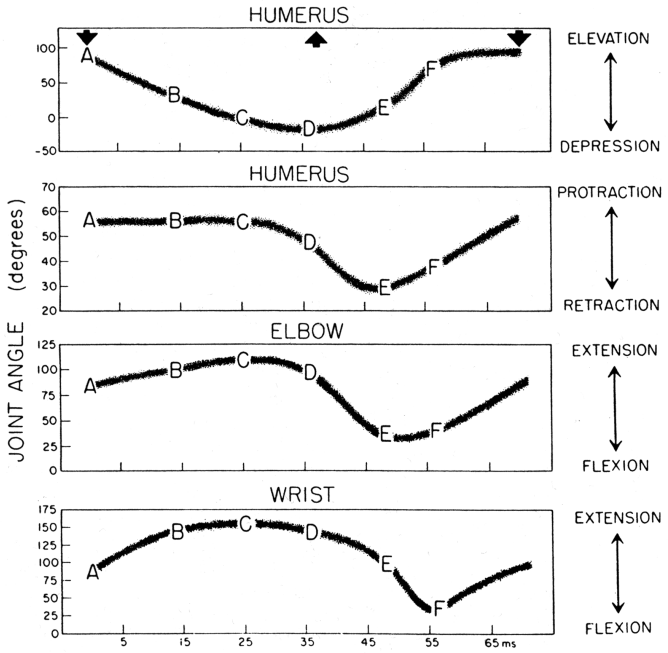

(b) Joint angles of a Starling's wing bones throughout a wingbeat

Figure 3.3: Results from Dial et al.'s study of Starling flight[DJJ91]

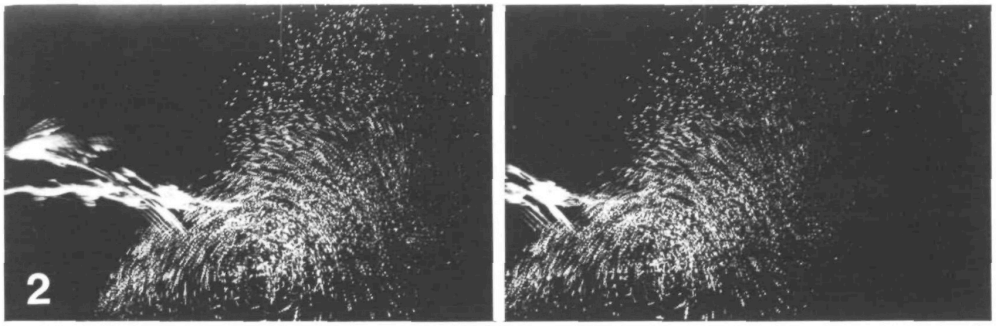

Figure 3.4: Wake of a Kestrel visualized through particle stereophotogrammetry[Spe87]

but how to use such data is less clear. Rayner's vortex theory of animal flight, innovative for its time, introduced a means for calculating the momentum of the fluid and thus the power expenditure of the bird[Ray79a, Ray79b]. Rayner proposed that the wake produced by a flapping bird in flight consists of a chain of elliptical vortex rings, one per wingbeat. With each wingbeat, the bird transfers momentum to the fluid creating a vortex, and resulting in an opposite and upward momentum acting on the bird thus keeping it aloft. By using DPIV to deliver the velocity field of a wingbeat vortex, one can use Rayner's vortex theory to compute the momentum that such a vortex of given size would have imparted to the bird. Spedding attempted to calculate this momentum that when analyzing the wake of a jackdaw. However, due to the extremely complex nature of fluid flow, he determined that the vortex wake contained only thirty-five percent of the momentum necessary to keep the bird aloft.[Spe86].

3.2.3 Gait Selection

A number of studies have concerned themselves with investigating the gaits with which birds choose to fly[HTB02, THB03, TD96, Tob07]. This is loosely analogous to investigating the difference between walking and running in humans. The first

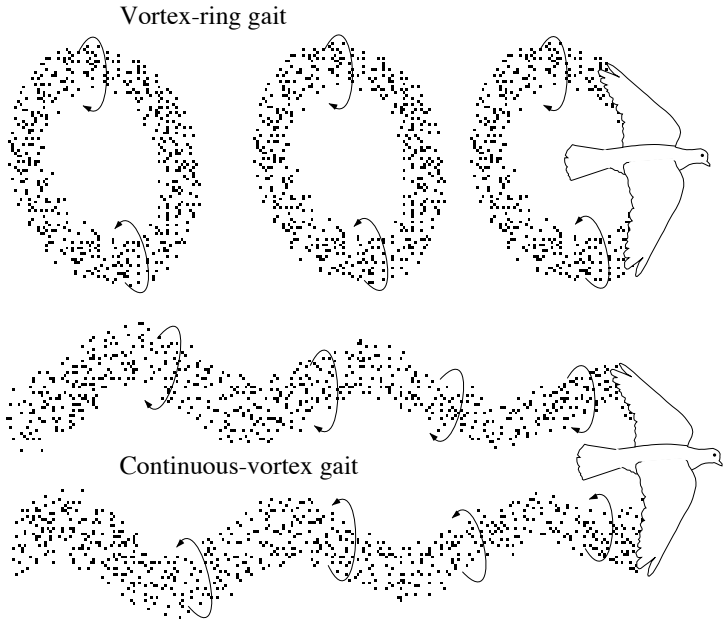

Figure 3.5: Avian flight gaits[TD96]

gait, the vortex-ring gait, creates discreet vortices, and is often employed by smaller birds flying at slower speeds. The second gait, the continuous-vortex gait, is more likely to be observed in larger birds for birds flying at faster speeds. A bird flying with a continuous vortex gait will not retract its wings fully on the upstroke and has more in common with the soaring flight associated with gulls and birds of prey. Figure 3.5 illustrates the difference in the wake of the two gaits. This difference was first noticed by Spedding while using DPIV to image the wake of a Kestrel [Spe87].

Thus far, we have seen seen how cineradiometry and particle image velocimetry can be used to gather data about bird flight. However, neither of these techniques can resolve simultaneous joint positions. Figure 3.6 shows Tobalske and Dial's estimates of wrist and wingtip locations of a magpie flying at four meters per second. However, in this study only those two points were plotted, and the markers used to indicate wrist and wingtip locations on the bird had a width of one centimeter.

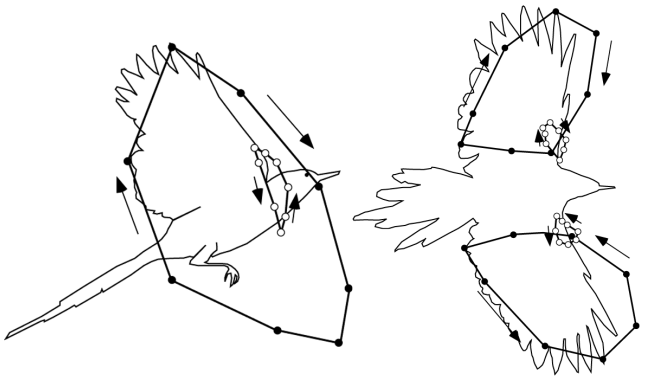

Figure 3.6: Wingtip and wrist motion of a Magpie in steady flight at 4 m/s[TD96]

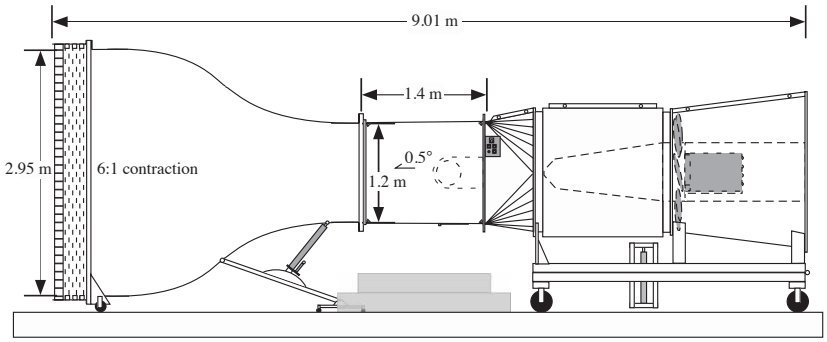

Figure 3.7: The Harvard Field Station's avian wind tunnel used by Hedrick et al.[HTB02]

Furthermore, data was recorded on low resolution cameras at the slow framerate of 60 frames per second[TD96].

3.2.4 Motion Capture

Hedrick et al. continued their studies on bird flight and kinematics in their 2002 study [HTB02]. They utilized the Harvard-Concord Field Station's wind tunnel (Figure 3.7) to capture the flapping motion of Cockatiels and Turtle-Doves. By mounting four high-speed cameras around the transparent test section of the wind tunnel and lighting the test section with six 300 watt halogen lamps, Hedrick was able to attain excellent high contrast high speed (250 frames per second) video of

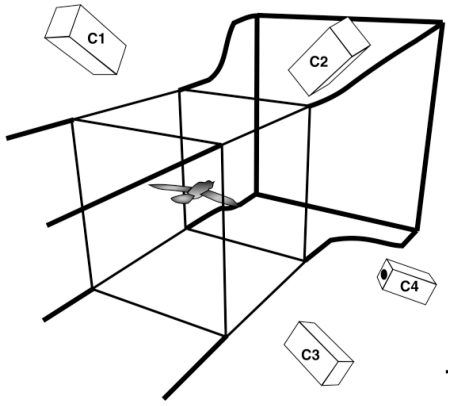

Figure 3.8: Position of motion capture cameras relative to wind tunnel test section[HTB02]

birds trained to fly in the wind tunnel.

To gather kinematic data, birds were outfitted with reflective markers on their wings prior to flight. Each marker was five millimeters in diameter, and five were placed on the right wing of each bird. Figure 3.9 shows sample data of a bird with markers on its wing from each of the four cameras. By utilizing the direct linear transformation technique (DLT), three dimensional coordinates for each marker were computed from the camera views.

Knowing the motion of five important points on the wing, Hedrick represented the wing as two triangles defined by the measured five markers in order to perform aerodynamic calculations. This simplified representation allows one triangle to represent the primary feathers, and the second to represent the secondary feathers (T2 and T1 respectively in Figure 3.10).

Hedrick uses these two polygonal faces to calculate the amount of lift produced by the bird. He assumed a sinusoidal curve for the coefficient of lift. He then computed the total velocity around each wing panel. The velocity that each triangle experiences is a sum of the forward velocity of the bird (or speed of the wind tunnel), the velocity of the wing relative to the body of the bird, and also a factor called the induced velocity. The induced velocity accounts for changes in velocity

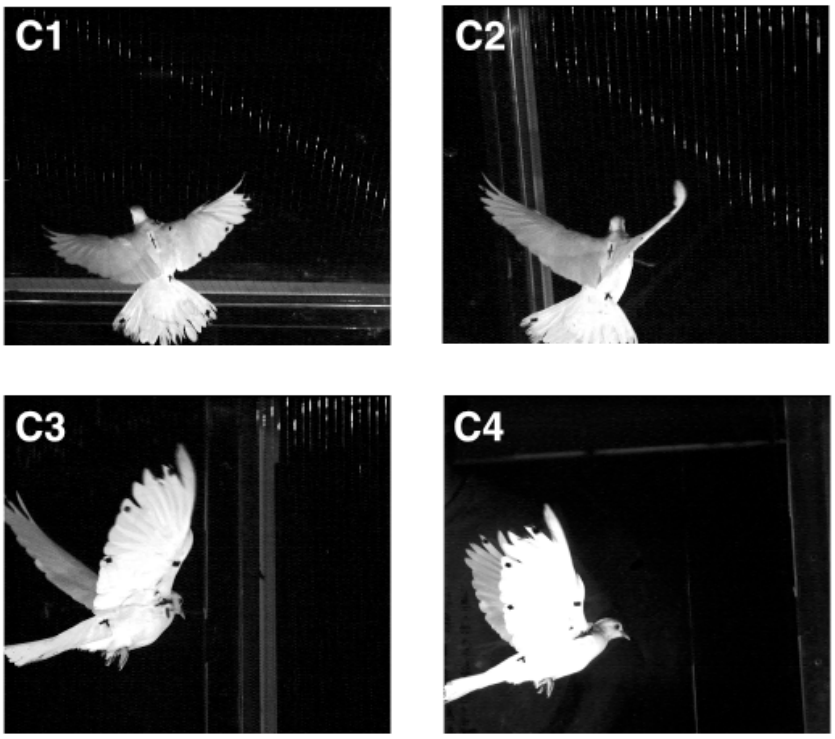

Figure 3.9: Motion capture camera views showing markers on a Turtle-Dove in the wind tunnel[HTB02]

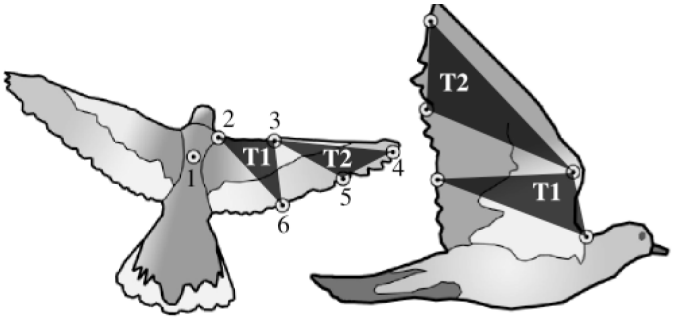

Figure 3.10: Triangular representations of the primary and secondary feathers approximating the wing of a Turtle-Dove[HTB02]

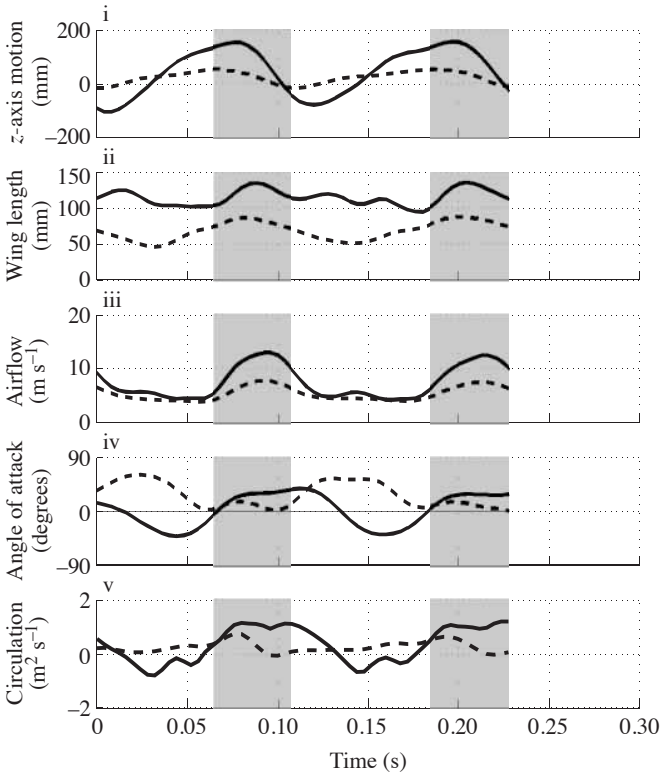

Figure 3.11: Hedrick et al.'s kinematic and force data for triangular wing sections of a Turtle-Dove in the wind tunnel[HTB02]

due to the tendency of a disturbed wake to affect the velocity of oncoming air. Once the total velocity is known, circulation and finally the total lift force can be calculated. Figure 3.11 shows his collected data for vertical position, length, and relative velocity, as well as the calculated angle of attack and circulation for both of the two triangles representing the wing over two wingbeats. The solid line indicates data from the distal triangle representing the primary feathers, while the dashed line represents the proximal secondary feathers. The shaded time periods indicate the downstroke.

Hedrick concluded that this aerodynamic model underestimates the lift on birds flying at slow speeds (below 5 m/s) and overestimates the lift at high speeds (above 11 m/s). While this model is crude, it seems applicable to the middle range of flight speeds for the birds that Hedrick was investigating. Clearly however, the

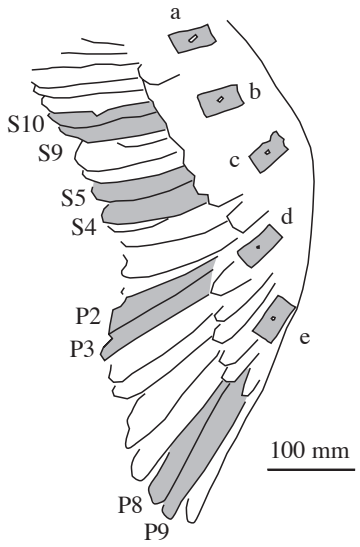

Figure 3.12: Pressure transducers (labeled *a* through *e*) mounted to pairs of primary and secondary feathers on the wing of a Canada Goose [UHB03]

geometric representation of a flapping wing can advance beyond the simplicity of two triangular elements.

3.2.5 Pressure Measurements

In order to gain insight into the aerodynamic forces acting on a flapping bird's wing, Usherwood et al. applied a novel approach in their 2003 study directly measuring the air pressures on the wing of a flying Canada Goose[UHB03]. By attaching pressure transducers to feathers shafts along the wing, the differential pressures between the top and bottom surfaces of the wing were measured in five locations (Figure 3.12).

Figure 3.13 graphically illustrates the magnitudes of the pressure at each transducer site along the wing over a single wingbeat. As expected, we can see that the pressures increase toward the distal end of the wing, where the feathers are moving faster. Also of note is the unforeseen double peak in pressure at the most distal site, and the positive pressure at the proximal sites which is maintained

throughout the stroke.

This study provides interesting new insight into the mechanics of bird flight; however it is highly constrained and looks only at one species of bird at one flight speed. Further, five transducers across the span of the wing seems to prove adequate for resolving the pressure distribution spanwise, but gives only one data point in the chord-wise direction oriented along the shafts of the secondary feathers.

Usherwood et al. followed this study two years later by conducting the same experiment, with more sensors, this time on pigeons in slow flight[UHMB05]. Here, they measured the pressure differential with eight transducers on the wing instead of five, and also turned their attention to the tail where they added four transducers. They found similar results in the pigeon as they found in the goose, and went on to investigate the muscle-mass specific power required for the bird to overcome gravity.

The additional sensors address some of the above shortcomings and provide a greater wealth of knowledge; however it is still unclear how to extract forces on the bird's flight surfaces from these pressure measurements. In the absence of kinematic joint motion data, it is impossible to describe the force vector even though the pressure data can help determine the magnitude. One of the most important aspects of these studies is that they were carried out in still air, away from the complications of wind tunnel flight. Without the turbulence of fan blades and visual distractions, these birds are likely to have flown more naturally. It has been shown that the induced velocity of the wind tunnel environment causes birds and bats to fly unnaturally [Ray94].

The last study of interest sought to quantify the instantaneous aerodynamic accelerations on a flying bird. To this end, Hedrick et al. flew cockatiels in a wind tunnel at various speeds, and recording both kinematic motion data through

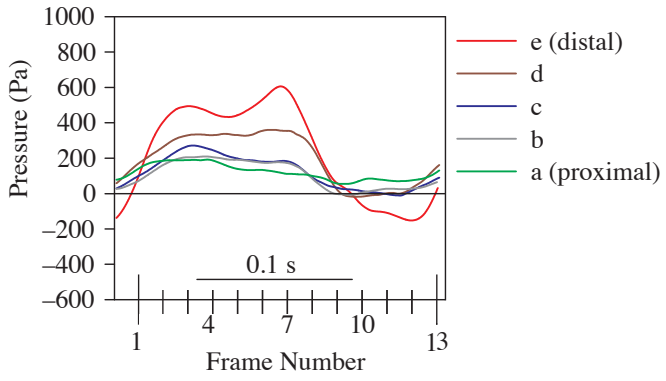

(a) Magnitude of each transducer plotted versus time

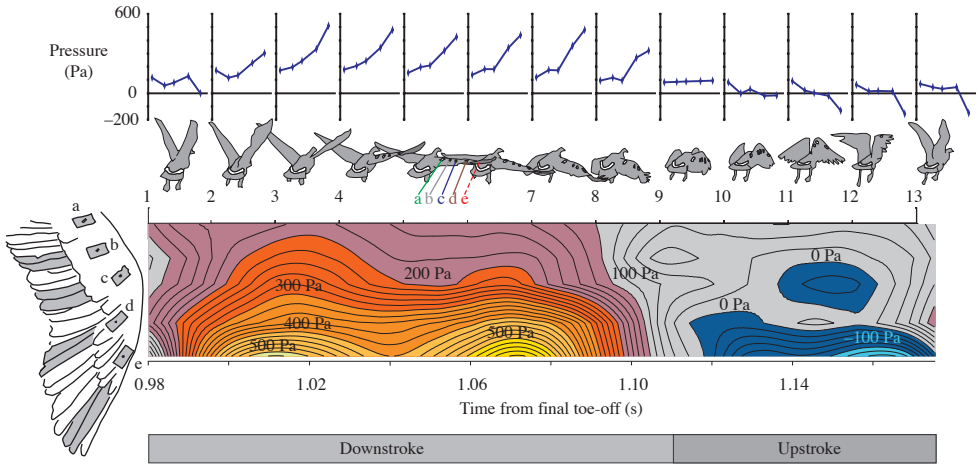

(b) Spatial representation of pressures along the wing. On top, the graphs indicate the pressure distribution from shoulder to handwing for each frame. In the middle, an illustration of the goose and wingbeat phase for each frame. On the bottom, a map using colors to show the magnitudes of pressures across the wing. Yellow indicates areas of high pressure, while blue indicates negative pressures, and grey represents pressures near zero.

Figure 3.13: Pressures on individual transducers across the wing throughout one wingbeat of a Canada Goose[UHB03]

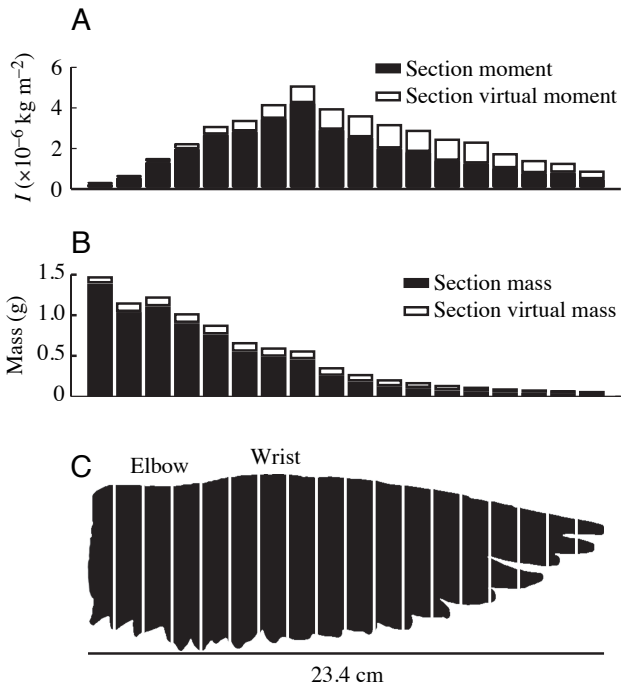

Figure 3.14: Mass and moment of inertia distributions of a Cockatiel wing[HUB04]

high speed cameras, as well as instantaneous acceleration data through a three-axis accelerometer mounted to the bird's torso[HUB04]. To determine the inertia of a flapping wing, they sliced a feathered specimen wing into 1 centimeter wide strips, weighed and determined the center of mass of each strip. Treating each slice as a point mass, he now had a mass distribution and moment of inertia for the wing. Knowing the wing kinematics, Hedrick et al. were able to subtract the inertial accelerations due to wing movement on the body of the bird to obtain the instantaneous accelerations due only to aerodynamic forces on the bird. They used this data to draw conclusions about the energy expenditure of the bird and the percent of lift generated on the upstroke. They did not compare their data to a force prediction model.

3.3 Aerodynamic Properties of Bird Wings

Apart from studying live birds flapping, researchers have examined the properties of rigid specimen wings. These few studies attempt to treat a bird wing as a classical airfoil and measure lift and drag coefficients. These studies ignore the flapping motion entirely and observe the wing under steady state conditions, but have the benefit of measuring forces directly. Working with dead specimens allows the attachment of force transducers to precisely measure the aerodynamic forces on the wing.

In 1981, Withers tested wings of several bird species in a wind tunnel at many different angles of attack and flight speeds. He used specimen wings dried in an open position, and reinforced the humerus with a brass rod for strength. He reported no significant bending of the feathers or separation of the primaries to confound his data. His results showed a wide range of lift and drag coefficient curves among the different species, and a large variance within the data for each wing. The coefficient curves for most wings could be correlated to a quadratic best-fit curve. Figure 3.15 shows Withers' coefficient of lift, coefficient of drag, and the lift-drag ratio curves for one of his examined species; the European Starling. For this wing, he only recorded data at angles of attack between negative fourteen and positive fourteen degrees, which limits the usefulness of the data. Furthermore, he provides no insight into how his steady-state analysis translates to unsteady flapping wing flight.

Recognizing that air flows faster over the tips than the bases of flapping wings, Usherwood and Ellington sought to examine a variety of animal wings in the manner of classical propellers by rotating them[UE02]. They examined the aerodynamic properties of several insect wings as well as a quail wing. The insect wings were not real wings, but plastic wings cut and molded to the proper shape. An

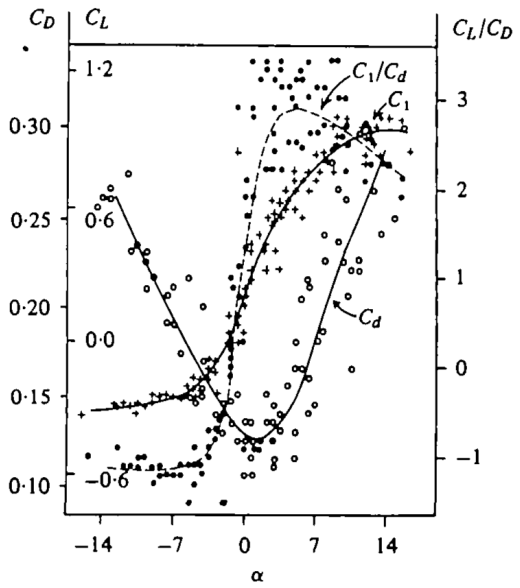

Figure 3.15: Experimental wind tunnel C_l, C_d, and C_l/C_d curves for the wing of a European Starling specimen (*Sturnus vulgaris*)[Wit81]

actual quail (*Coturnix chinensis*) wing was used for the quail study, and a plastic quail wing was also tested for comparison. The wings were mounted on an intricate rig which allowed them to be rotated at precise angular velocities. The rig included an integrated force transducer to directly measure the forces generated by the air on the wings. Figure 3.16 shows the measured lift and drag coefficients derived from the measured forces for three insect species as well as the quail. Usherwood and Ellington examined a much wider range of angles of attack than previous studies, as shown in the figure, and the resulting curves approximately represent periodic functions as indicated by flat plate theory. Later, Usherwood repeated the study on Pigeon wings while also measuring pressures on the wing, and found similar resulting lift and drag coefficient curves [Ush09]. While these studies still represents a steady-state approach, they recognize that the velocity profile on a wing is non-uniform and thus obtain more realistic coefficient curves.

In 2005 March et al. took the study of specimen wings one step further by directly measuring the forces on a real wing whose shape could be changed [MBG05].

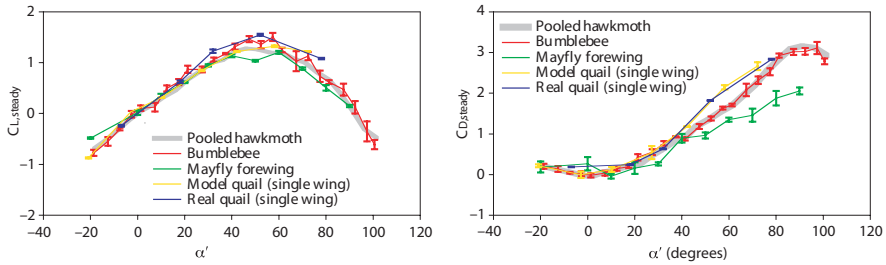

Figure 3.16: Lift and drag coefficients vs angle of attack for several species recorded in rotating wing experiments[UE02]

Figure 3.17: Red-tailed hawk wing with poseable wrist on a force transducer in a wind tunnel[MBG05]

They surgically implanted steel wires in the arm of a deceased Red-Tailed Hawk (*Buteo jamaicensis*) so that the wrist could be held rigidly at different angles. They then tested the wing on a force transducer in a wind tunnel at different airspeeds, angles of attack, and wrist angle. They also performed tests on a Great Horned Owl wing (*Bubo virginianus*) but did not actuate the owl's wrist joint. While this study implemented new methods for studying the aerodynamic effects of changing wing shape, too little data was recorded over too small a range of angles of attack (negative five degrees to positive twenty degrees) to draw any useful conclusions.

3.4 Animation Studies

To date, studies of avian flight have primarily fallen into one of two domains, biology and ornithology, or aerospace engineering. Biological studies of bird flight are interested in metabolic energy and power requirements, and therefore the simplest aerodynamic force models are sufficient. Even a first order estimate of a bird's power requirement is sufficient to gain important insight into migration patterns and the distances birds can fly between food sources. Thus biological studies have only a tangential application of aerodynamics. These studies are experimental in nature, based on observation and measurement, with little need for computer simulation.

In contrast, aerodynamic studies in the engineering domain have developed powerful fluid simulation techniques and force models. Numerical methods can solve complex flow conditions with great accuracy. However, these techniques are primarily applied to traditional fixed-wing type aircraft studies. With no historical motivation to create flapping aircraft (ornithopters), the aerospace community has focused its attention on rigid-body aircraft.

The techniques of both of these domains can be used directly in computer animation and simulation. The computer animation and motion picture industry has developed sophisticated physically-based simulation techniques, as well as designing a set of tools to create and animate virtual creatures. Birds have appeared in many computer generated feature films, including recently: Disney-Pixar's *Up*, Pixar's *Finding Nemo*, Dreamworks Animation's *Kung Fu Panda*, and Weta Digital's *Lord of the Rings*. However, the motivation behind the avian-inspired creatures in these films is entertainment, not realism. A minimal amount of research has been dedicated to the accurate portrayal of birds in the animation and computer graphics field. However, the few attempts to simulate a virtual bird using

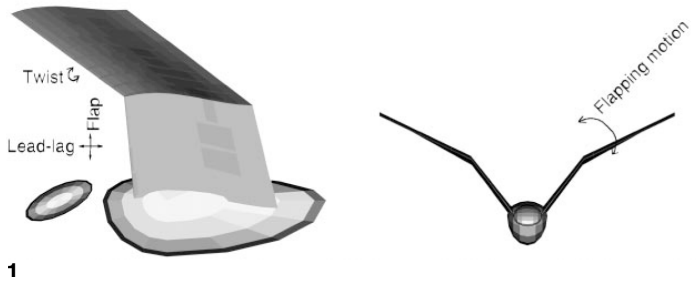

Figure 3.18: Ramakrishnananda and Wong's geometric bird model showing a wing as two airfoils[RW99].

physically based aerodynamics are notable.

The first study to take this approach of using physical principles to simulate and animate the forward flight of birds was that of Ramakrishnananda and Wong[RW99]. They used a very primitive representation of bird geometry where a wing is comprised of two airfoil sections each with one hinge, a degree of twist, and a sweep angle (Figure 3.18). This model ignores the wrist joint, constrains the degrees of freedom of the other two joints, and ignores any effects of feathers. Given user inputs such as the wingbeat frequency, a set of dynamic equations describe the state of the system for each timestep. A proportional-derivative controller attempts to propel the bird along a series of user specified waypoints. Each timestep is solved sequentially to find the optimal angle of attack, twist, and sweep for each section. A blade element model was used, but the coefficients were not described in the article. Without specifying the lift and drag coefficients, the physical accuracy of even such a simplified model can be called into question.

Building on the work of Ramakrishnananda and Wong, Wu and Popovic's 2003 model was a vast improvement[WP03]. This new model was far more advanced in the way it represented a bird's geometry. As shown in in Figure 3.20a, the wing was morphologically accurate, taking the shoulder, elbow, and wrist joints into account. The shoulder was represented as a ball joint with twist, for a total for four degrees

Figure 3.19: Ramakrishnananda and Wong's animated eagle[RW99].

of freedom. The elbow and wrist joints were both modeled as single degree of freedom hinge joints, though the elbow had an extra degree of twist mimicking the action of the radius and ulna bones. While the wrist is technically a ball joint with two axes of rotation, it was represented here with only one. The primary function of the wrist is to control the spread of the primary feathers, which it can do as a single axis hinge joint. The lack of a second degree of freedom may limit the model, but the wrist still serves its function. The tail was also accounted for in this model, as a non-trivial amount of lift and moment on the body is generated by the tail.

Feathers were represented in a way that simplifies their geometry while still accounting for the mechanisms by which they physically interact with the air. Each feather was represented as a quadrilateral, as shown in Figure 3.20b, and made dynamic by the introduction of three virtual springs. A twist spring and a bend spring exist at the base of the feather, and a second bend spring was placed in the middle of the feather to allow for bend along the rachis. These added degrees of freedom allowed for important interaction with the flow as the feathers bend and twist to change the configuration of the wing. Aerodynamic forces were tallied for each side of a feather (shown as the dotted line in Figure 3.20b) so that they

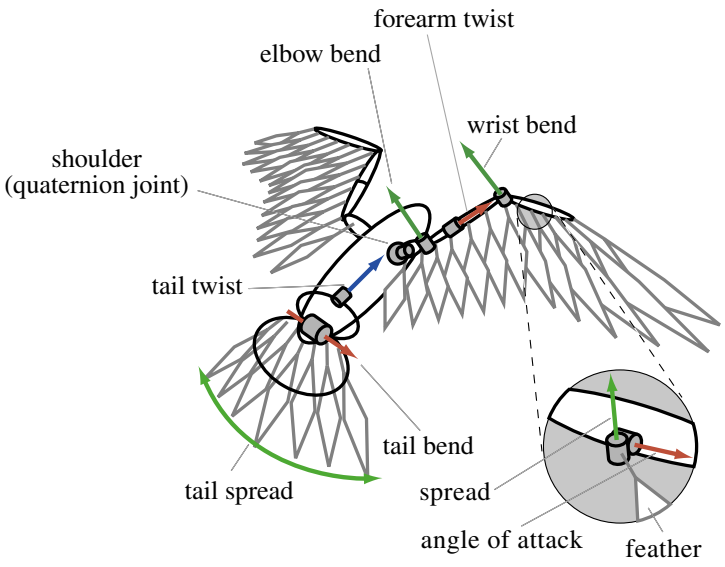

(a) Bird rig with joints and degrees of freedom indicated

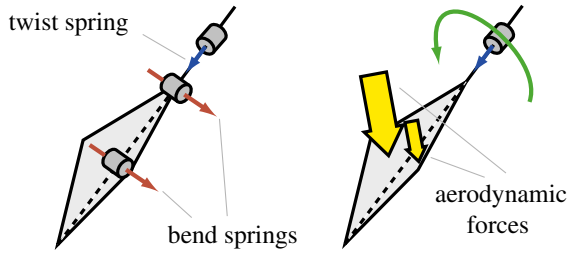

(b) Individual feather geometries showing springs and degrees of freedom

Figure 3.20: Wu and Popovic's geometric and kinematic representation of a bird[WP03]

could be summed to find the total forces.

The goal of this study was visual realism, not numerical accuracy and thus a quasi-steady blade element model was sufficient. Wu and Popovic cite Withers [Wit81] as a baseline for their lift and drag coefficients, but Withers' data falls within a very narrow range of angles of attack. For lift and drag coefficients outside this curve, Wu and Popovic conjectured values which were intuitive but not based on any physical properties. These curves are shown in in Figure 3.21. It is unclear how the functions representing these coefficients were derived. However,

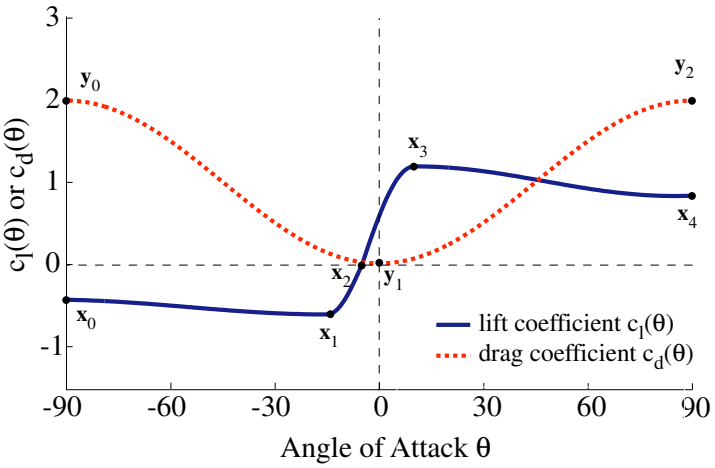

Figure 3.21: Wu and Popovic coefficient of lift and drag curves over the complete range of angles of attack[WP03]

their success in creating realistic animations lends at least some merit to these arbitrary coefficients.

Once the aerodynamic forces were computed, an advanced simulated annealing algorithm solved for wingbeat parameters. These parameters, such as amplitude and frequency for each joint, were specified and held constant through one wingbeat. The solver therefore found the kinematic parameters for each wingbeat in order for the bird to follow a user-specified path. The simulated annealing solver minimizes a specified energy function by finding a local minimum which is probabilistically representative of the global solution. This solver does not find an exact solution, as this is often impossible in simulations with many degrees of freedom; instead the solver ran for one thousand iterations per wingbeat in order to converge on a solution.

The energy function specified by Wu and Popovic is a concatenation of six terms. The first three terms are measures of the deviation from the specified path in position, velocity, and orientation. The fourth term seeks to minimize both the angular velocity of the bird's body and the first derivative of the angular velocity

Figure 3.22: Wu and Popovic's resulting animation of a raven taking off[WP03]

of the body to achieve smooth flight. The fifth term minimizes forearm twist on the upstroke, a metric that mimics this energy conserving feature of true bird flight and makes for realistic looking animations. The last energy minimization term penalizes backflow of feathers through the air; that is a feather moving with negative relative airspeed with respect to its forward pointing vane. If this were to happen, it would ruffle a bird's feathers and create parasitic drag. The simulation optimization step solves these parameters for the next wingbeat, and the two wingbeats are blended together into a smooth motion.

Wu and Popovic's results are impressive and show a high degree of visual realism. While their methods are more intuitive than experimental, the fact that their results are very similar to the way real birds fly is encouraging. However, the lift and drag coefficients used are arbitrary, and other parameters require manual adjustment in order achieve realism. Constants such as feather spring stiffnesses and energy function coefficients need all require user input. Furthermore, the quadrilateral representation of feathers leaves significant room for improvement in their geometric resolution. With more complex geometry, more realistic aerodynamic forces can be modeled.

CHAPTER 4

CONSTRUCTING A DIGITAL BIRD AND WINGBEAT

In this chapter, we detail the steps taken to digitally recreate the motion of a flapping bird. The particular bird whose geometry we recreate and whose motion we capture is a Red-winged Blackbird (*Agelaius phoeniceus*). We concentrated on this species because it lent itself well to observation for high-speed motion capture in our flight tunnel. However, in order to mimic the captured motion we must first have a digital model of the bird.

We start by building off of work done by Jeffrey Wang to construct a morphologically accurate deformable bird mesh and rig[Wan07]. Then, we introduce a novel method to obtain individual feather geometry by laser scanning. Knowing the geometry of the bird's body as well as its feathers gives a complete model of the bird. We then utilize the research conducted by Brendan Holt on high speed motion capture of a Red-winged Blackbird[Hol09]. This work yields highly detailed kinematics of the wingbeat of a bird in level flight in a flight tunnel. Applying the joint angles resulting from this study to our digital bird model, we have a morphologically accurate polygonal bird wing undergoing a physically measured kinematic wingbeat motion. Because the model is polygonal, in the next chapter we will analyze these polygons to compute the aerodynamic forces on each and obtain a total force on the bird.

4.1 The Skin Mesh of an Ivory-Billed Woodpecker

4.1.1 Computerized Tomography and Modeling of the Body

Motivated by alleged sightings of the thought-to-be extinct Ivory-billed woodpecker (*Campephilus principalis*)[FLL$^+$05], Jeffrey Wang's 2007 work used three-

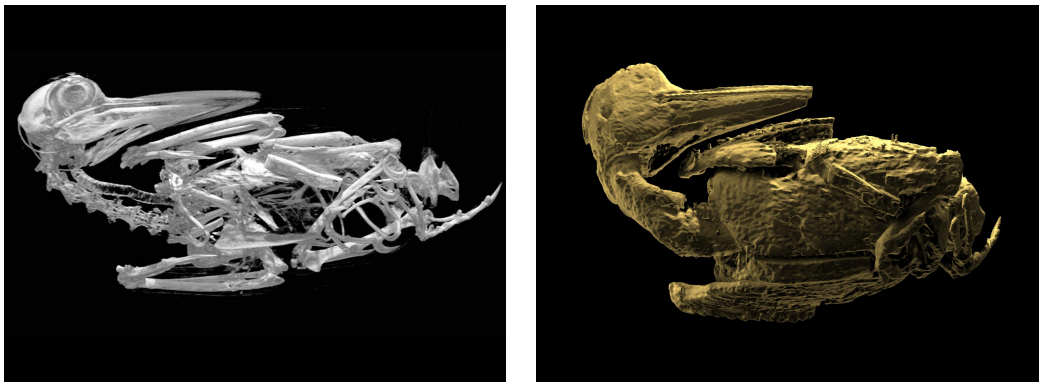

(a) CT data filtered to isolate bones and reveal the skeleton **(b)** CT data filtered to reveal the bird's skin

Figure 4.1: Wang's Ivory-billed woodpecker reconstructed from computerized tomography scan data showing different anatomic features[Wan07]

dimensional volume capture techniques to construct a digital model of this bird[Wan07]. Since the species was considered extinct, a pickled specimen was used for analysis. This specimen was scanned using x-ray Computerized tomography (CT), which produced a series of two-dimensional scans. These scans were stitched together to create a three-dimensional volume using medical imaging techniques [MSS92][SFF91]. Wang was then able to manually define contours of bone and skin, building a three dimensional skeleton and skin mesh.

Next, Wang employed animation techniques to create a rig of virtual joints for the model, joints which mimic the physiological degrees of freedom of the actual bird. This was based in part on the specimen's skeleton revealed by the CT scan (Figure 4.1a). Wang then fit a mesh of quadrilateral elements to the skin surface indicated by the CT scan. In this way he was able to smooth the rough surface shown in Figure 4.1b, and obtained a clean mesh suitable for binding to the joint rig. By using the animation technique of smooth skinning, the mesh thus became deformable, and Wang was able to pose the the virtual model of the bird in any position.

Figure 4.2 shows the smooth digitally reconstructed skin mesh of the Ivory-

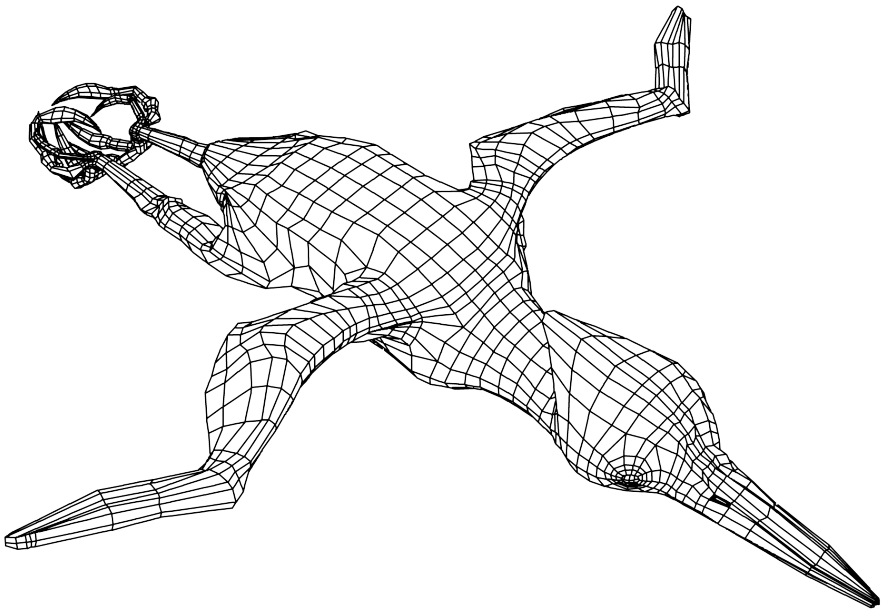

Figure 4.2: Wang's digital Ivory-billed woodpecker model showing the smooth skin mesh. Feathers are not shown to better illustrate the anatomy of the wings.

billed woodpecker. Here, it has been unfolded out of the unnatural pose shown in Figure 4.1 into a "neutral pose" from which it is easy to animate. Wang subsequently added flight feathers modeled as NURBS surfaces to the wings, and cleverly used animation techniques for rendering fur to approximate the appearance of plumaceous feathers on the body. Figure 4.3 shows Wang's digital Ivory-billed woodpecker model successfully posed to match a video of a Pileated woodpecker in flight. Our model makes use of Wang's bird's body, but not the feathers because the NURBS feathers of this model were not morphologically accurate.

Of particular importance in Wang's woodpecker model and rig is the physiological accuracy of the patagium. The patagium is an elastic area of skin near the elbow which connects the shoulder and wrist joints. The patagium is stretched taught when the wing is extended and provides important aerodynamic functionality by maintaining an airfoil cross section of the wing in this elbow area. Figure 4.4 illustrates the function of the patagium by comparing the patagium in the

Figure 4.3: Comparison of Wang's digital model to actual video. Left: A still-frame from a video of a Pileated woodpecker in flight. Right: The digital Ivory-billed woodpecker with NURBS feathers posed to match.[WBL+08]

rendered model to that of a Pileated woodpecker specimen.

Wang scripted a procedural rigging algorithm to control the patagium and simulate its natural motion. The animator now only has to be concerned with posing the shoulder, elbow, and wrist joints. The patagium will automatically assume the proper shape as controlled by Wang's algorithm.

Because the bird in our investigation is not an Ivory-billed woodpecker, this model cannot be used without modification. However, it is a remarkable model for its morphological accuracy, and we can take advantage of the fact that most birds share nearly identical anatomical structure, varying only in the size and length of certain bones. By scaling the rig of the Ivory-billed woodpecker model as a whole as well as scaling individual arm bones, we can closely represent a Red-winged blackbird at the proper scale and with all the degrees of freedom of motion necessary for animating any bird.

4.2 Scanning and Construction of Flight Feathers

While the body of our Red-winged blackbird can be digitally reconstructed based on another species, the feathers are unique. Feather shapes, sizes, and even num-

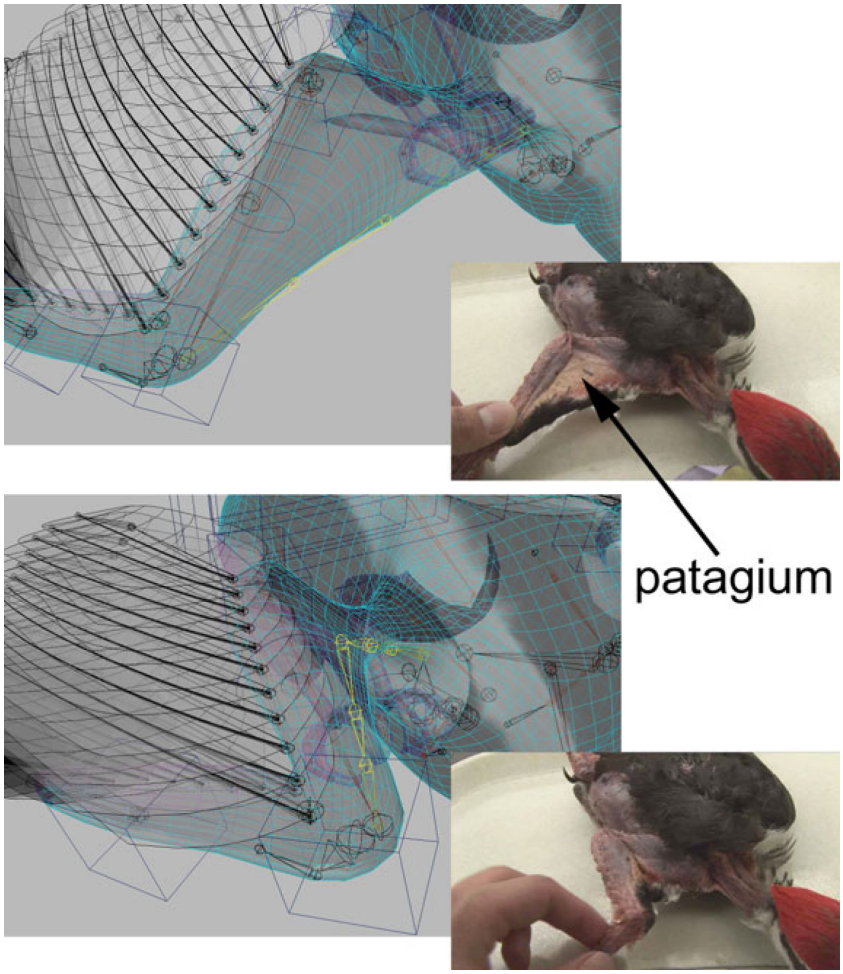

Figure 4.4: Functionality of the patagium. In the top view the wing is extended and the patagium stretched taught. In the lower view, the wing is retracted and the patagium folds into the shoulder. The inset shows the wing of specimen Pileated woodpecker for comparison to the digital model.[Wan07]

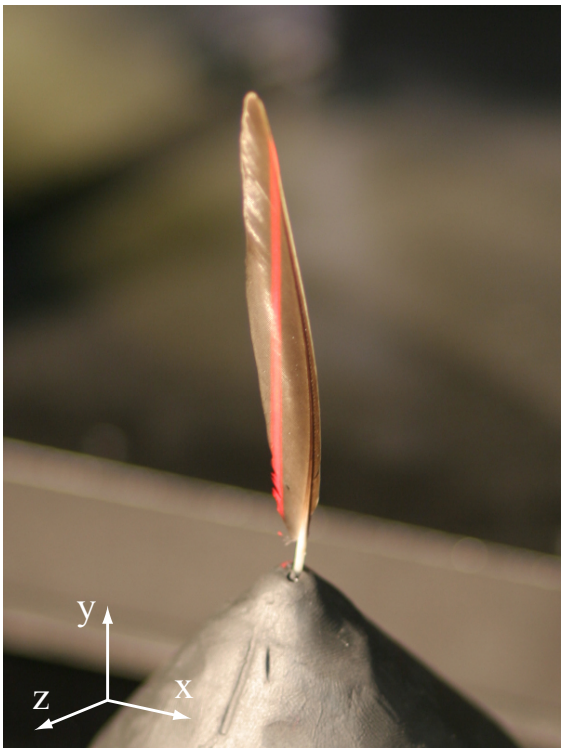

Figure 4.5: Laser scan of the first primary feather of a Red-winged blackbird in progress on the Cyberware Modelshop scanning table.

bers vary across bird species and therefore it is important that we model our digital feathers on the feathers of an actual Red-winged blackbird. Because feathers comprise most of the surface area of the wing, with the patagium and skin of the arm making up the rest, we took special care to model the geometry of the feathers as accurately as possible. Even slight changes in the geometry of the wing can dramatically affect the aerodynamics.

4.2.1 Laser Scanning

Using the feathers from a female Red-winged blackbird window-kill specimen, we scanned each feather individually using a laser ranging scanner. The scanner we used was a Cyberware 3030 Scanhead in conjunction with Cyberware's actuated Modelshop table. With position encoders embedded in the table, the scanhead is

Table 4.1: Cyberware scanner resolution

Dimension	Resolution
X	0.1 mm
Y	1 mm
Z	0.1 mm

rigidly mounted while the table can move in two degrees of freedom (lateral, and rotational). Our scans were conducted by mounting the feather on a clay pedestal about four inches from the front of the scanhead enclosure. The feather was oriented vertically and normal to the scanhead as to appear as broad as possible.

Figure 4.5 shows a scan in progress. A vertical beam of 650 nanometer light sweeps across the feather as the Modelshop table moves laterally. The time for the light to return to the sensor is measured and a distance from the sensor to each point is calculated. For the purposes of the scans, the X direction is along the lateral track of the table's motion, parallel to the vanes of the feather. The Y direction is up, along the rachis. The Z direction is away from the scanhead, perpendicular to the vanes. The scans were conducted at the maximum possible resolution as indicated in Table 4.1.

While the resolution of the scanner is very high, it also gives a very noisy output. This is likely due in part to the irregular nature of the feather. It is not a smooth and well behaved object with a uniform reflectance profile. Instead, it is a complex object comprised of microfeatures with subsurface structures, where light does not reflect cleanly back to the sensor. Edges are especially problematic because of scattering effects where the vane becomes thin. The result is an often jagged and discontinuous mesh whose overall geometry and curvature represent the feather well, but whose small scale features must be filtered. Comparing the photographic representation to the rendered raw scan of the first primary feather in Figure 4.6, we see that general curvature is quite accurate, but there is a great

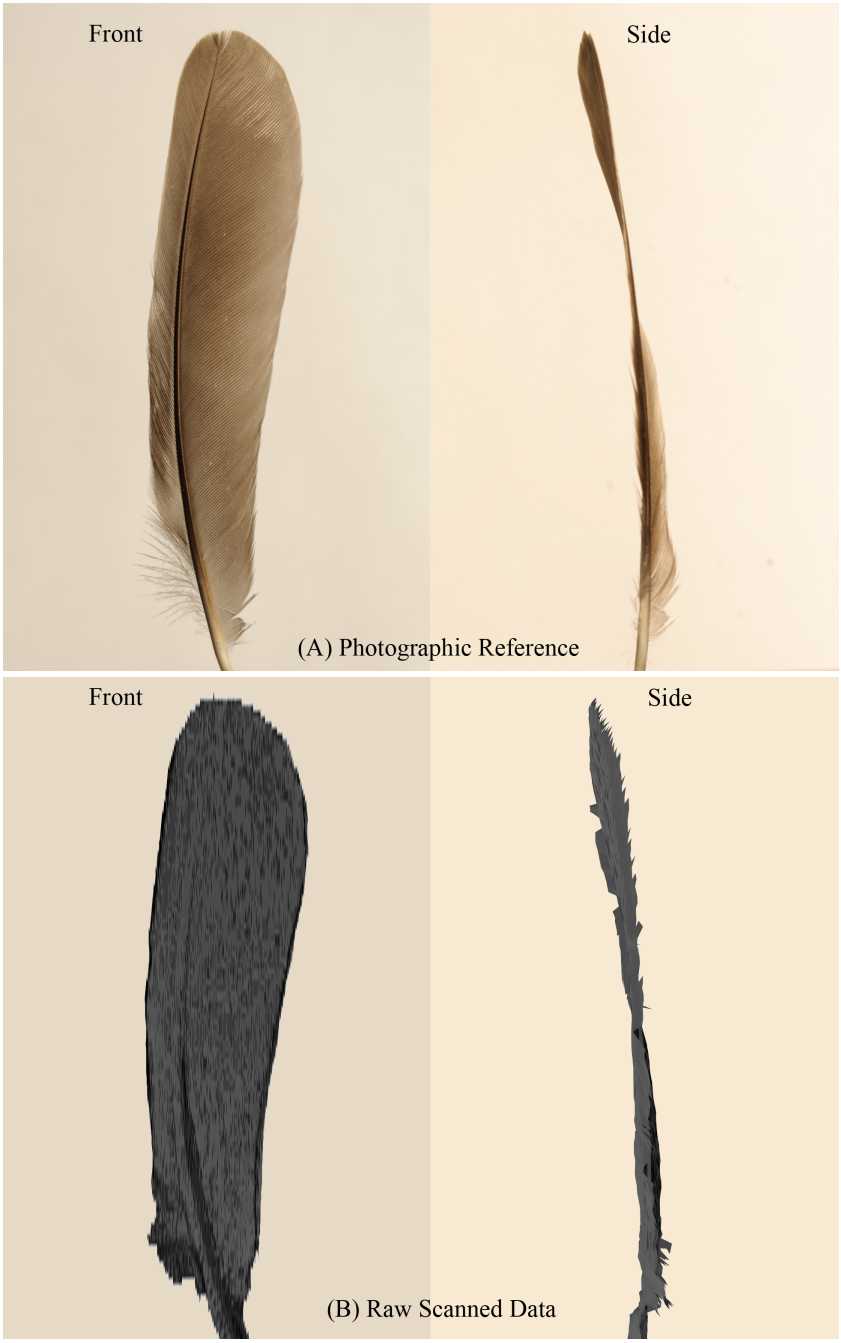

Figure 4.6: Photographic and digital comparison of the first RWBB primary feather. (A) Shows reference photographs of the feather from the front and side. (B) Shows the rendered point cloud data of the feather obtained from the scanning process shown from the front and side.

Figure 4.7: Photograph of the RWBB first primary feather showing the traced outline used to define the edges of the three-dimensional mesh

deal of high frequency noise.

4.2.2 Processing Feather Data

Through a series of smoothing operations and reprojections, we can modify the noisy and dense raw data mesh into a smooth and well ordered polygonal mesh.

We begin processing the raw scanned mesh by manually deleting the particularly egregious vertices around the edge. Next we iteratively smooth the mesh by averaging vertices locally just enough to damp out the high frequency noise without altering the overall geometry or curvature. Next we trace a series of NURBS curves across the smoothed mesh. The goal is to replace the high resolution polygonal

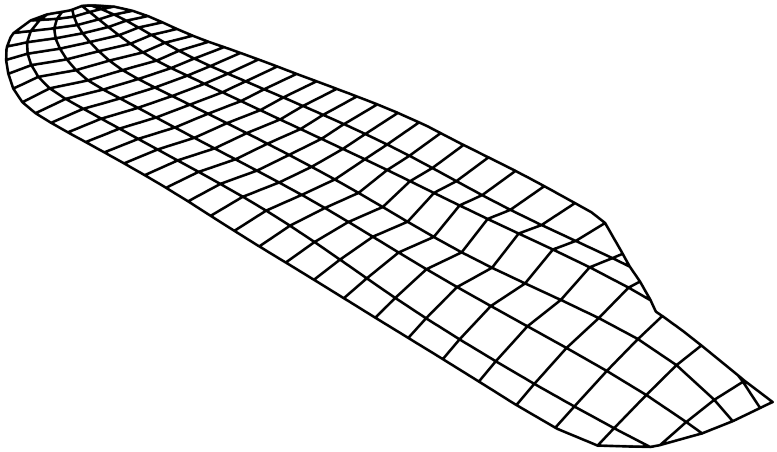

Figure 4.8: Final polygonal feather mesh

mesh with a NURBS surface. We ultimately convert the NURBS surface back to a polygonal mesh for analysis, but having this intermediate NURBS surface allows us to control the feather's tessellation and topology. For each feather we manually trace the boundary of the vanes with NURBS curves (Figure 4.7) and project these curves onto the surface. After trimming away the surface outside these curves, we are left with the reconstructed feather defined as a parametric surface. The isoparametric lines and defining tessellation are oriented along the principal axes of the surface. This allows the creation of relatively uniform polygons. Evenly spaced and unskewed polygons will be useful for aerodynamic computations.

Figure 4.8 shows the final polygonal mesh of a typical feather. Its curvature and geometry accurately reflect that of the original specimen. Because of the NURBS representation, the polygonal resolution is variable and can be refined or coarsened for more accurate or faster simulations, respectively. Figure 4.9 shows the first primary feather, comparing the photographic reference to the processed polygonal mesh.

Repeating this process for each of the eighteen feathers gives a complete picture

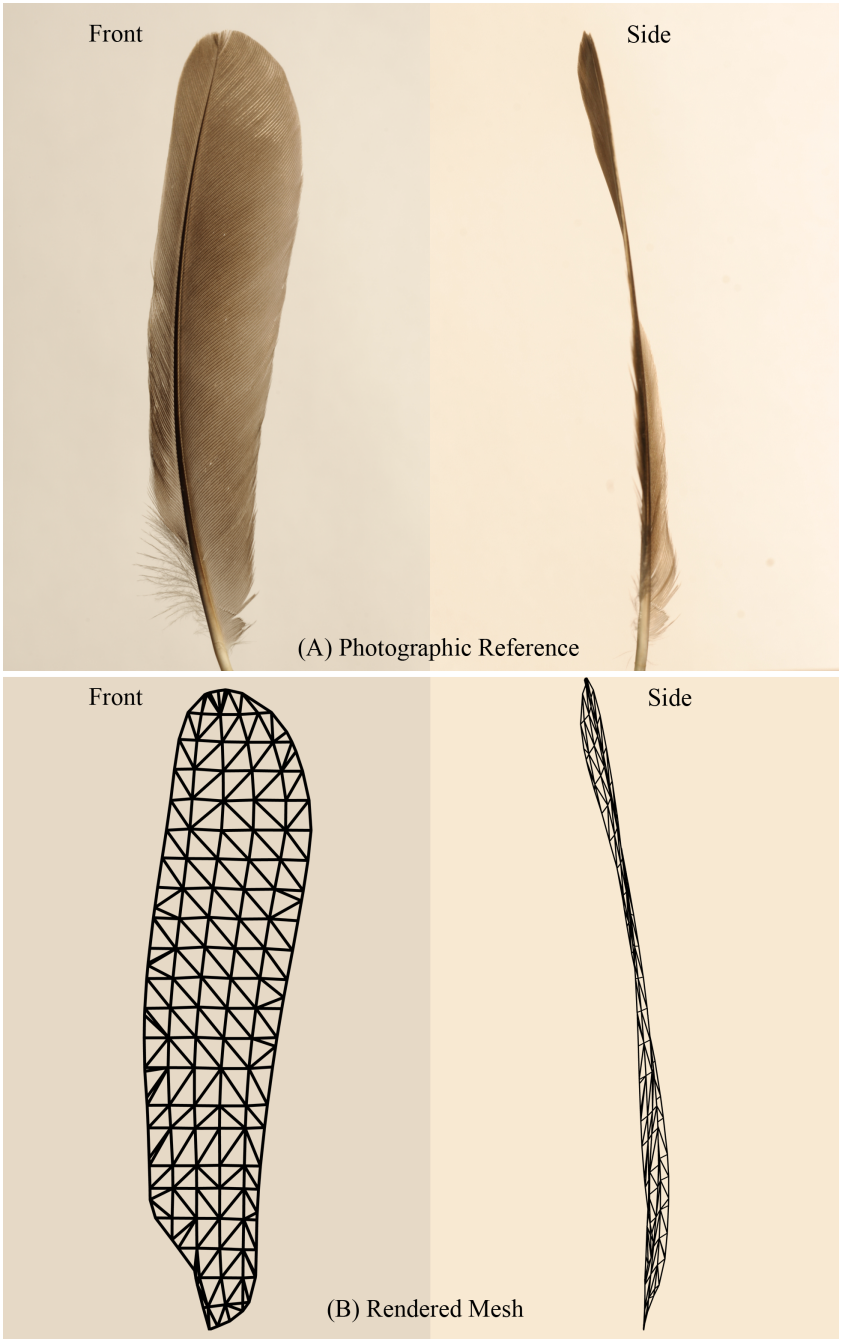

Figure 4.9: Photographic and digital comparison of the first RWBB primary feather. (A) Shows reference photographs of the feather from the front and side. (B) Shows the rendered smoothed and processed polygonal mesh from the front and side.

of the wing. Figure 4.10 shows a lineup of each Red-winged blackbird flight feather.

Figure 4.10: Complete set of digitized feathers of the Red-winged blackbird

4.3 Motion Capture

For the kinematic data describing the motion of a Red-winged blackbird wingbeat, we utilize the motion capture work done by Brendan Holt in 2009[Hol09]. This work focused on the high speed motion capture of birds flying in a flight tunnel. Distinct from a wind tunnel, a flight tunnel is not powered by fans and the bird flies through still air. Its motion is recorded by multiple cameras as it flies through a test section of the tunnel. By using two cameras to track retroreflective markers placed on the bird, Holt was able to obtain accurate joint kinematic data for one complete wingbeat using direct linear transformation methods (DLT).

Wild birds were captured through the use of mist nets, were flown in the tunnel, and then released in the location they were caught. While Holt's work experimented with a number of different species of birds, a female Red-winged blackbird provided the best results. Birds were handled according to IACUC protocol 2001-0051 under the supervision of Cornell University ornithologist Dr. Kimberly Bostwick[Hol09].

The thirteen meter long flight tunnel, located at the Cornell University Ex-

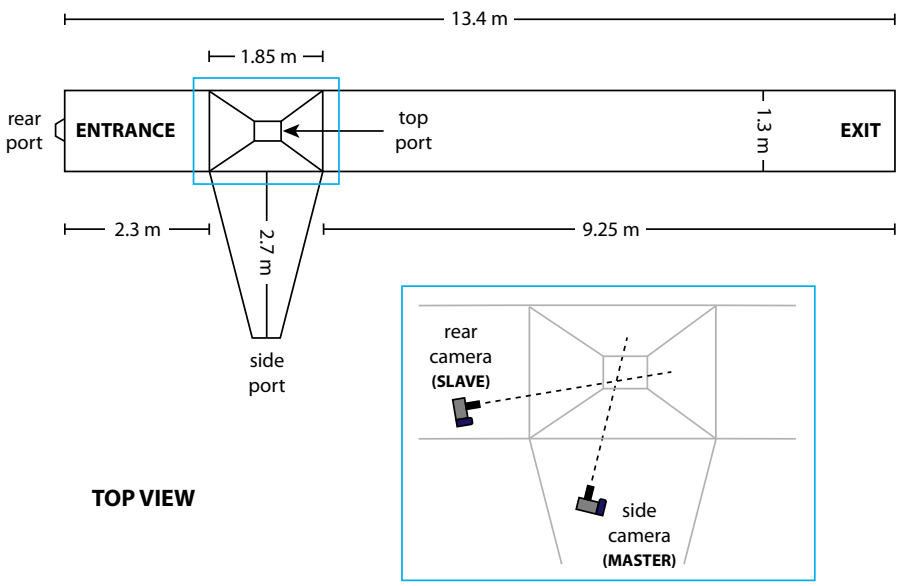

Figure 4.11: Cornell University flight tunnel schematic showing the locations of the two high speed cameras used to record the Red-winged blackbird in free flight[Hol09]

perimental Ponds, provided an optimal environment for observing a small bird in free flight (Figure 4.11). The bird was introduced through the rear of the tunnel and flew towards the sunlit exit, where it was recaptured in mist netting.Two cameras recorded the flight of the bird at five-hundred frames per second. These two vantage points later allowed the motion of the wing to be reconstructed in three dimensions. A large amount of lighting was needed to illuminate the markers on the bird at such high framerates. Several halogen floodlamps were used to illuminate the inside of the tunnel. Figure 4.13 shows several superimposed images from the side camera of the recorded flight. Before each test the cameras were calibrated though the use of a calibration cube, which is necessary to specify coefficients of the DLT algorithm.

Figure 4.12 shows the test specimen with retroreflective markers attached. These three millimeter in diameter markers were cut out from commercially available adhesively backed 3M tape. Because the tape is thin and weighs relatively

Figure 4.12: Underside of the Red-winged blackbird test subject showing nine retroreflective markers on the wing, four on the body, and one on the tail.[Hol09]

little, it had a negligible impact on the flight of the bird. Non-permanent adhesive allowed the bird to pick the markers off after the flight. The bird was marked in nine places on each wing surface, top and bottom.

Using software techniques developed by Ty Hedrick[Hed08], Holt was able to reconstruct the positions of the wing markers on the bird. Hedrick's software methods make use of the DLT algorithm for triangulating the position of points in three dimensions from multiple two-dimensional camera views. This method was first introduced by Abdel-Aziz and Karara in 1971[AAK71].

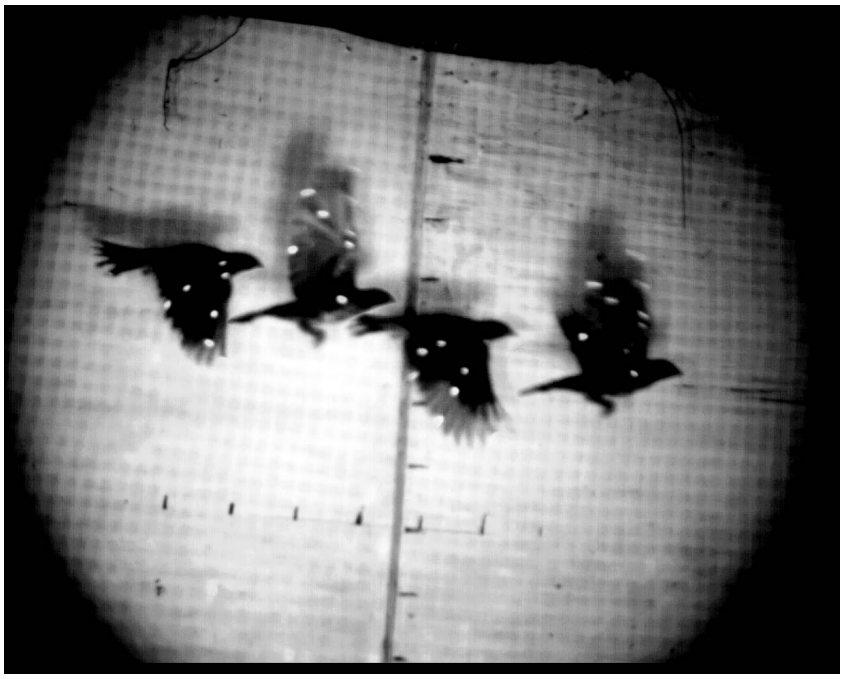

Figure 4.13: Four superimposed frames from the side camera showing the bird at the top of its upstroke and bottom of its downstroke for two wingbeats. The wing markers are clearly visible.

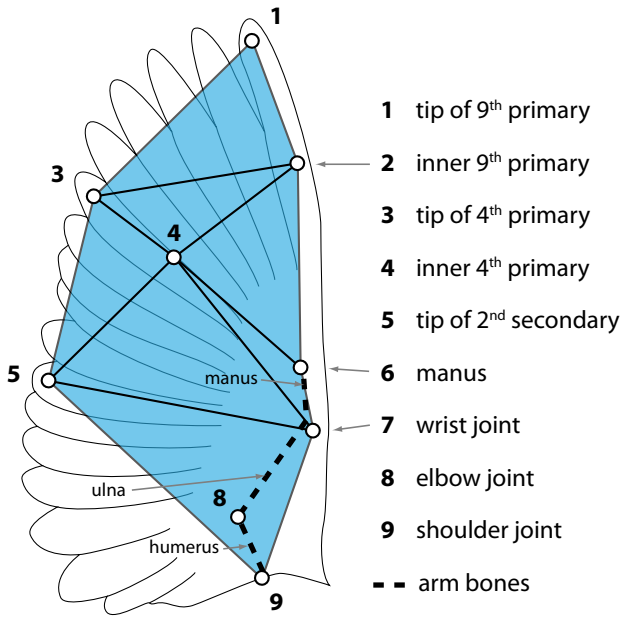

Figure 4.14: Virtual mesh showing the positions of markers on the wing in relation to the arm bones and feathers[Hol09]

The resulting wingbeat kinematics gave numerical three-dimensional positions for each wing marker over the seventy-seven millisecond long wingbeat. Although it is impossible to know positions of all markers with complete precision, the DLT algorithm takes an error-minimization approach and results in the best possible analysis of the data.

Figure 4.14 shows a basic geometric mesh constructed from the wing markers. Animating this mesh yields the time slices shown in Figure 4.15. Here we can clearly see the extension of the wing at the top of the upstroke, the forward sweeping motion of the downstroke, and the way the wing folds up to make itself smaller as it begins the upstroke.

4.4 Feathering the Model Wing

With the coarse mesh describing the wing motion obtained from the markers, the final step in recreating the wingbeat is to substitute individual feathers into the RWBB model. To do this, we constrain each feather such that it is parented to the joint hierarchy of the wing. The positions of the primary feathers are constrained to the virtual wrist bone, and the positions of the secondary feathers are constrained to the virtual radius and ulna bones. As for rotations, the ninth primary feather is oriented to the rotation of the wrist bone and the ninth secondary feather is oriented to the rotation radius and ulna bones. The orientations of the feathers between these two extremities are smoothly blended between the two. This gives an accurate model of feather movement as the wing opens and closes.

Figure 4.16 shows the substitution of polygonal feathers into the RWBB model. Only the shoulder and arm of the bird's geometry are shown here. The arm of the bird has been posed to match the position given by the markers for one instant in time. Figure 4.16a shows the coarse mesh of the markers relative to the arm.

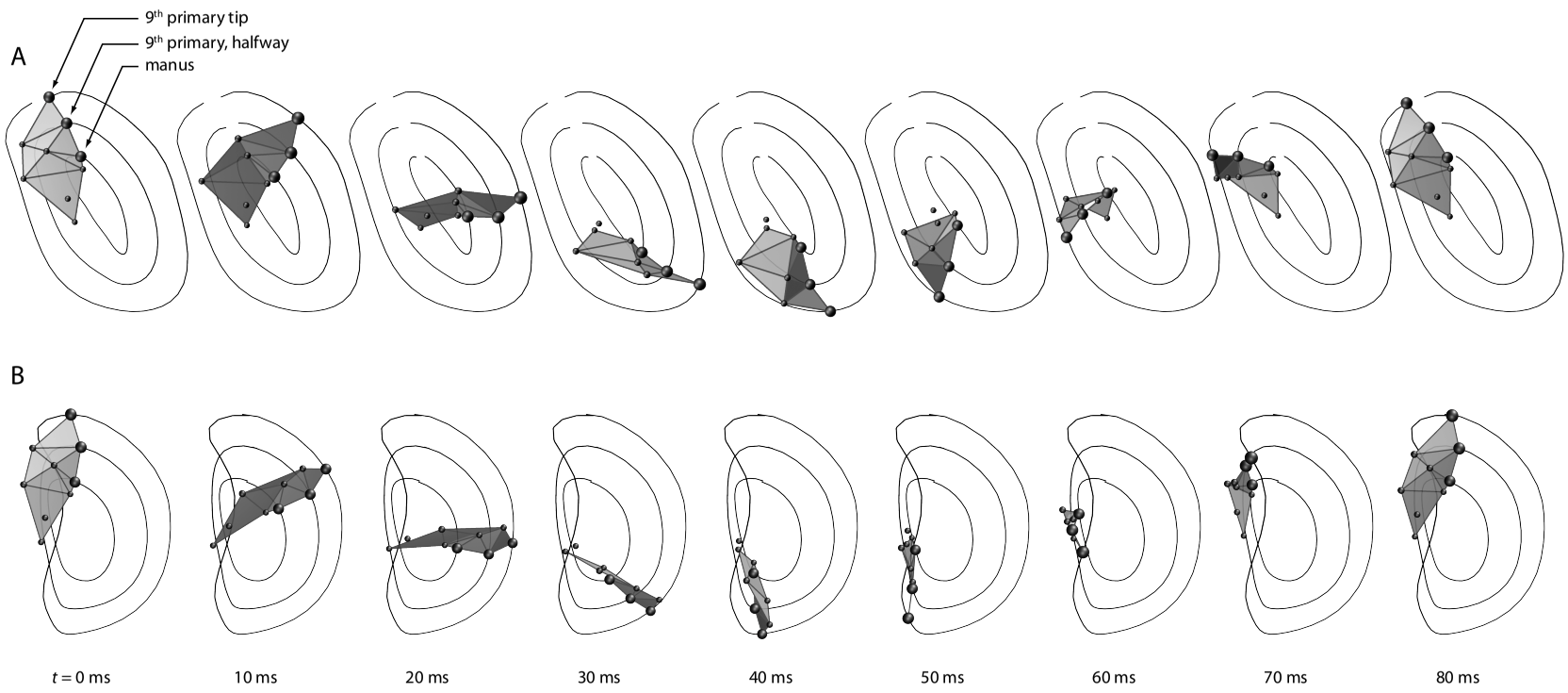

Figure 4.15: Digital wing mesh shown at ten millisecond intervals over the wingbeat. Motion trails indicate the paths of the markers. The top row of images (A) shows the side view of the bird. The lower row of images (B) shows the view from the rear.[Hol09]

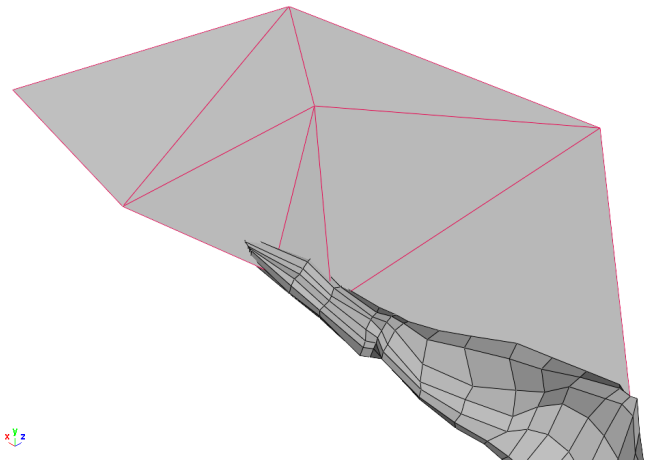

(a) Wing marker coarse mesh

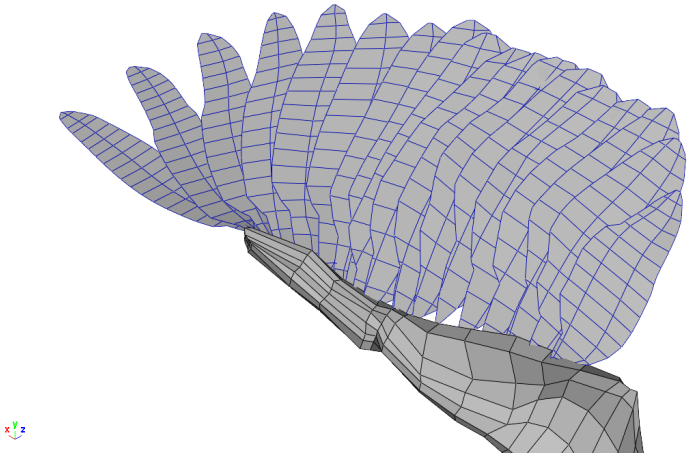

(b) Polygonal feathers

Figure 4.16: Red-winged blackbird model wing posed to fit kinematics. The wing is represented as a coarse mesh created from marker locations and also individual feather meshes. The bird's shoulder is located in the lower right of each frame.

In Figure 4.16b the coarse mesh is replaced by the individual polygonal feather meshes, which give a good representation of the shape of the coarse mesh while adding finer detail.

CHAPTER 5

AERODYNAMIC ANALYTIC METHODS

With the wing geometry and kinematics of a Red-winged blackbird wingbeat fully defined, we will attempt to simulate the aerodynamic forces on the wing during the wingbeat. Three different approaches were explored, each with its own unique set of challenges. First, a numerical simulation approach was taken using computational fluid dynamics (CFD) software. The geometric complexity of the model wing proved itself a formidable obstacle. Rather than simplify the geometry and sacrifice precision we experimented with a second method; wind tunnel testing. By using a three-dimensional rapid prototyping machine to print a plastic wing, we were able to measure the forces on this plastic wing in a wind tunnel. However, working with a rigid plastic model lacked the deformability of a flapping wing. In addition, working within the constraints of the rapid prototyping machine sacrificed precision and added complexity to the workflow. Finally, a quasi-numerical blade element simulation was implemented to model the bird wing. This method had the advantage of being able to approximate the non-linear and unsteady velocity field and flow conditions, as well as the non-rigid deformation of the geometry. This chapter presents this blade element method and our modifications to the traditional model. We will detail how how coefficients were chosen, the vector math required for simulation in three dimensions, and the additional mathematical terms influenced by insect flight studies.

5.1 Computational Fluid Dynamics

Computational fluid dynamics (CFD) is the analysis of fluid flow using numerical iterative solvers. The technique requires a mesh of the fluid domain, and uses finite volume methods to solve the complete Navier-Stokes equations. These methods are

similar to techniques used in finite element analysis (FEA) to solve for mechanical stresses in structural mechanics. CFD offers the potential of fully solving the problem, obtaining the complete velocity and pressure fields numerically. The CFD method is widely used in the aerospace industry as it is the most accurate method of solving for forces on a body. Modern CFD software is capable of simulating complex compressible, supersonic, and turbulent flows. However, the algorithms are highly computationally expensive, often taking minutes or hours to solve simple problems. In addition, CFD solvers often stumble over intricate geometries and non-rigid bodies. The software we used in our CFD tests is FLUENT, by ANSYS Inc.[1]

Before ever attempting to run even a steady state simulation of our wing in FLUENT, we first had to modify the wing geometry to be compatible with the software. This proved to be a difficult process. Because our digital feathers are defined as infinitesimally thin surfaces, we needed to give them volume in order for FLUENT to recognize them as a solid boundary. This was solved by extruding each digital feather by one millimeter, and then rounding the edges. Figure 5.2 shows the mesh of one of these converted feathers. The feathers were given rounded edges to avoid sharp pressure gradients, a phenomenon which occurs around sharp edges and can cause the solver to fail. Unfortunately, the thickness and roundness of the feathers detract from their physical accuracy.

To convert a series of thick feathers into a wing, we performed a series of boolean operations which intersected the surfaces of the feathers with each other to create one continuous surface (Figure 5.1). Care was taken to ensure that the elements within the mesh were small enough and of sufficient resolution for the solver to accurately converge on a solution. Too much mesh resolution will needlessly increase computation time without contributing to improved accuracy.

[1]FLUENT version 6.3.26. URL: http://www.ansys.com/products/fluid-dynamics/fluent/

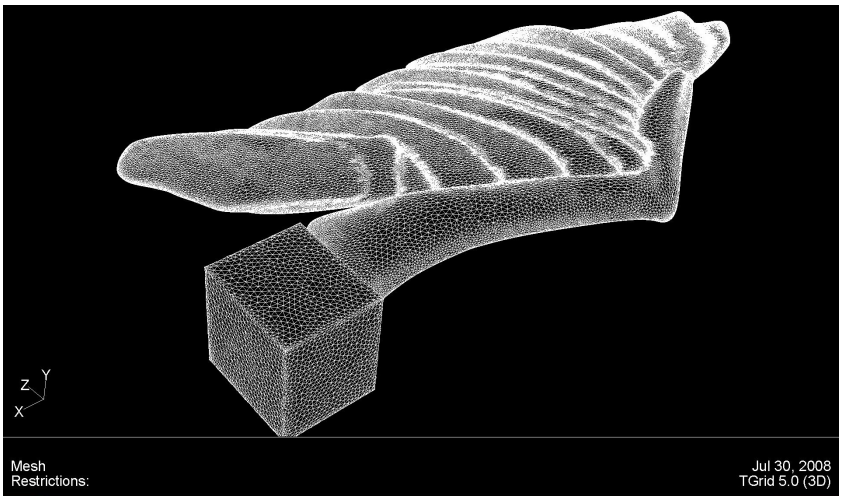

Figure 5.1: Surface mesh of a wing with merged feathers for use in FLUENT

While we were able to create a surface mesh of the wing, meshing the fluid volume proved too complex a task. FLUENT's mesh and grid creating software package TGRID was unable, after repeated attempts, to create a volume mesh around such a complex three-dimensional structure. Several proof of concept simulations were run on three-dimensional single feathers, as well as on two-dimensional slices of the wing. The result of one of these tests on a single feather is shown in Figure 5.2.

CFD, while powerful, does not fulfill our needs. Even if TGRID managed to create a mesh to simulate the wing, commercial CFD software is ill-equipped to handle the non-linear deformation of the surface that is required to accurately simulate the kinematic behavior of the wing. For all geometric configurations of a moving surface, the software would need to recompute the volume mesh to account for the changes in boundary geometry. This is a non-trivial problem, which FLUENT's deformable mesh capabilities could not handle.

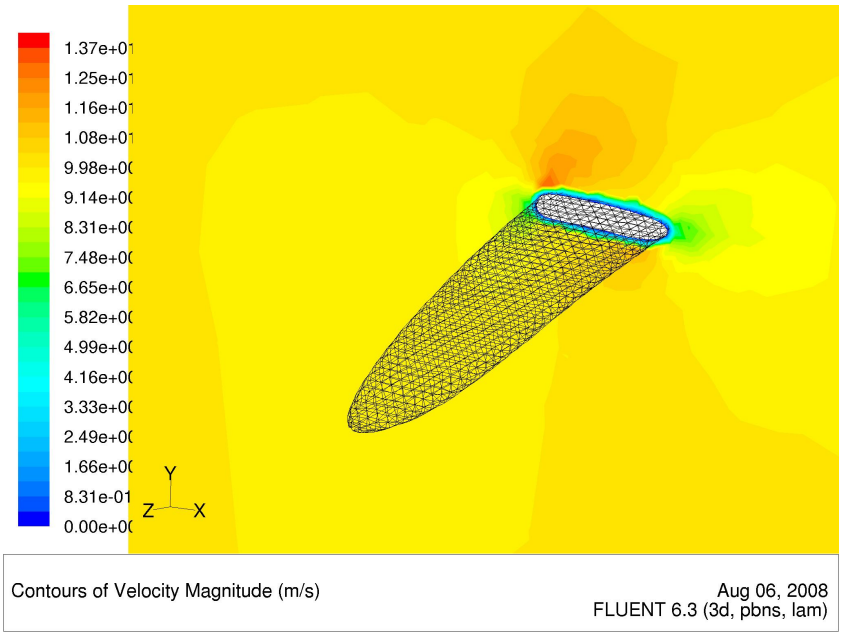

Figure 5.2: Three-dimensional CFD solution showing a slice of the velocity field around a single feather

5.2 Wind Tunnel Testing

Wind tunnel testing offers a physical analog to CFD's virtual simulation. By taking the same wing model used in our CFD meshing attempts and printing it, we were able to test the physical geometry in a wind tunnel.

Using a Stratasys Inc. Dimension 1200ES 3D Printer, we printed our model wing in ABS plastic. The Dimension 1200ES printer allows printing of parts within a ten by ten by twelve inch volume. The printer builds parts by depositing layer upon layer of plastic one-tenth of an inch thick. The active printing volume allowed us to print the wing at actual size, and thus no Reynold's number conversion was needed.

Mounting this plastic wing in a wind tunnel, we were able to measure external forces on the wing. We utilized Cornell University's custom four-foot wind tunnel[2].

[2]Harley-Davidson Laboratory, Sibley School of Mechanical and Aerospace Engineering, Cornell University

Figure 5.3: Computer rendering of the model wing which was printed in plastic by a rapid prototyping machine

This tunnel has a four-foot by four-foot test section with a fifty-foot flow development section behind a honeycomb inlet. The wind tunnel was also equipped with a helium bubble generator and strobe light used to visualize the flow. By injecting small (on the order of one millimeter) helium-filled neutrally buoyant soap bubbles into the flow and illuminating them with the strobe light, one can visualize the path taken by the fluid around the test object. The wing was mounted on a JR3 Inc. 20E12A six-degree-of-freedom strain gauge force balance. The analog signal from the force balance was converted to a digital signal, filtered, and recorded by computer.

Wind tunnel analysis is traditionally used to experimentally determine forces on scaled down models of aircraft. In order to maintain the same Reynold's number as the expected flight regime, the airspeed of the wind tunnel is increased in inverse proportion to the model scale. By printing an actual size model, we had no such scaling issues with the Reynold's number regime; however, the limitations inherent to wind tunnel testing and the rapid prototyping printing process provided their

Figure 5.4: Plastic printed wing mounted on stand in wind tunnel for testing

own insurmountable difficulties.

The largest obstacle that we sought to overcome was the limitation of only being able to conduct steady-state experiments. One approach to accurately portray the detailed kinematic motion described in Section 4.3 is to run a number of experiments on differently shaped wings. By recording the forces on each wing we could create a quasi-steady state database of forces that could be input into the kinematic model. We could do this by printing a plastic wing for each geometric wing-shape described by the kinematics, and recording the forces on each of these wings in the wind tunnel throughout the complete range of angles of attack. However, we were hampered by the monetary cost and time investment involved in printing a number of such wings. Printing one wing takes roughly forty-eight hours. Even with such a library of printed wings, it is unclear exactly how to map the recorded forces at different wing-shapes and angles of attack to the forces acting on the kinematic model of the wing. Our goal was to obtain instantaneous forces on the wing and integrate them over the wingbeat for a discreet number of poses in the wingbeat cycle to determine the total momentum transferred to the

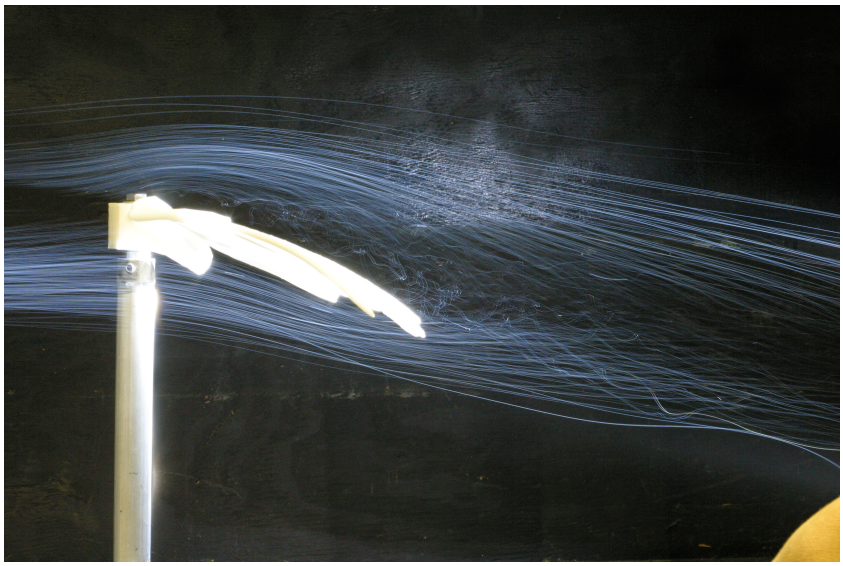

Figure 5.5: Plastic wing in wind tunnel with streaklines illuminated by helium bubbles

bird from the air. Since different polygons of the kinematic wing have different instantaneous velocities and angles of attack, there is no clear look up into the force values recorded at the wind tunnel.

Furthermore, we were limited by the rapid prototyping process itself. The ABS plastic printed by the machine is brittle, and care must be taken to add enough geometric thickness to the model so that it will not break. Similar to the CFD meshing process, this thickening of the wing detracts from the wing's physical realism. The surface of the printed model is also rough where the many layers of plastic one-tenth of an inch thick join each other on the model. This roughness disrupts airflow and causes boundary layer separation. The plastic can be sanded smooth if handled carefully, but in trying to maintain the realism of gaps between certain feathers there will always be areas of the model unreachable for sanding. Finally, we are limited by the scale of the prototyping volume. By printing a larger model it may be possible to avoid the problems of roughness and thickness of the plastic; however the size would still be limited to the ten by ten by twelve inch

printing volume.

5.3 The Basic Blade Element Model

Looking for a faster simulation method than CFD and more dynamic simulation method than wind tunnel testing, we turned to the blade element (BE) model, described in Section 2.2. Free of the constraints of a fully-numeric computer simulation and physical experiments, the blade element model provides a quasi-numeric framework in which to compute instantaneous forces on differential areas of the wing. By analyzing the wing as a geometric mesh of quadrilateral elements, we can treat each element as a differential flat plate and sum the combined aerodynamic forces acting on each small plate.

$$L' = \frac{1}{2}\rho U^2 C_L(\alpha)\, c \tag{5.1}$$

$$D' = \frac{1}{2}\rho U^2 C_D(\alpha)\, c \tag{5.2}$$

Recall from Chapter 2.2.4 that the formulas for the lift and drag forces on a two-dimensional blade element are given by Equations 5.1 and 5.2, where ρ is the density of air, U is the airspeed, C_L and C_D are the respective coefficients of lift and drag, and c is the chord length. Figure 5.6 reviews the fundamental blade element directions. Recall that the chord is oriented in the same direction that the airfoil is aiming, and that the relative wind is the total velocity of the oncoming air. The angle of attack is the angle between the chord and the relative wind. It is also important to remember that the lift force acts in a direction orthogonal to the relative wind, while the drag force acts in the same direction as the relative wind.

With a digital model representing each feather, and fully defined kinematics of

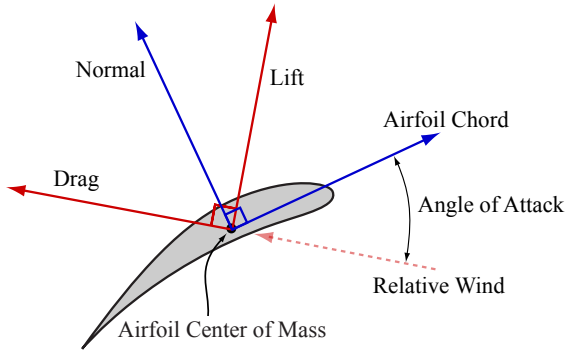

Figure 5.6: Blade element lift and drag forces in two dimensions on a typical airfoil

the wingbeat, we know the velocity and orientation of every face within all of the feathers of the wing throughout the wingbeat. We can then take each polygonal face as an individual blade element and compute the instantaneous lift and drag force acting on that element at a given time. By summing the force acting on every element, we can obtain a net force on the bird. This Riemann sum type of integration is described in detail in Section 5.6. Until that section, we will focus on the forces on a single element. In the following sections we review the coordinate systems of a blade element, the lift and drag coefficients, and the additional force terms besides lift and drag which act on a blade element.

5.3.1 Two-Dimensional Coordinate System

The blade element model is a two dimensional model. Figure 5.7 shows the two relevant coordinate systems used in computing the forces on a blade element.

The first is the blade element velocity coordinate system defined by unit vectors $\hat{\mathbf{x}}_v$ and $\hat{\mathbf{y}}_v$. This represents the frame of the moving blade element oriented relative to the oncoming airflow. The velocity of fluid is in the $-\hat{\mathbf{x}}_v$ direction. The external aerodynamic forces act in this coordinate frame. Lift acts in the $+\hat{\mathbf{y}}_v$ direction,

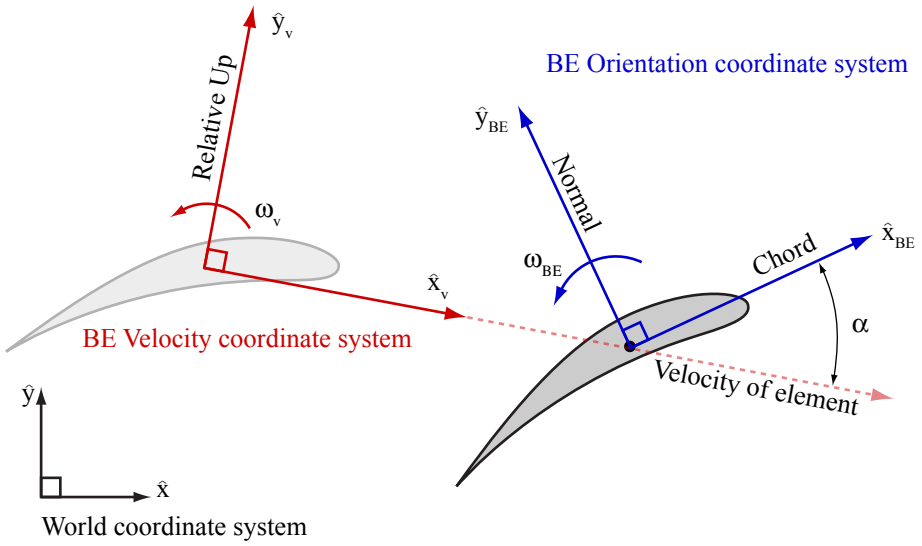

Figure 5.7: The two different frames of reference used in the blade element model

which represents the relative up direction. Drag acts in the $-\hat{\mathbf{x}}_v$ direction, the direction of fluid flow. Because circulation will play an important factor in lift generation, the rotational velocity ω_v of this frame is also important.

Table 5.1: Coordinate system axis labels

Unit Vector	Full Name
$\hat{\mathbf{x}}_{BE}$	Chord
$\hat{\mathbf{y}}_{BE}$	Normal
$\hat{\mathbf{x}}_v$	Velocity
$\hat{\mathbf{y}}_v$	Relative Up
α	Angle of Attack

Next, the blade element orientation coordinate system is defined by unit vectors $\hat{\mathbf{x}}_{BE}$ and $\hat{\mathbf{y}}_{BE}$. This frame of reference describes the orientation of a blade element by defining its chord and normal directions. The chord is the vector created between the trailing edge and leading edge, and indicates the direction the element is aiming. The chord is represented by the axis $+\hat{\mathbf{x}}_{BE}$, and the direction of the face normal is indicated by $+\hat{\mathbf{y}}_{BE}$. The rotational velocity of this frame is ω_{BE}.

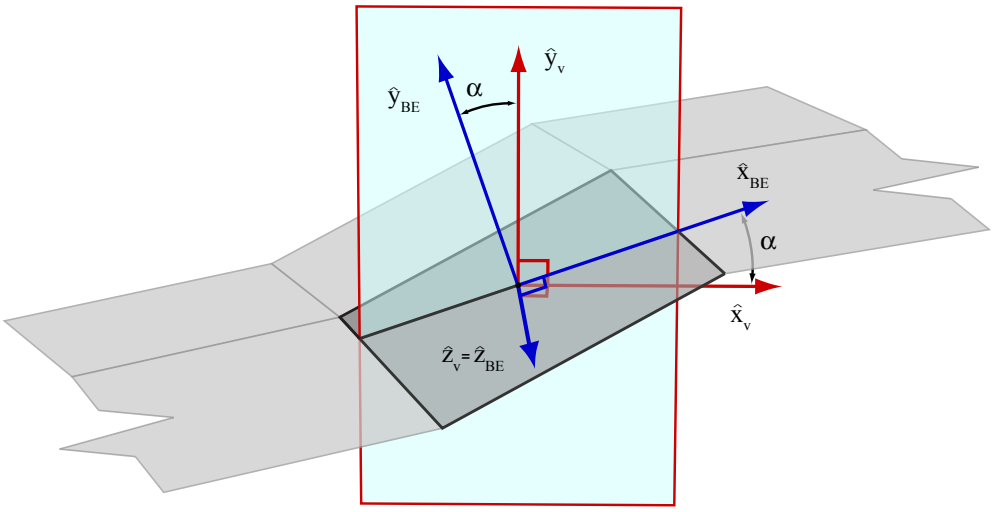

Figure 5.8: Projecting a three-dimensional face into a two dimensional blade element

The angle of attack is the angle between the chord and airflow velocity, or $\hat{\mathbf{x}}_{BE}$ and $\hat{\mathbf{x}}_v$. When we wish to indicate the change in angle of attack with respect to time, we use $\dot{\alpha}$ instead of ω, and define $\dot{\alpha}$ as $\dot{\alpha} \equiv \omega_{BE} - \omega_v$. Table 5.1 lists the common names associated with the axis variables to avoid confusion.

5.3.2 Extension to Three Dimensional Coordinate System

Although our polygonal elements are three dimensional, we can project them into the two dimensional coordinate systems described in Section 5.3.1 in order to fit the blade element model. Figure 5.8 shows the way in which a polygon is sliced by a vertical plane in the direction of fluid flow in order to build the blade-element-centric and velocity-centric coordinate systems. Knowing only the normal and the velocity of the face, we use vector mathematics to construct the remaining principle axes and determine the angle of attack.

The face normal $\hat{\mathbf{y}}_{BE}$ is implicitly defined, and the face velocity $\mathbf{U}$ is computed

using a central finite difference approach by comparing the positions of a face at timesteps immediately preceding and proceeding the current time. Dividing velocity by its magnitude (Equation 5.3) gives us the unit vector $\hat{\mathbf{x}}_v$ which is the direction of the fluid flow relative to the face.

$$\hat{\mathbf{x}}_v \equiv \frac{\mathbf{U}}{\|\mathbf{U}\|} \tag{5.3}$$

Next, we wish to determine the chord direction $\hat{\mathbf{x}}_{BE}$. To determine the chord we must first build the rest of our coordinate systems by defining a binormal direction $\hat{\mathbf{z}}_{BE}$. Then, we can compute the chord $\hat{\mathbf{x}}_{BE}$, the fluid up vector $\hat{\mathbf{y}}_v$, and finally determine the angle of attack α. In Equation 5.4 we define the binormal vector by crossing the velocity with the normal. This z direction in the the blade element coordinate system is also the same in the fluid flow coordinate system ($\hat{\mathbf{z}}_{BE} = \hat{\mathbf{z}}_v$) however we will use the blade element subscript for simplicity.

$$\hat{\mathbf{z}}_{BE} = \hat{\mathbf{x}}_v \times \hat{\mathbf{y}}_{BE} \tag{5.4}$$

We calculate the direction of the chord $\hat{\mathbf{x}}_{BE}$ by crossing the normal with the binormal (Equation 5.5). This gives us a vector which is coplanar with the face but oriented in the direction of the face's velocity.

$$\hat{\mathbf{x}}_{BE} = \hat{\mathbf{y}}_{BE} \times \hat{\mathbf{z}}_{BE} \tag{5.5}$$

Finally, by crossing the binormal with the chord, we obtain the relative up direction of the fluid flow $\hat{\mathbf{y}}_v$ (Equation 5.6). This is the direction in which the lift force acts on the face.

$$\hat{\mathbf{y}}_v = \hat{\mathbf{z}}_{BE} \times \hat{\mathbf{x}}_v \tag{5.6}$$

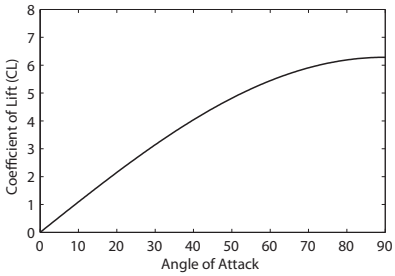

Figure 5.9: Theoretical lift coefficient curve of a flat plate

With these principle unit vectors defined for both the blade element and fluid velocity coordinate systems, we can calculate the angle of attack. Shown in Equation 5.7, the angle of attack is found by taking the inverse cosine of the dot product between the chord and velocity unit vectors. We use a conditional statement to test whether the airflow is coming from above or below the face and force the angle to be negative when the flow has a negative $\hat{\mathbf{y}}_{BE}$ component.

$$\alpha = \begin{cases} -\cos^{-1}\left(\hat{\mathbf{x}}_{BE} \cdot \hat{\mathbf{x}}_v\right) & \text{if } \left(\hat{\mathbf{x}}_v \cdot \hat{\mathbf{y}}_{BE}\right) < 0 \\ +\cos^{-1}\left(\hat{\mathbf{x}}_{BE} \cdot \hat{\mathbf{x}}_v\right) & \text{otherwise} \end{cases} \tag{5.7}$$

In this section we have described our method of computing the directions in which the blade element forces act, as well as the face velocity $\mathbf{U}$ and angle of attack α, which are inputs into the blade element force model. Now we will turn our attention to the only remaining input to the model, the lift and drag coefficients.

5.3.3 Lift and Drag Coefficient Curves and Values

Lift and drag coefficients are traditionally determined experimentally. Although our wind tunnel efforts proved unsuccessful, we can draw on flat plate theory and the large body of research on animal flight to make educated guesses.

Classical aerodynamic theory defines a flat plate as a symmetric airfoil of zero camber, infinite span, and infinitesimal thickness. For such a theoretical element,

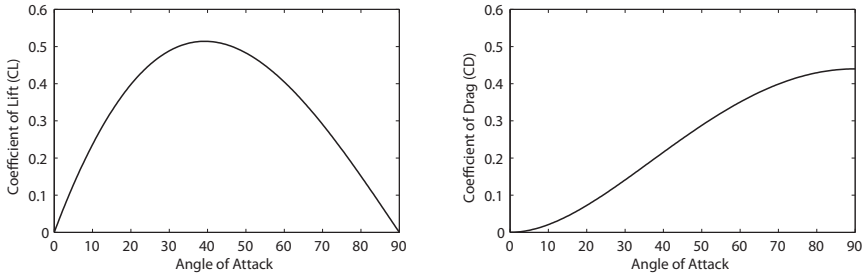

Figure 5.10: Theoretical lift and drag coefficient curves for a stalled flat plate

Bernoulli's law and the Blaussius theorem tell us that the coefficient of lift is defined as $C_L = 2\pi \sin(\alpha)$ (Figure 5.9) [Wit81, And00, WS84, Nor90]. This derivation assumes that the Kutta condition is satisfied, indicating that the flow remains attached to the trailing edge. For small angles of attack this approximation holds true. As the angle of attack increases however, the flow is certain to detach and stall the wing before ninety degrees. Thus, we cannot rely on this theoretical prediction of the lift coefficient due to attached flow.

Theoretical lift and drag predictions also exist for a theoretical flat plate which is stalled from the beginning. This stalled flat plate theory predicts the lift coefficient as $C_L = \frac{\pi sin(2\alpha)}{4 + \pi sin(\alpha)}$, and the drag coefficient as $C_D = \frac{\pi sin^2(\alpha)}{4 + \pi sin(\alpha)}$ (Figure 5.10) [KBD35, WBD04]. In this prediction, the lift coefficient has a periodic dependence on 2α instead of α. Although this theory underestimates the magnitudes of the coefficients, the periodic shape of the coefficient curves reflects experimental values well[WBD04].

Several studies have sought to experimentally quantify the values of the coefficients of lift and drag in greater detail for both insects and birds. Texts generally recognize the maximum coefficient of lift as being between 1.5 and 2.0 [Nor90, WS84]. Weis-Fogh found the maximum lift coefficient to be 1.8 for a hummingbird[WF72]. Whithers experimented with many bird wings and found lower maximum lift coefficients, between 0.8 and 1.2[Wit81]. He found the angles

of attack of maximum lift to be between 8 and 25 degrees.

Although flying at lower Reynold's numbers ($10^2 < Re < 10^3$), insect wings offer valuable insight into the shape of force coefficient curves. Dickinson and Gotz experimented with a low Reynold's number robotic flat plate assembly and found that the coefficient of lift scaled with $\sin(2\alpha)$ and the coefficient of drag scaled with $\sin^2(\alpha)$[DG93]. Experimenting on a robotic fruit fly wing, Sane and Dickinson found the lift coefficient to be $C_L = 0.225 + 1.58\sin(2.13\alpha - 7.2°)$ and the drag coefficient to be $C_D = 1.92 - 1.55\cos(2.04\alpha - 9.82°)$[MHD99, SD01]. Usherwood and Ellington's investigation of several insect wings and a quail wing yielded rough coefficients of $C_L = 1.75\sin(2\alpha)$ and $C_D = 3.0\sin^2(\alpha)$ at Reynold's numbers near the range of bird flight at $Re \approx 5\times10^3$[UE02] (Note the trigonometric identity relevant to C_D curves: $\sin^2\theta = \frac{1-\cos 2\theta}{2}$). Wang et al. found the curves for a fruit fly to be $C_L = 1.2\sin(2\alpha)$ and $C_D = 1.4 - \cos(2\alpha)$[WBD04]. These curve shapes were also confirmed for fruit flies by Dickson and Dickinson[DD04]. Finally, Usherwood investigated a rotating pigeon wing and found the same curve shapes with a maximum C_L of 1.64 at 45 degrees and maximum C_D of 3.0 at 90 degrees[Ush09].

Figure 5.11 shows the obtained lift and drag coefficient curves from several insect and bird wing studies. In all cases, the form is approximated by $C_L = A\sin(2\alpha)$and $C_D = B(1-\cos(2\alpha))$ where A is the maximum coefficient of lift and $2B$ is the maximum coefficient of drag. We will use Ellington's value of 1.64 for the maximum coefficient of lift (Equation 5.8) because it is one of the few studies to accurately determine the maximum lift coefficient of a real feathered bird wing ($A = 1.64$)[Ush09]. Finally, we will use the value of 3.0 ($B = 1.5$) for the maximum drag coefficient (Equation 5.9). This value is supported by several studies[Ush09, DG93, UE02].

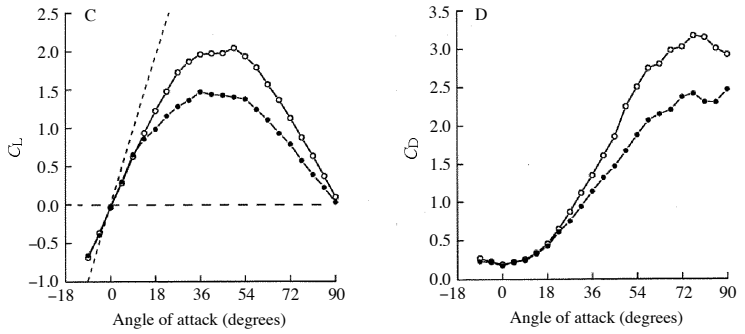

(a) Low Reynold's number flat plate experimental results[DG93]

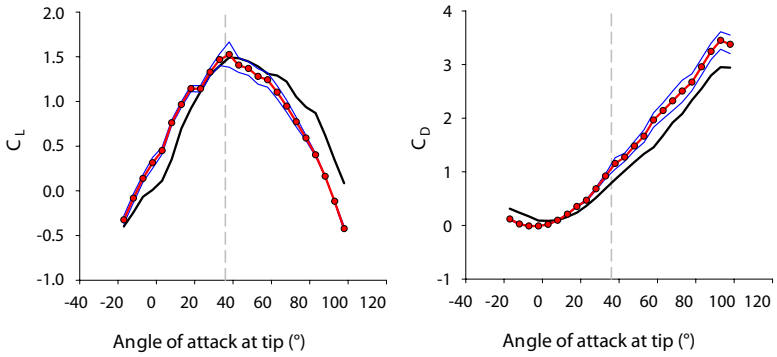

(b) Results obtained from a revolving pigeon wing[Ush09]

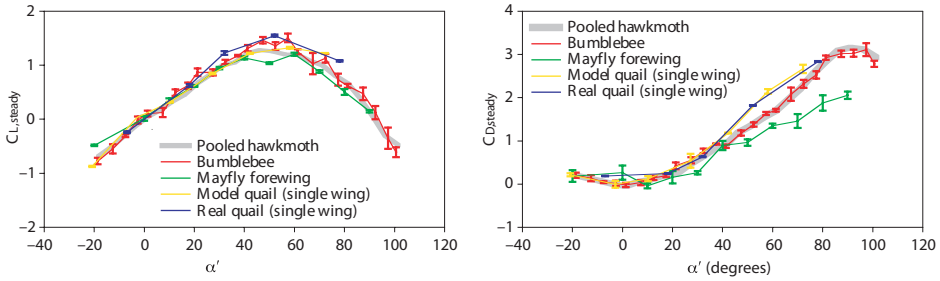

(c) Coefficient results of several insect species and one bird species[UE02]

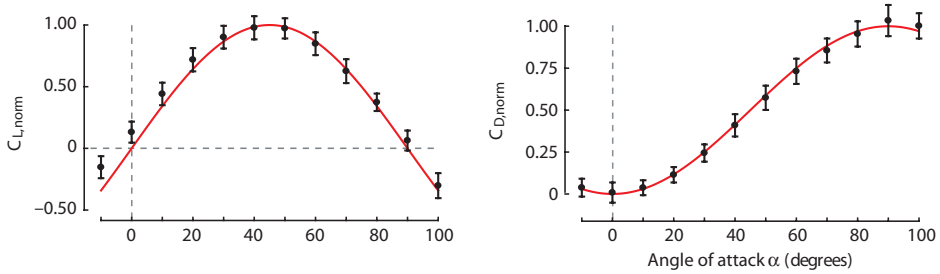

(d) Normalized coefficient results of a fruit fly wing[DD04]

Figure 5.11: C_L and C_D curves from a number of insect and bird wing studies over the complete range of angles of attack

$$C_L = 1.64 \sin 2\alpha \tag{5.8}$$

$$C_D = 1.5\,(1 - \cos 2\alpha) \tag{5.9}$$

Incorporating these coefficient functions into the equations for lift and drag (Equations 5.1 and 5.2), we obtain the final form of the two-dimensional lift and drag forces on an element in Equations 5.28 and 5.29.

$$\mathbf{F}'_L = \frac{1.64}{2}\rho\|\mathbf{U}\|^2 \sin(2\alpha)\, c\, \hat{\mathbf{y}}_v \tag{5.10}$$

$$\mathbf{F}'_D = -\frac{1.5}{2}\rho\|\mathbf{U}\|^2 (1 - \cos(2\alpha))\, c\, \hat{\mathbf{x}}_v \tag{5.11}$$

5.4 Revising the Blade Element Model

The major shortcoming of the blade element model is its lack of transient force terms. The angle-of-attack-dependent coefficients of lift and drag do little to capture the dynamic forces which arise as the wing undergoes rapid accelerations, decelerations, twists, and changes in direction. In order to add some of these forces to the blade element model, we incorporate two additional force terms into the model. The first is an added mass terms which is dependent on the acceleration of the wing elements. The second is a circulation term, which is dependent on the angular velocity of the wing. This implementation is borrowed from studies of fruit fly flight, where these terms are vitally important. While their relative magnitudes may be somewhat less when applied to bird flight, they remain important force terms for maintaining a physically accurate model.

5.4.1 Added Mass

Also referred to as virtual mass, added mass refers to the mass of fluid surrounding the wing that gets accelerated along with the wing as the wing moves. This fluid moving with the wing adds inertial forces which can be accounted for. Force due to added mass is an unsteady term which depends on the acceleration of the wing. A wing moving at constant velocity incurs no added mass. For high Reynold's number wings the added mass is very small and can be neglected. Added mass only becomes significant in low Reynold's number flight and in applications where the density of the wing is close to the density of the fluid.

For bird flight, the importance of added mass lies somewhere in between, and its effects are non-negligible. We follow the approach of Sane and Dickinson [SD01] and Berman and Wang[APW05, BW07], both of which sought to improve the quasi-steady model of flight as applied to fruit fly hovering. Following the classical derivation for the force due to added mass $\mathbf{F}_A$ around a theoretical flat plate, and projecting the added mass tensor into two dimensions yields equations 5.12 to 5.15 [Sed65]:

$$\begin{aligned} \mathbf{F'}_A &= \left(m_{22}\omega_{BE}\|\mathbf{U}\|sin\alpha - m_{11}\|\dot{\mathbf{U}}\|cos\alpha\right)\hat{\mathbf{x}}_{BE} \\ &\quad - \left(m_{11}\omega_{BE}\|\mathbf{U}\|cos\alpha + m_{22}\|\dot{\mathbf{U}}\|sin\alpha\right)\hat{\mathbf{y}}_{BE} \end{aligned} \tag{5.12}$$

Equation 5.12 gives the terms which comprise the two-dimensional added mass force $\mathbf{F'}_A$ for a wing of arbitrary shape. Each of the $\hat{\mathbf{x}}_{BE}$ and $\hat{\mathbf{y}}_{BE}$ components have both a linear acceleration and angular velocity term.

$$m_{11} = \frac{1}{4}\pi\rho c^2 \tag{5.13}$$

$$m_{22} = 0 \tag{5.14}$$

The coefficients m_{11} and m_{22} are terms from the added mass tensor which depend on the geometry of the wing. For a two dimensional flat plate with zero thickness, the equations for m_{11} is defined by Equation 5.13 where ρ is the density of air and c is the chord length of the element. In Equation 5.14, m_{22} becomes zero because we have simplified the geometry to have no thickness in the $\hat{\mathbf{y}}_{BE}$ direction. This simplification allows us to cancel two of the terms in equation 5.12 and yields a simpler formula.

$$\mathbf{F}'_A = -\frac{1}{4}\pi\rho c^2\|\dot{\mathbf{U}}\|\cos\alpha\,\hat{\mathbf{x}}_{BE} - \frac{1}{4}\pi\rho c^2\omega_{BE}\|\mathbf{U}\|\cos\alpha\,\hat{\mathbf{y}}_{BE} \tag{5.15}$$

5.4.2 Angular Rotation

In addition to added mass, another transient term exists which accounts for lift due to the rotational velocity of an element as distinct from the already calculated lift due to translation (Equation 5.28). Sane and Dickinson [SD02] as well as Berman and Wang[APW05, BW07] obtained similar results to each other in applying this terms to the net force in their fruit fly hovering models. Sane and Dickinson took the approach of adding a separate coefficient-based force due to circulation term to the net force, while Berman and Wang included an angular rotation-based term in the general lift equation. Berman and Wang based their model on the earlier Andersen et al. study [APW05] which fit a solution of ordinary differential equations to the results computed through thorough experimentation and CFD simulation. Andersen et al. found that this angular velocity term ω augmented the translational lift to fit the lift predicted by CFD on a thin and flat wing very well.

Sane and Dickinson's circulation term is described in Equations 5.16 to 5.20. Referring back to the equation for lift force due to circulation (Equation 2.6, Equa-

tion 5.16), Sane and Dickinson define the circulation Γ as depending on the rotational velocity of the element, chord length squared, and a coefficient of rotation (Equation 5.17). Given in Equation 5.18, this newly introduced coefficient of rotation C_{rot} depends on a non-dimensional axis of rotation $\hat{x}_0$ (not to be confused with a unit vector). This axis of rotation $\hat{x}_0$ goes from a value of 0.0 at the leading edge to 1.0 at the trailing edge.

$$F_R = \rho U \Gamma \tag{5.16}$$

$$\Gamma = C_{rot} \omega c^2 \tag{5.17}$$

$$C_{rot} = \pi \left(0.75 - \hat{x}_0\right) \tag{5.18}$$

However, the axis of rotation is difficult to define if it is not externally imposed by a motor, as Sane and Dickinson did. Sane and Dickinson state that $\hat{x}_0$ is thought to lie between 0.25 and 0.5 for insects. We will set the value of $\hat{x}_0$ to 0.25 because it agrees well with Berman and Wang's model below. Substituting this value into Equation 5.18, we find the coefficient of rotation to be a constant equal to $\frac{\pi}{2}$. We substitute this coefficient back into Equation 5.17 and exchange the generic ω for the more appropriate$\dot{\alpha}$ to obtain the circulation (Equation 5.19).

$$\Gamma = \frac{\pi}{2} \dot{\alpha} c^2 \tag{5.19}$$

Finally, we substitute Equation 5.19 into Equation 5.16 to obtain the final force due to circulation around a two-dimensional element in Equation 5.20.

$$\mathbf{F}'_R = \frac{1}{2} \rho \pi \|\mathbf{U}\| \dot{\alpha} c^2 \, \hat{\mathbf{y}}_v \tag{5.20}$$

Andersen et al. obtained the same result by creating an analytic model to approximate the results from highly accurate CFD simulations and physical experiments. The lift force for this model is given in Equation 5.21.

$$\mathbf{F}'_{lift} = -\frac{1}{2}\rho C_T c\|\mathbf{U}\|^2 \sin(2\alpha)\ \hat{\mathbf{y}}_v + \frac{1}{2}\rho C_R\|\mathbf{U}\|\dot{\alpha}c^2\,\hat{\mathbf{y}}_v \quad (5.21)$$

$$\mathbf{F}'_R = \frac{1}{2}\rho C_R\|\mathbf{U}\|\dot{\alpha}c^2\,\hat{\mathbf{y}}_v \quad (5.22)$$

Isolating the angular velocity dependent term from the blade element translational lift term, we obtain Equation 5.22. Berman and Wang set the value of the coefficient of rotation C_R, introduced in this model, to π. This substitution yields Equation 5.23, the same force due to angular rotation as found by Sane and Dickinson.

$$\mathbf{F}'_R = \frac{1}{2}\rho\pi\|\mathbf{U}\|\dot{\alpha}c^2\,\hat{\mathbf{y}}_v \quad (5.23)$$

5.5 Three-Dimensional Forces

In the previous sections, we have been looking at the two-dimensional forces on an element denoted by the prime designation. In order to extend these forces into the third dimension, we must multiply them by the span width l of the element. Equations 5.24 through 5.27 list these forces.

$$\mathbf{F}_L = \frac{1.64}{2}\rho\|\mathbf{U}\|^2 \sin(2\alpha)\, c\, l\,\hat{\mathbf{y}}_v \quad (5.24)$$

$$\mathbf{F}_D = -\frac{1.5}{2}\rho\|\mathbf{U}\|^2 (1-\cos(2\alpha))\, c\, l\,\hat{\mathbf{x}}_v \quad (5.25)$$

$$\mathbf{F}_A = -\frac{1}{4}\pi\rho c^2 l\left(\|\dot{\mathbf{U}}\|\cos\alpha\,\hat{\mathbf{x}}_{BE} - \omega_{BE}\|\mathbf{U}\|\cos\alpha\,\hat{\mathbf{y}}_{BE}\right) \quad (5.26)$$

$$\mathbf{F}_R = \frac{1}{2}\rho\pi\|\mathbf{U}\|\dot{\alpha}c^2 l\,\hat{\mathbf{y}}_v \quad (5.27)$$

The arbitrary orientation of our polygonal flat plates makes defining a chord and span length difficult. Instead, we make the assumption that each flat plate is square, thus the chord and span are both equal. Therefore, we can define both of

them as a function of the polygonal surface area, a known quantity. In Equations 5.28through 5.31, we make the substitutions $c \equiv \sqrt{A}$ and $l \equiv \sqrt{A}$ where A is the area of the polygonal element.

$$\mathbf{F}_L = \frac{1.64}{2}\rho\|\mathbf{U}\|^2 \sin(2\alpha)\, A\, \hat{\mathbf{y}}_v \tag{5.28}$$

$$\mathbf{F}_D = -\frac{1.5}{2}\rho\|\mathbf{U}\|^2 (1 - \cos(2\alpha))\, A\, \hat{\mathbf{x}}_v \tag{5.29}$$

$$\mathbf{F}_A = -\frac{1}{4}\pi\rho A^{\frac{3}{2}} \left(\|\dot{\mathbf{U}}\| \cos\alpha\, \hat{\mathbf{x}}_{BE} - \omega_{BE}\|\mathbf{U}\| \cos\alpha\, \hat{\mathbf{y}}_{BE}\right) \tag{5.30}$$

$$\mathbf{F}_R = \frac{1}{2}\pi\rho\|\mathbf{U}\|\dot{\alpha} A^{\frac{3}{2}}\, \hat{\mathbf{y}}_v \tag{5.31}$$

5.6 Integration

We now have the pieces in place to compute the external fluid forces on every individual polygonal element in the wing to obtain an net instantaneous force on the bird. We can integrate this instantaneous force over the time range of the complete wingbeat to find the net impulse on the bird, $\mathbf{I}_{BE}$. Impulse is simply a force multiplied by the time period over which it acts, and has units of momentum. With this predicted impulse integrated from the aerodynamic forces, we can compare it to the actual impulse required to keep the bird aloft $\mathbf{I}^*$. The actual impulse is calculated as the weight of the bird m_b multiplied by gravitational acceleration g, and the wingbeat period T. This impulse is given as a scalar in Equation 5.32.

$$I^* = m_b g T \tag{5.32}$$

We then can then define a lift ratio parameter r_{lift} (Equation 5.33) which is the ratio of the theoretical impulse to the real impulse in the vertical direction. In this equation, we double the theoretical impulse of a single wing to account for the pair of wings. If the predicted lift and drag forces are accurate, the lift ratio will

Table 5.2: Mathematical Term Definitions

Description	Notation	Definition
2-D instantaneous force on element	$\mathbf{F}'_i$	$\mathbf{F}'_i = [\mathbf{F}'_L + \mathbf{F}'_D + \mathbf{F}'_A + \mathbf{F}'_R]_i$
3-D instantaneous force on element	$\mathbf{F}_i$	$\mathbf{F}_i = \mathbf{F}'_i \times$ span of element
Total instantaneous force on wing: Force summed over all elements	$\mathbf{F}$	$\mathbf{F} = \sum_{wing} \mathbf{F}_i$
Total force on wing summed over time: Impulse	$\mathbf{I}$	$\mathbf{I} = \sum_{T} \mathbf{F}\, \Delta t$

be equal to one. A value of greater than one would indicate that the aerodynamic force model is overestimating forces, and a value less than one would indicate an underestimation of forces.

$$r_{\text{lift}} = \frac{2I_{\text{BE,vertical}}}{I^*} \tag{5.33}$$

Table 5.2 describes the terms used as we integrate to find the impulse. We start with $\mathbf{F}'_i$, the two-dimensional force on an element. The index i denotes the specific element, and i ranges from 0 to n where n is the total number of faces making up the wing. When $\mathbf{F}'_i$ is converted to force on a three-dimensional element, it becomes $\mathbf{F}_i$ and is equal to the sum of the lift, drag, added mass, and circulation forces on the element ($\mathbf{F}_i = \mathbf{F}_{L,i} + \mathbf{F}_{D,i} + \mathbf{F}_{A,i} + \mathbf{F}_{R,i}$). Summing this force for every element gives the total instantaneous force on the wing $\mathbf{F}$. The last piece of the integration is to sum the instantaneous forces on the wing throughout the entire wingbeat period T (Equation 5.34).

$$\mathbf{I} = \sum_{T} \left[\left[\sum_{wing} \mathbf{F}_i \right]_t \Delta t \right] \tag{5.34}$$

We now have a fully-defined quasi-steady state which acts on individual polygonal elements, accounts for transient forces, and integrates to a single numerical

value (impulse in the vertical direction) with which we can evaluate the accuracy of our model.

CHAPTER 6

RESULTS

In this chapter we apply the aerodynamic model developed in Chapter 5 to the geometric and kinematic model described in Chapter 4, and present the resulting forces on a bird throughout a wingbeat. We begin by outlining the timing of the wingbeat and dimensions of the wing. We compute several non-dimensional parameters, including the Reynolds number and Strouhal number. Importantly, we also estimate the mass of the bird for use in our force equations.

We then look at the forces on the simple mesh created directly from Holt's motion capture data. We look at each of the four force terms; lift, drag, added mass, and circulation, and compare the effects of each. We then determine the efficiency of this model as applied to the simple mesh, before moving on the higher-resolution feathered mesh. We perform the same computations on the feathered mesh, and investigate the differences between the two. Finally, we look at the effects of feather bending and twist on force production of the feathered model.

6.1 Biological Benchmarks

Our Red-winged blackbird test subject was an adult female. During the recorded wingbeat in the flight tunnel, the bird flew at 4.36 meters per second. The observed wingbeat had a period of duration of 83 milliseconds, yielding a flapping frequency of 12.0 hertz. Although we could not measure the dimensions of the wings directly from the specimen, we can estimate these parameters from the motion capture data. Our specimen had a wingspan of approximately 35 centimeters from wingtip to wingtip, including the body. A single wing measured 16 centimeters from shoulder to wingtip (the distal tip of the ninth primary feather). We estimate the average chord length $\bar{c}$ to be 6 centimeters. The surface planform area

of the extended wing is about 80 cm^2. We can use these physiological dimensions to calculate non-dimensional characteristic parameters.

The Reynolds number ($Re = \frac{\rho U l}{\mu}$) comes to $Re = 1.85 \times 10^5$ when we set the characteristic length l to the average chord length $\bar{c}$ and use standard values for density and viscosity[1]. This is within the expect range of Reynolds numbers for bird flight.

The Strouhal number, a dimensionless parameter which is a ratio of the vertical motion of the wing to its horizontal translation, is the wingbeat frequency multiplied by vertical amplitude and divided by the forward velocity of the bird: $St = \frac{f\,a}{U}$. Studies have shown that animals which propel themselves through fluid, including fish, sharks, dolphins, insects, bats, and birds, all move most efficiently at Strouhal numbers between 0.2 and 0.4 [TNT03, NTT04]. Our Red-winged blackbird's wing bends nearly ninety degrees upward from the horizontal plane, giving a rough flapping amplitude of 13 centimeters. This gives a Strouhal number of $St = 0.36$. Although a flight tunnel is not a natural flying environment, we can conclude that the bird was flying efficiently during the captured wingbeat.

Lastly, we can look at the reduced frequency parameter ($k = \frac{\pi f\,\bar{c}}{U}$) to characterize the oscillatory motion of the wing. Reduced frequency parameters below 0.1 indicate that unsteady aerodynamic effects play no role, while values above 1.0 indicate unsteady effects to be important [Spe03]. Our bird flew with a reduced frequency of $k = 0.52$, indicating that unsteady effects may not be large in magnitude but cannot be ignored either.

To determine the mass of the bird, we have to estimate from cataloged specimens. We were unable to measure the mass of our test specimen in the field due to handling constraints. However, since our specimen was an adult female Red-

[1]Assuming standard temperature (20°c) and pressure (101kPa) values for the properties of air: $\rho = 1.225\text{kg m}^{-2}$ $\mu = 1.53 \times 10^{-5}\text{kg m}^{-1}\text{ s}^{-1}$.

winged blackbird, and mass estimates are readily available. The *CRC Handbook of Avian Masses* lists the average mass of a female Red-winged blackbird as 42.72 grams with a standard deviation of 2.51 grams[Jr.07]. Using this reference, we will assume the mass of our bird to have been 43 grams.

6.2 Coarse Motion Captured Mesh

Our preliminary analysis begins with the coarse motion capture mesh. Figures 6.1 and 6.2 show this coarse mesh as a series of snapshots from four different camera views; the three main axes as well as a perspective view. A force analysis of these low-resolution polygons is indicative of the forces on the higher resolution model, treated later in this chapter. Figure 6.3 shows the area of each face throughout the wingbeat with an inset giving a reference of polygon location. The downstroke period of time is shaded gray, and the upstroke is white. Looking at the data, we can see that Face 0, which represents the humerus, elbow, and forearm; undergoes the most deformation of the faces. Face 2 is most contracted at 50 milliseconds, the threshold between the downstroke and upstroke. The other faces are most contracted in the middle of the upstroke, around 70 milliseconds. This is corresponds to the flexion of the wrist, just before it begins to extend in preparation for the next downstroke.

Figure 6.4 gives the angle of attack per face. Again, Face 0, representing the shoulder and elbow joints, reaches its minima earlier than the other polygons. The angle of attack is positive for the entire downstroke, with an mean of around 45 degrees, and a maximum of 80 degrees. In the latter part of the upstroke, the angle of attack becomes positive again as well.

Figure 6.5 plots the average angle of attack and average velocity. Of note is the double peak in velocity during the downstroke, and the single sharp minima

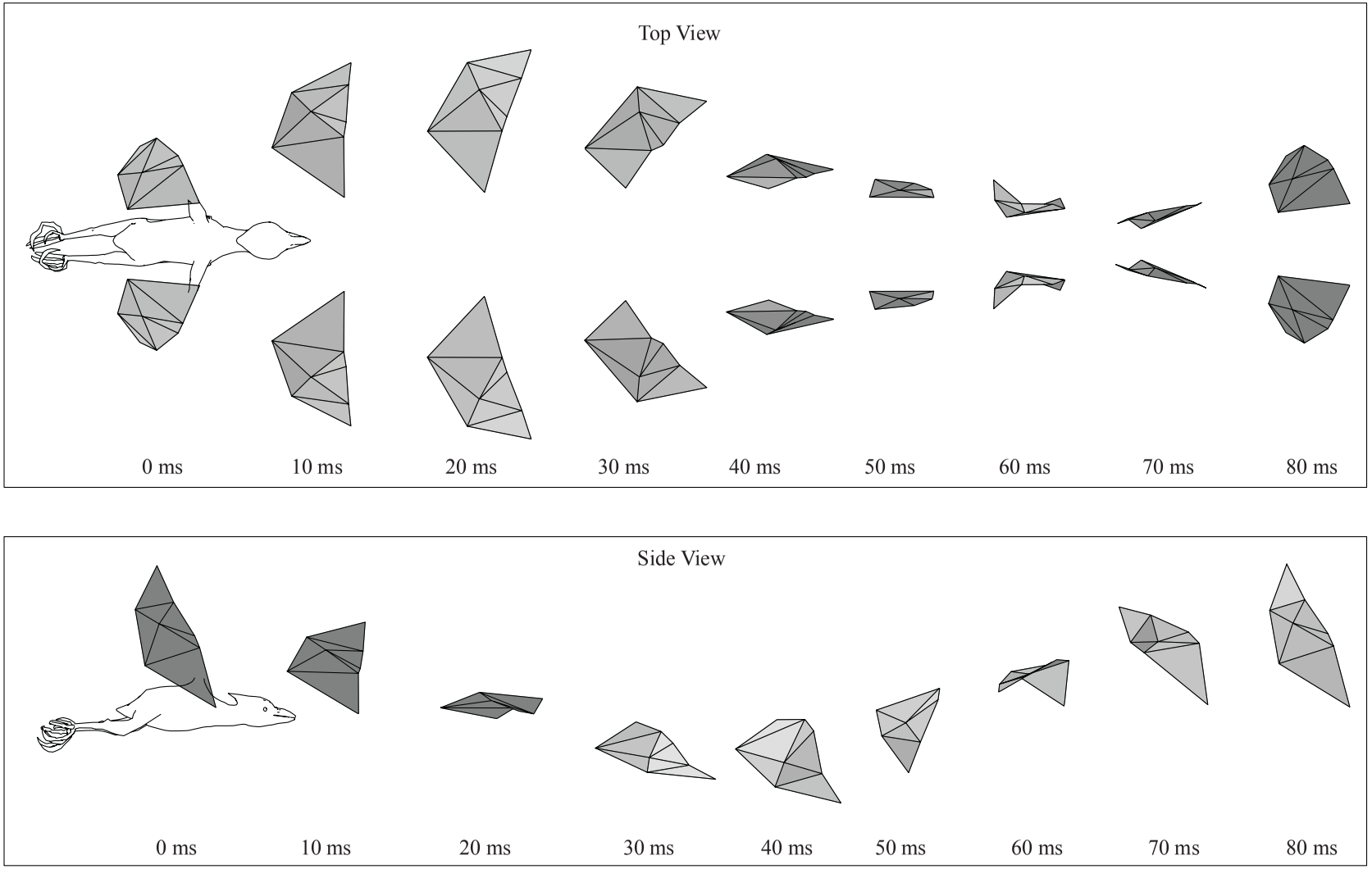

Figure 6.1: Top and side views of coarse mesh wingbeat

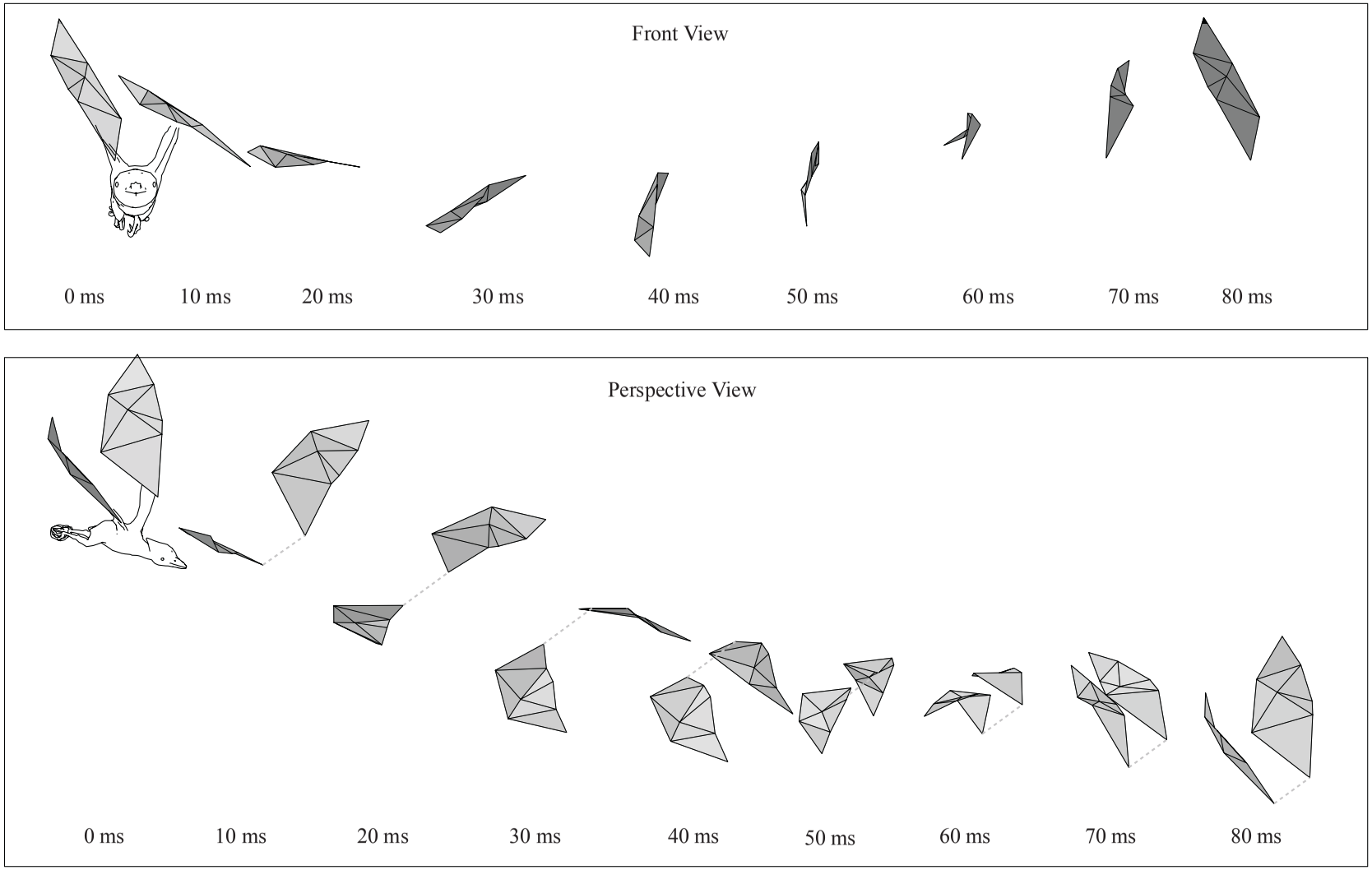

Figure 6.2: Front and perspective views of coarse mesh wingbeat

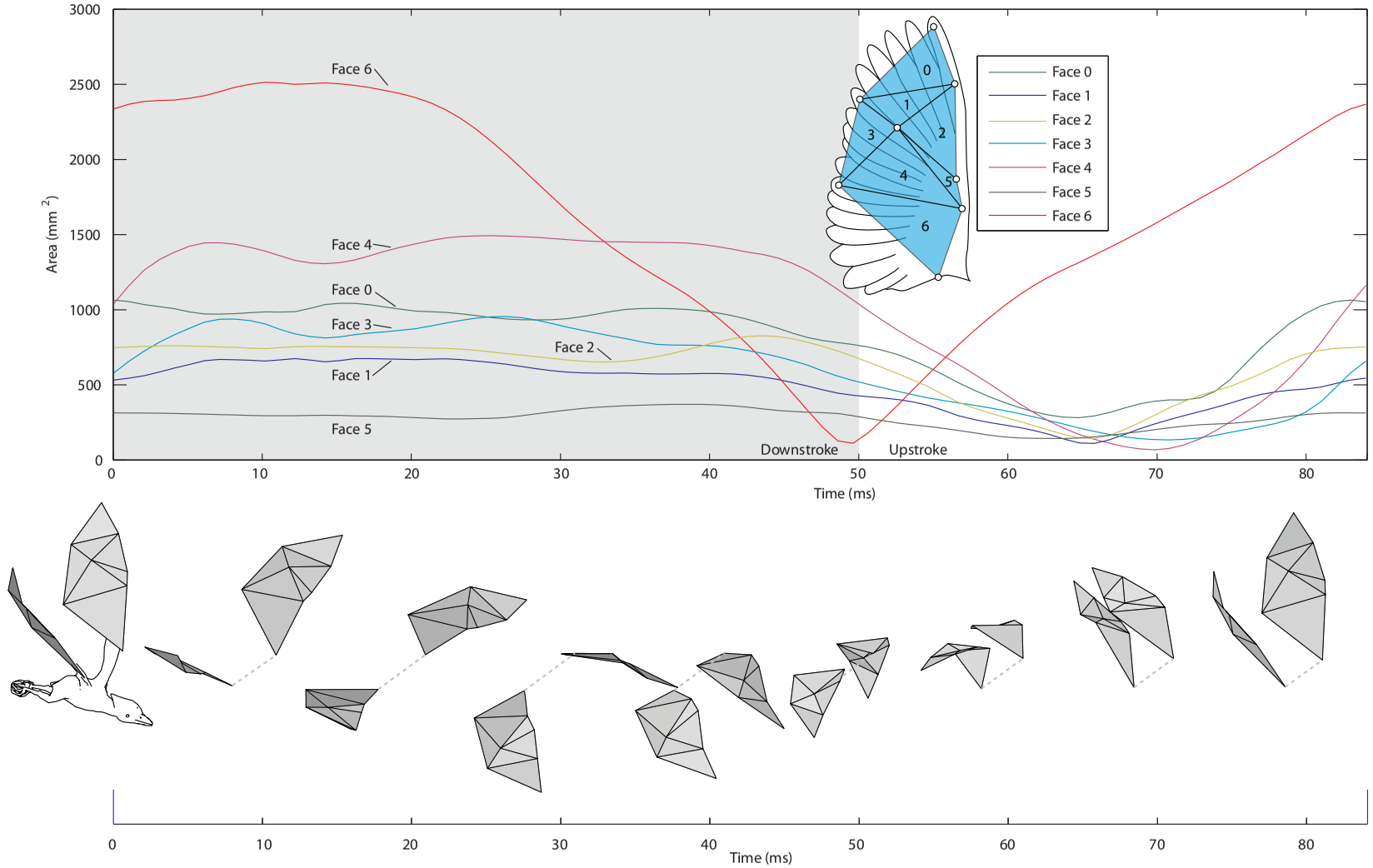

Figure 6.3: Instantaneous area per face of the coarse mesh

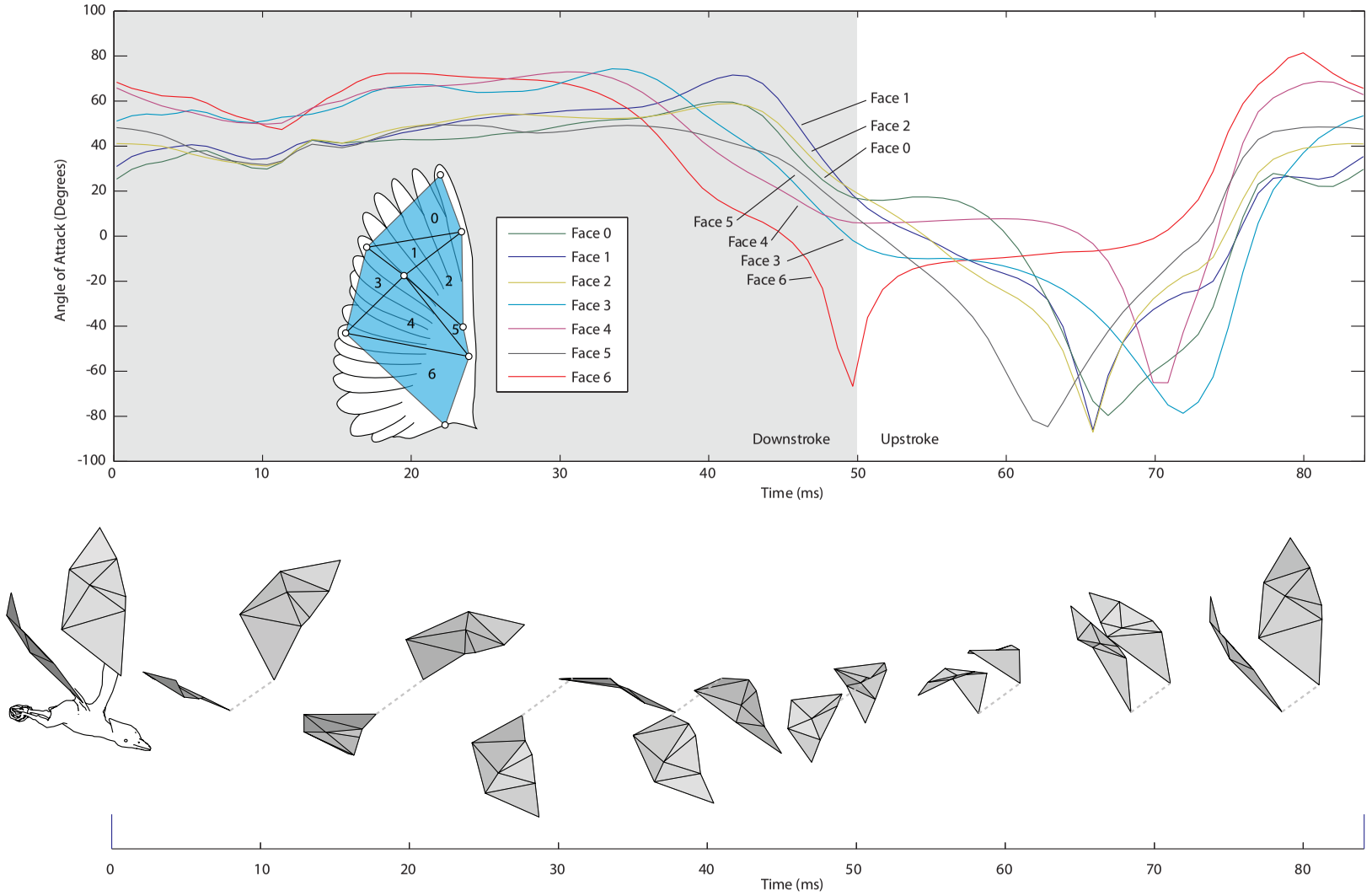

Figure 6.4: Instantaneous angle of attack per face of the coarse mesh

during the upstroke. Angle of attack increases during the downstroke until it peaks at the end of the downstroke, and then sharply minimizes on the upstroke. It is difficult to conclude anything more from this plot because the directions in which the forces act are constantly shifting. Thus a high velocity on the downstroke is not necessarily inefficient, because the faces are likely oriented in a way minimize the net downward force. The force computations take the changing coordinate systems into account, and apply each of the force terms in the proper direction. Each of the four force terms; lift, drag, added mass, and circulation, acts in some combination of face normal, back, and relative up unit vectors (refer to Figure 5.8 and Table 5.1 for definitions of these unit vectors) .

Figure 6.22 shows the vertical component of each of the four force terms. We can see that translational lift contributes the most force, followed by drag, which is also translational. Although drag is often thought of as a hindering force, here it is advantageous due to the orientation of the polygons. The added mass and rotational lift terms contribute a smaller amount, but are not negligible. The translational lift and drag terms show a distinct peak in the latter portion of the downstroke, and all of the force terms are minimized on the upstroke. The added mass and rotational lift terms are more difficult to correlate with the motion of the bird, but their oscillatory nature in the early part of the downstroke reinforce the high-frequency bumps in the translational lift curve.

Summing these force terms together, we obtain the total force shown in figure 6.7. Each directional component of the total force is plotted, with the vertical force indicated in bold. Here the triple-peaked nature of the vertical force is evident. As shown above, the unsteady added mass and circulation terms reinforce this trend. Integrating through the wingbeat, we can see that while the vertical force integrates to a net positive force, the side and forward forces have negative values

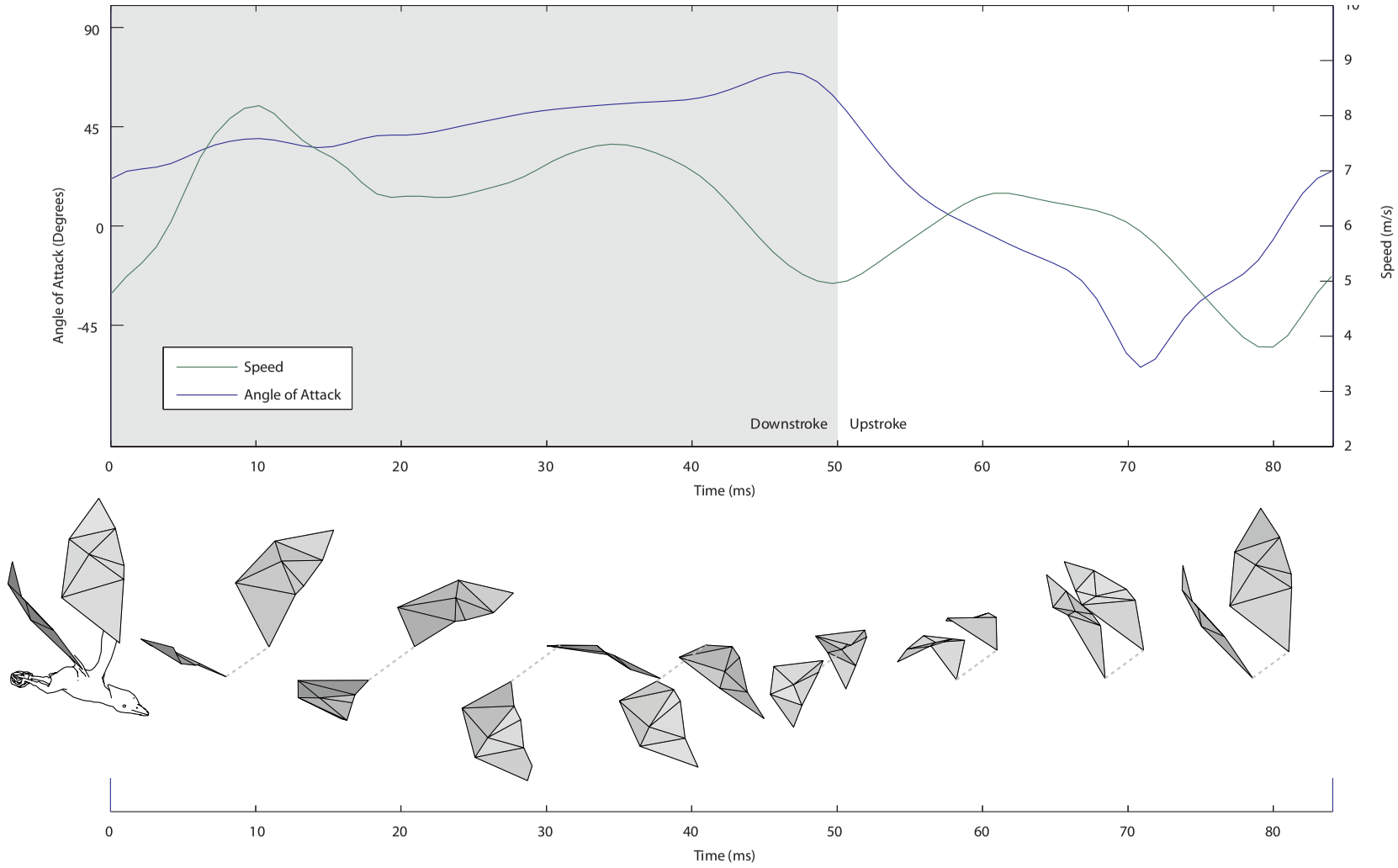

Figure 6.5: Average angle of attack and velocity of the coarse mesh

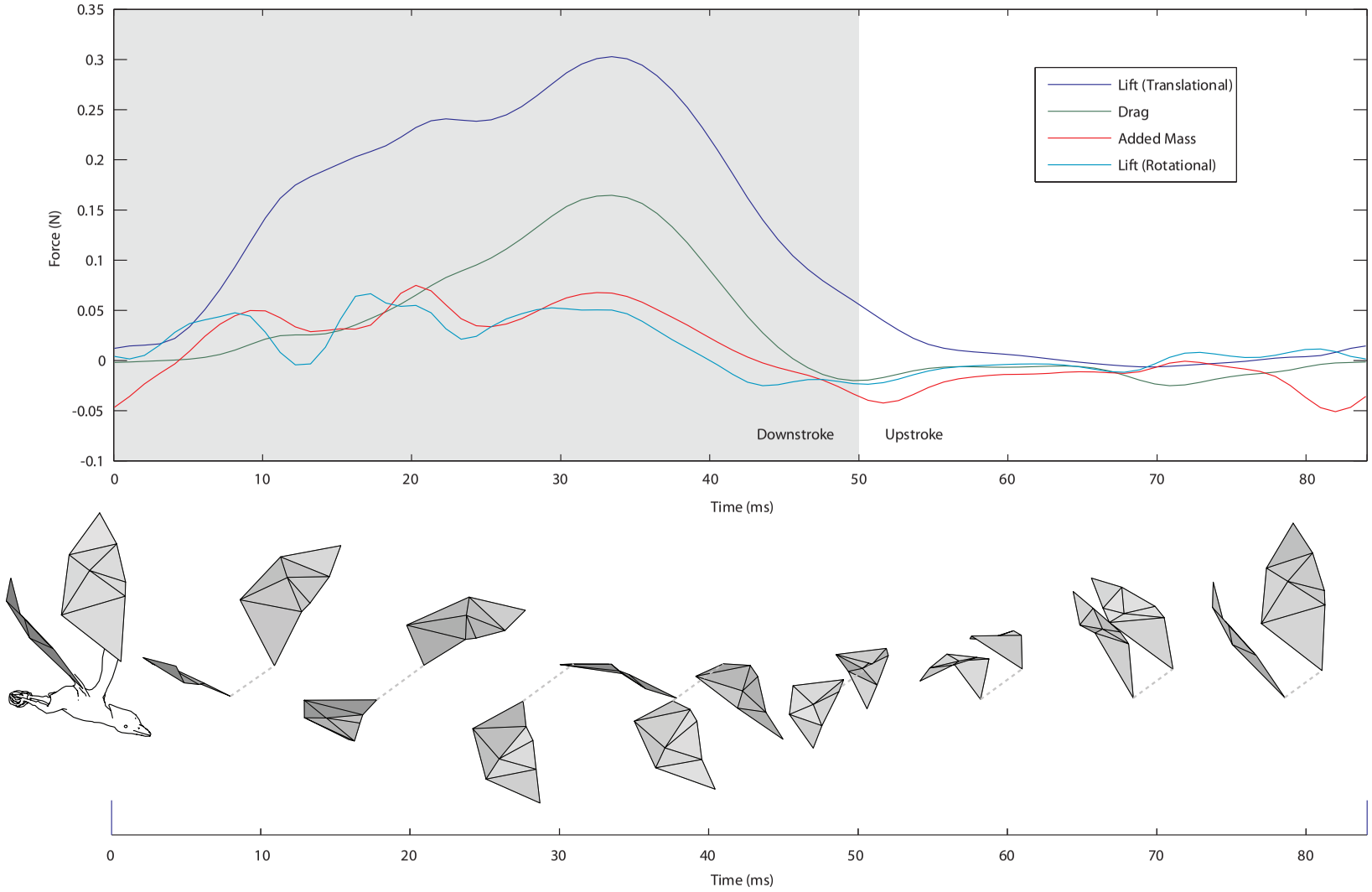

Figure 6.6: Components of instantaneous force in the vertical dimension of the coarse mesh

which serve to cancel out their effect. Theoretically, a bird in straight and level flight has only to over come the force of gravity. If it is neither accelerating nor decelerating, the side and forward forces should integrate to zero. However, our model does not take into account the additional drag on the bird due to the body and tail. Thus, the forward force is likely underestimated.

Note that in all of these plots, we are investigating only the single wing. To obtain the full force on the bird, we must double the force to account for the second wing. The second wing also negates the effects of force in the side (mediolateral) direction. However, some of this air which is forced together by the wings likely results in a forward propulsive effect, and may account for the low values of force in the forward direction.

Looking to see the contribution to total vertical force of each of the four force terms, we plot their percentages in Figure 6.8. We can see that translational lift and drag together account for almost ninety percent of the total force, with the unsteady terms contributing just over ten percent. Circulation contributes slightly more than added mass.

Having estimated the mass of the bird in Section 6.1, we can now compute the required impulse I^* (Equation 5.32). Using a mass for the bird of forty-three grams, we compute the required impulse for the wingbeat to be $I^* = 0.0356\,\mathrm{N}\cdot\mathrm{s}$. Dividing by the time period, we can compute the instantaneous required force to overcome gravity, $F^*_{wing} = \frac{1}{2} m_b g = 0.215\,\mathrm{N}$. The one-half coefficient accounts for the single wing supporting half of the weight of the bird. Plotting this required force value against the computed total vertical force gives us Figure 6.9. Here, the dotted line indicates the required force, and the solid line represents the computed force from our model. To support the weight of the bird, the area under each curve should match.

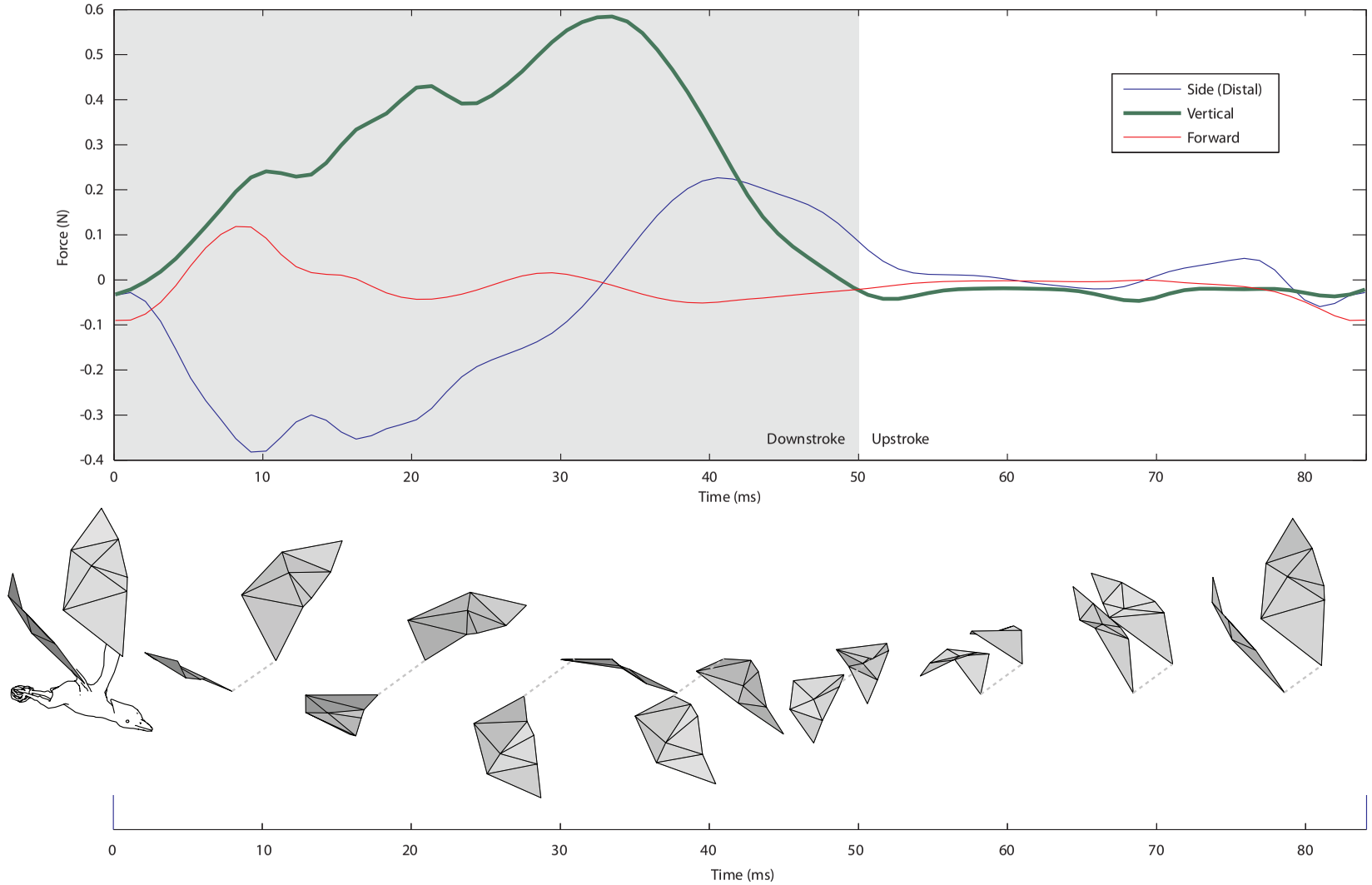

Figure 6.7: Total instantaneous force in three dimensions of the coarse mesh

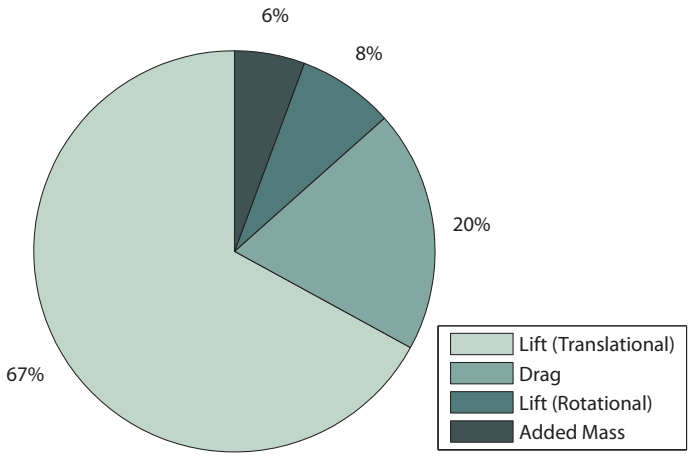

Figure 6.8: Percent contributions of force components of coarse mesh

Table 6.1: Integrated impulse and average force values in three dimensions for one and both wings of the coarse mesh

Term	Direction	Single Wing	Both Wings
Impulse I	**Vertical**	$I_y = \quad 1.36 \times 10^{-2}\text{N} \cdot \text{s}$	$I_{y,bird} = 2.73 \times 10^{-2}\text{N} \cdot \text{s}$
	Forward	$I_x = \quad 8.42 \times 10^{-4}\text{N} \cdot \text{s}$	$I_{x,bird} = 1.68 \times 10^{-3}\text{N} \cdot \text{s}$
	Side	$I_z = -4.78 \times 10^{-3}\text{N} \cdot \text{s}$	$I_{z,bird} = 0.00 \times 10^{-3}\text{N} \cdot \text{s}$
Average Force $\bar{F}$	**Vertical**	$\bar{F}_y = \quad 1.64 \times 10^{-1}\text{N}$	$\bar{F}_{y,bird} = 3.28 \times 10^{-1}\text{N}$
	Forward	$\bar{F}_x = \quad 1.01 \times 10^{-2}\text{N}$	$\bar{F}_{x,bird} = 2.02 \times 10^{-2}\text{N}$
	Side	$\bar{F}_z = -5.76 \times 10^{-2}\text{N}$	$\bar{F}_{z,bird} = 0.00 \times 10^{-2}\text{N}$

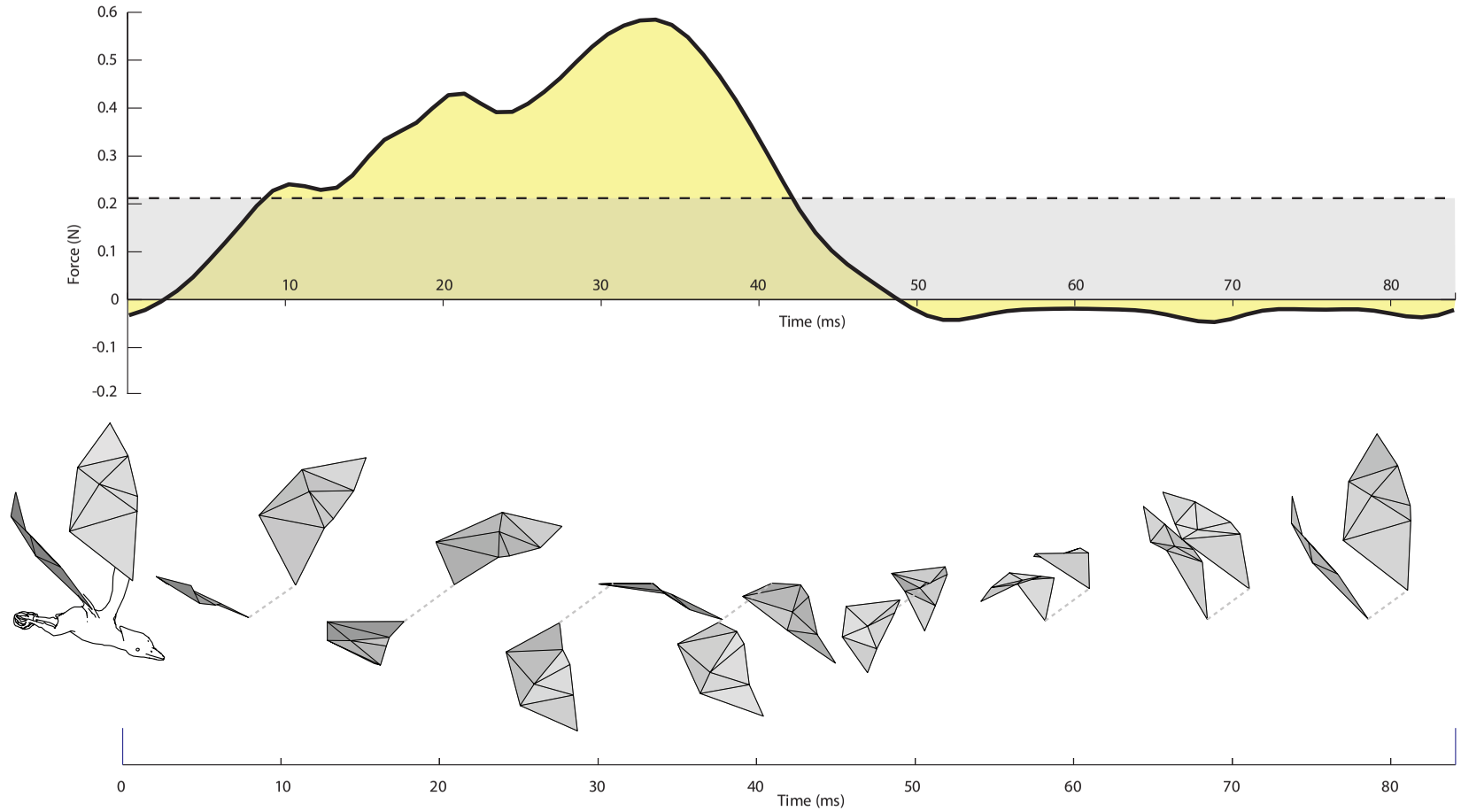

Figure 6.9: Total vertical aerodynamic force of the coarse mesh and gravitational force. The weight of the bird (F^*_{wing}) is shown as the dotted line.

Integrating the total aerodynamic force gives the values listed in Table 6.1. Dividing the impulse by the time period gives the average force, $\bar{F}$. We can now compute the lift ratio r_{lift} (Equation 5.33) and determine how well the modeled force values match the actual force needed to overcome gravity and keep the bird in the air. Setting the lift ratio equal to $r_{\text{lift}} = \frac{I_{\text{y,bird}}}{I^*}$, and using the value of $I_{y,bird} = 2.73 \times 10^{-2}$ for the computed vertical impulse and a value of $I^* = 0.0356$ for the actual required impulse, we obtain a lift ratio value of $r_{\text{lift}} = 76\%$ (Equation 6.3).

$$r_{\text{lift}} = \frac{I_{\text{y,bird}}}{I^*} = 0.760 \tag{6.1}$$

Our force model predicts seventy-five percent of the force required to overcome gravity from the wings. Additional force arising from the body and tail is not considered. According to a recent study by Usherwood et. al, the tail can contribute more than eight percent of a bird's weight in lift[UHMB05]. Such a force addition from the tail would leave only sixteen percent of the bird's weight unaccounted for by aerodynamic forces. Given the amount of simplification in this model, even an inconsistency of sixteen percent is an encouraging result.

Next, we will look at the wing with full feather geometry. We will describe how we animated the wing, and investigate the differences in force and impulse production between the above coarse mesh and the finely-resolved full feather mesh. Finally, we will look at the effects of feather bend and twist on the total force production.

6.3 Kinematics and Animation of Fine Feather Meshes

We use character animation techniques to define the pose of the wing for each timestep. By setting keyframes for the rotations of each joint, the hierarchy of

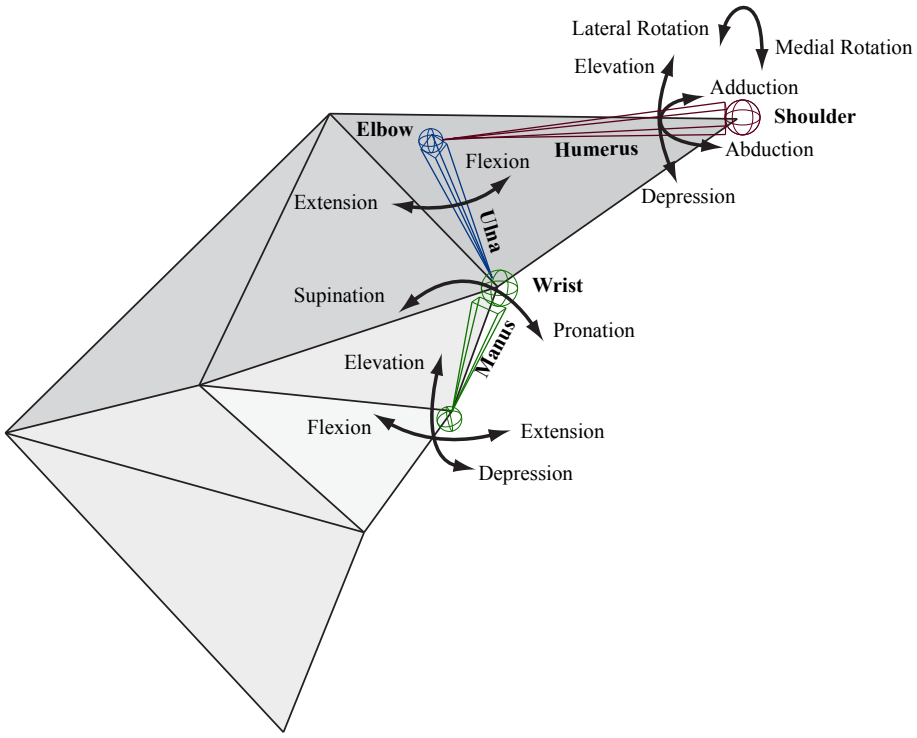

Figure 6.10: Nomenclature of the rotational degrees of freedom of arm joints

the model and the scripted constraints determine the position and rotation of each feather. We use a combination of forward kinematics (FK) and inverse kinematics (IK) to specify joint rotations. Figure 6.10 illustrates the seven degrees of freedom of the bird arm, which are similar to the human arm. The should and wrist are both ball joints, and have three degrees of freedom. The elbow, conversely, is a hinge joint and has a single degree of freedom.

The rotations of the shoulder and elbow are determined using an IK solver, which seeks to minimize those rotations in order to colocate the wrist joint with the marker on the coarse mesh representing the wrist. The IK solver also seeks to keep the two joints in the plane created by the markers of the coarse mesh. Bone length affects the rotations of each joint, and therefore we use Holt's analysis of bone lengths for our model, given in Table 6.2. The wrist joint itself is controlled

Table 6.2: Estimated bone lengths from specimen and marker data [Hol09]

Bone	Length
Humerus	29mm
Ulna	45mm
Manus	15mm

by an FK solver which utilizes an aim constraint. This aim constraint points the wrist along the axis created by the the leading edge of the wing and again seeks to keep the rotations in the plane of the coarse mesh.

Figure 6.11 shows the animation curves of the rotations of the shoulder joint along with the joint positions superimposed over the perspective snapshot views. The main motion of the wingbeat is the vertical elevation-depression motion of the shoulder (long-dashed blue curve). This creates the framework of the flap, which is completed by the other rotational degrees of freedom.

Figure 6.12 shows the extension-flexion of the elbow joint. When the arms is fully outstretched, this angle is 180 degrees, and zero when the elbow is fully bent. Here we see that the elbow is almost fully extended at the beginning of the downstroke, and retracts to about forty degrees on the upstroke to help minimize surface area during this drag-inducing phase of the wingbeat.

Figure 6.13 shows the complex rotation of the wrist. Since all of the primary feathers are attached to the manus or hand-wing, the orientation of the wrist has the most direct impact on the motion of the feathers of any of the arm joints. Like the elbow, the wrist is nearly fully extended on the downstroke, and retracts in flexion to near zero degrees on the upstroke for aerodynamic efficiency. This is the most noticeable motion of the wrist, but the other two axes have important functions as well. The spike in depression at the end of the downstroke and just before the upstroke gives a flick of air inward, which may contribute to forward force as discussed earlier. The supination-pronation movement of the wrist serves

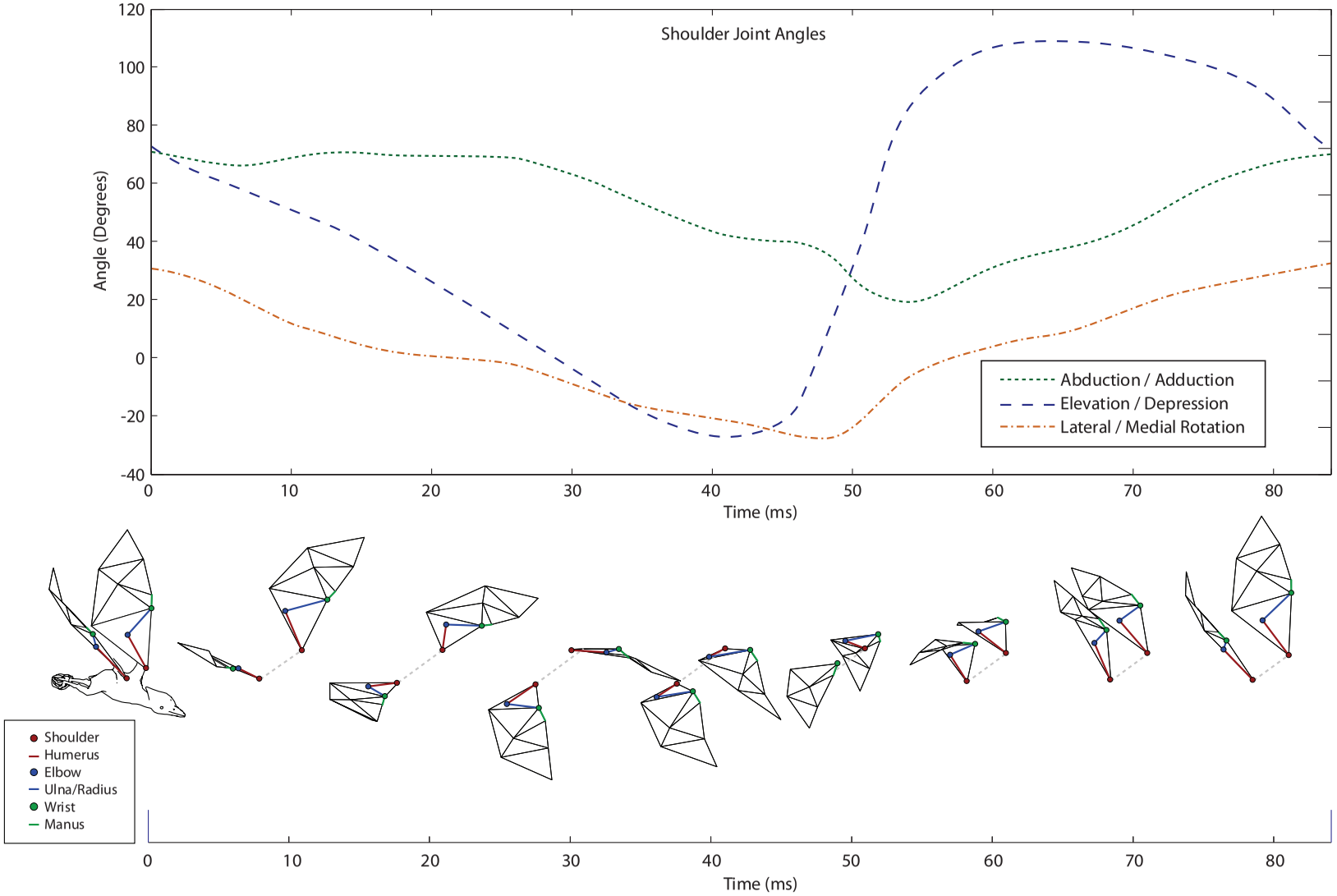

Figure 6.11: Shoulder rotation animation curves for the three rotational axes

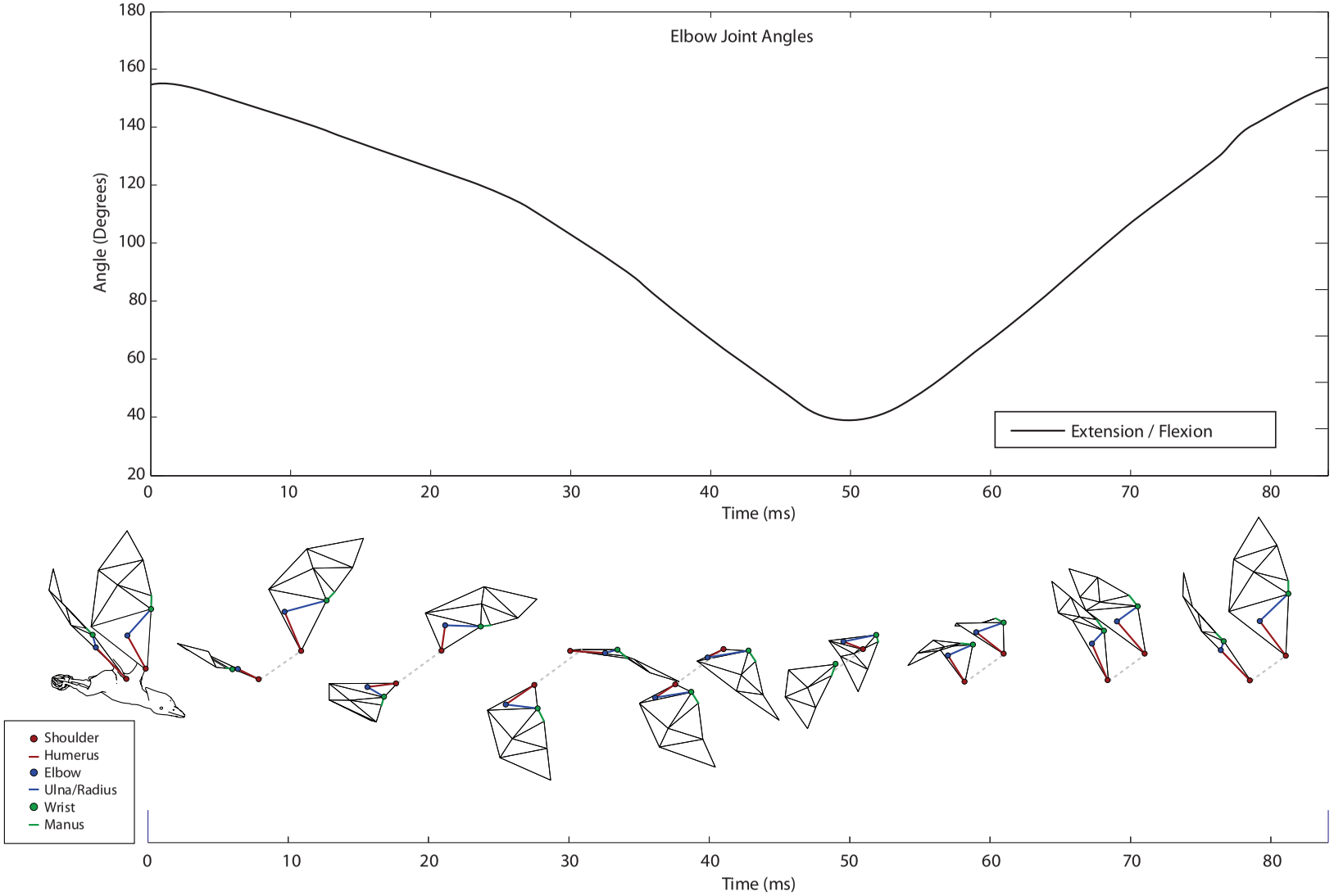

Figure 6.12: Elbow rotation animation curve with single degree of freedom

the important function of adjusting the overall angle of attack of the primary feathers. This angle is near neutral during the downstroke, but on the upstroke the wrist supinates sharply to minimize the angle of attack as the wing is now moving upward.

With our joint angles specified by the outlined constraints, we are finally able to animate the finely-resolved mesh of the wing including each of the eighteen feathers as well as the entire arm and patagium. Figure 6.14 shows how the fine mesh compares to the coarse mesh. The overlap is not perfect, but it fits the motion well given the degrees of freedom of the arms joints and the constraint of constant bone lengths. Figures 6.16 and 6.17 in Section 6.5 show the fine mesh from additional viewpoints.

6.4 Feather Occlusion

As we can see in Figure 6.14, many feathers overlap. Therefore, we cannot simply sum the forces on each polygonal element, because many forces would be counted twice. Therefore, we implement a crude algorithm to determine if a given face on a feather is occluded by another feather. Knowing the geometry of the neighboring feather, this algorithm simply determines whether the centerpoint of a face, projected orthogonally, is within the two-dimensional geometric bounds of the neighboring feather. If so, it is ignored and forces are not computed. If it lies outside the bounds of the overlapping feather, its forces are computed to be aggregated with the others to determine the net force. While still discreet in nature, the resolution of the polygons is high enough that this approach yields an accurate description of which faces are actually affected by the oncoming air.

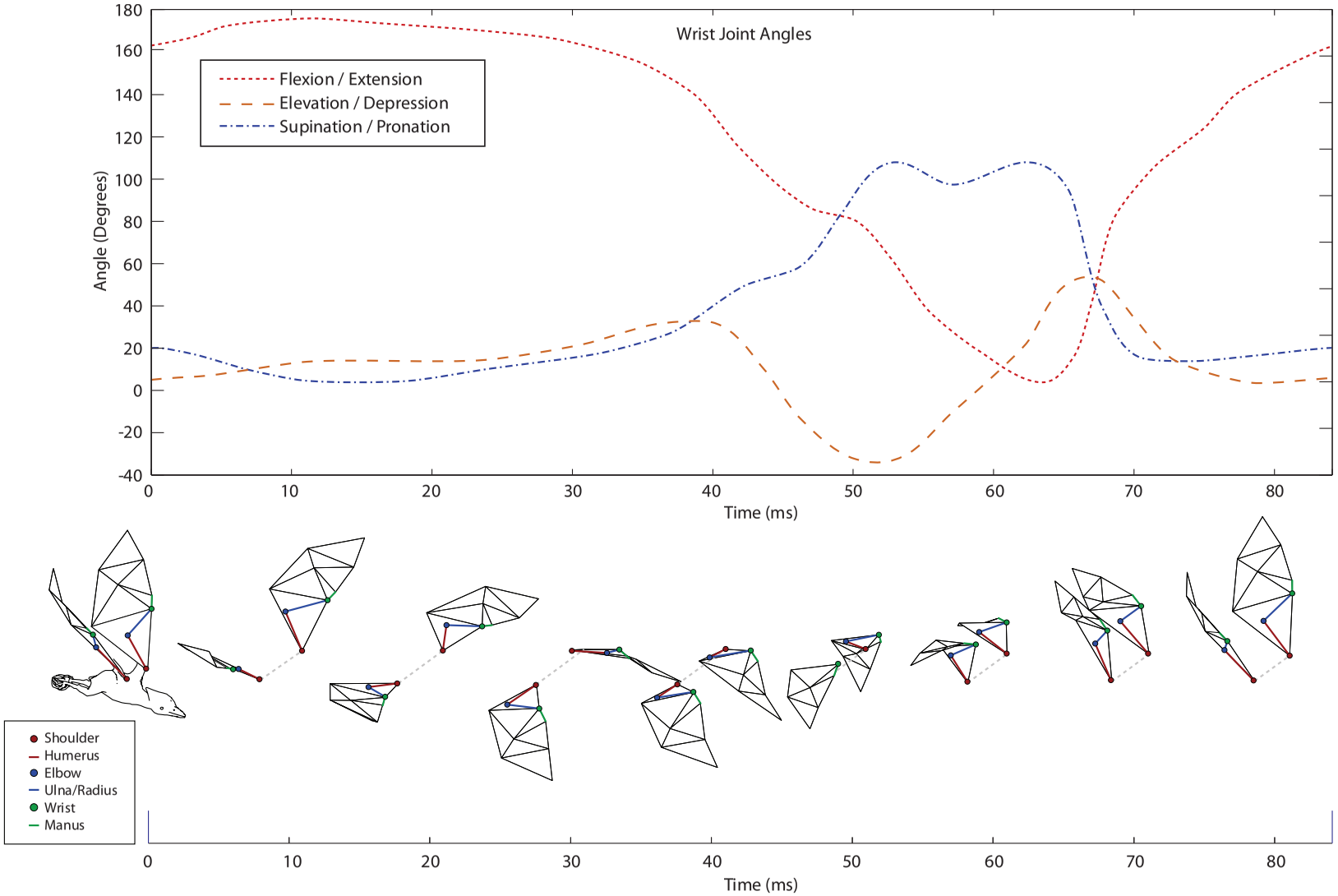

Figure 6.13: Wrist rotation animation curve for the three rotational axes

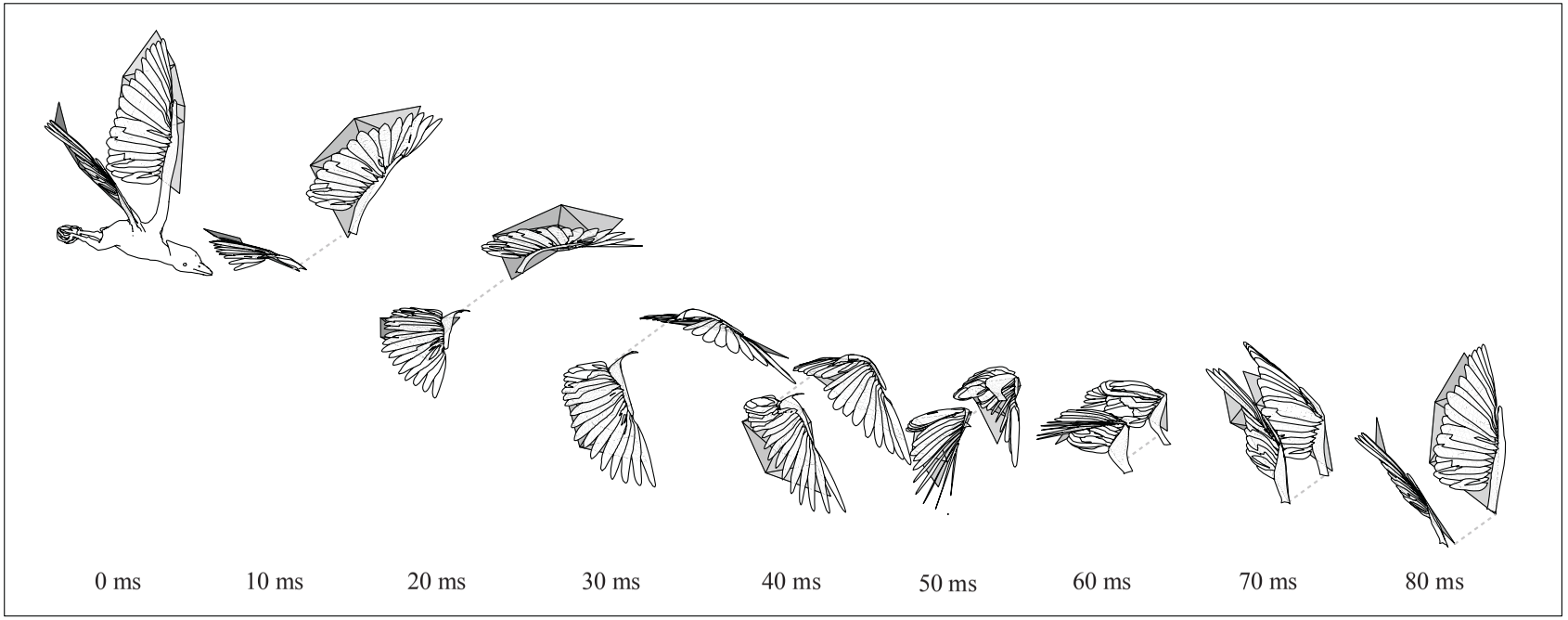

Figure 6.14: Perspective snapshots of fine feathered mesh overlaid on coarse mesh

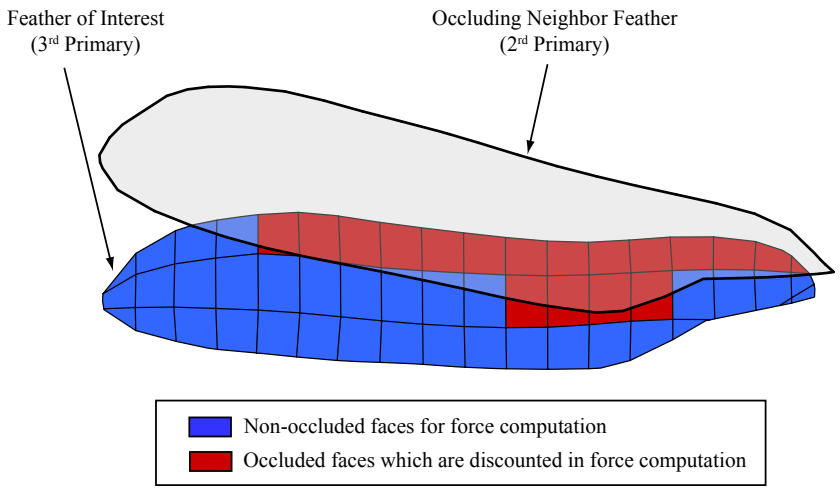

Figure 6.15: Example of feather occlusions showing the polygons in blue which are used in force computations, and the polygons in red which are occluded by a neighboring feather.

6.5 Rigid Feather Results

Figures 6.16 and 6.17 show the motion of the fine mesh from four viewpoints. We perform our numerical simulation on this fine mesh, as we did the coarse mesh in Section 6.2. While echoing similar trends as the coarse mesh, important differences arise between the two models.

First, we look at the surface area of the wing and compare it to the area of the coarse mesh in Figure 6.18. Both meshes follow the trend of maximizing wing surface area on the downstroke, and minimizing it on the upstroke. However, the fine mesh has a greater area for most of the wingbeat. This is likely due to the area of secondary feathers which lies outside the coarse mesh, as shown in Figure 6.19.

Comparing the mean angle of attack of the two meshes in Figure 6.20, we see that the angle of attack varies greatly between the meshes. Because each feather is rotated slightly in the transformation hierarchy to simulate the layering and non-

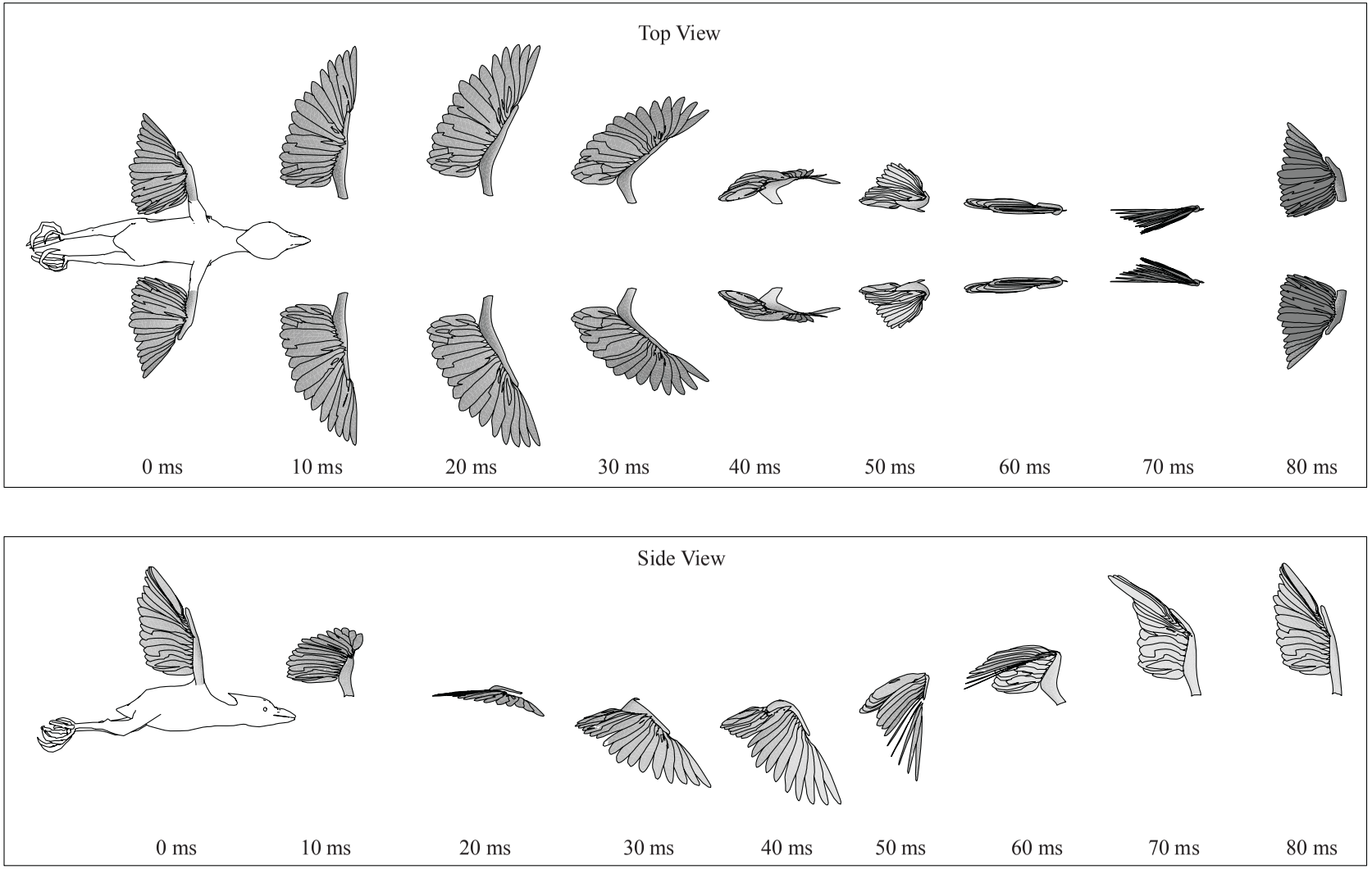

Figure 6.16: Top and side views of fine mesh wingbeat

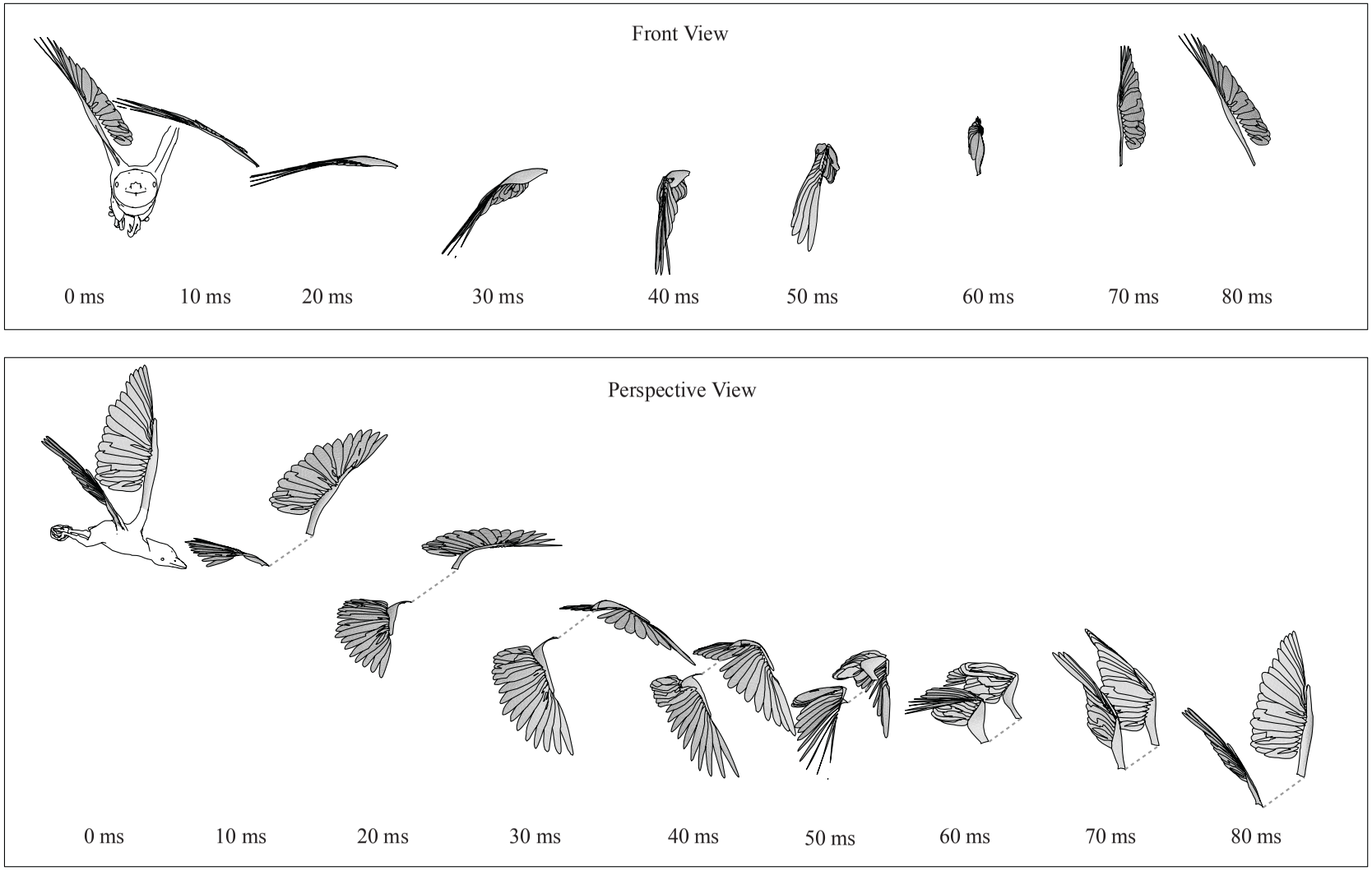

Figure 6.17: Font and perspective views of fine mesh wingbeat

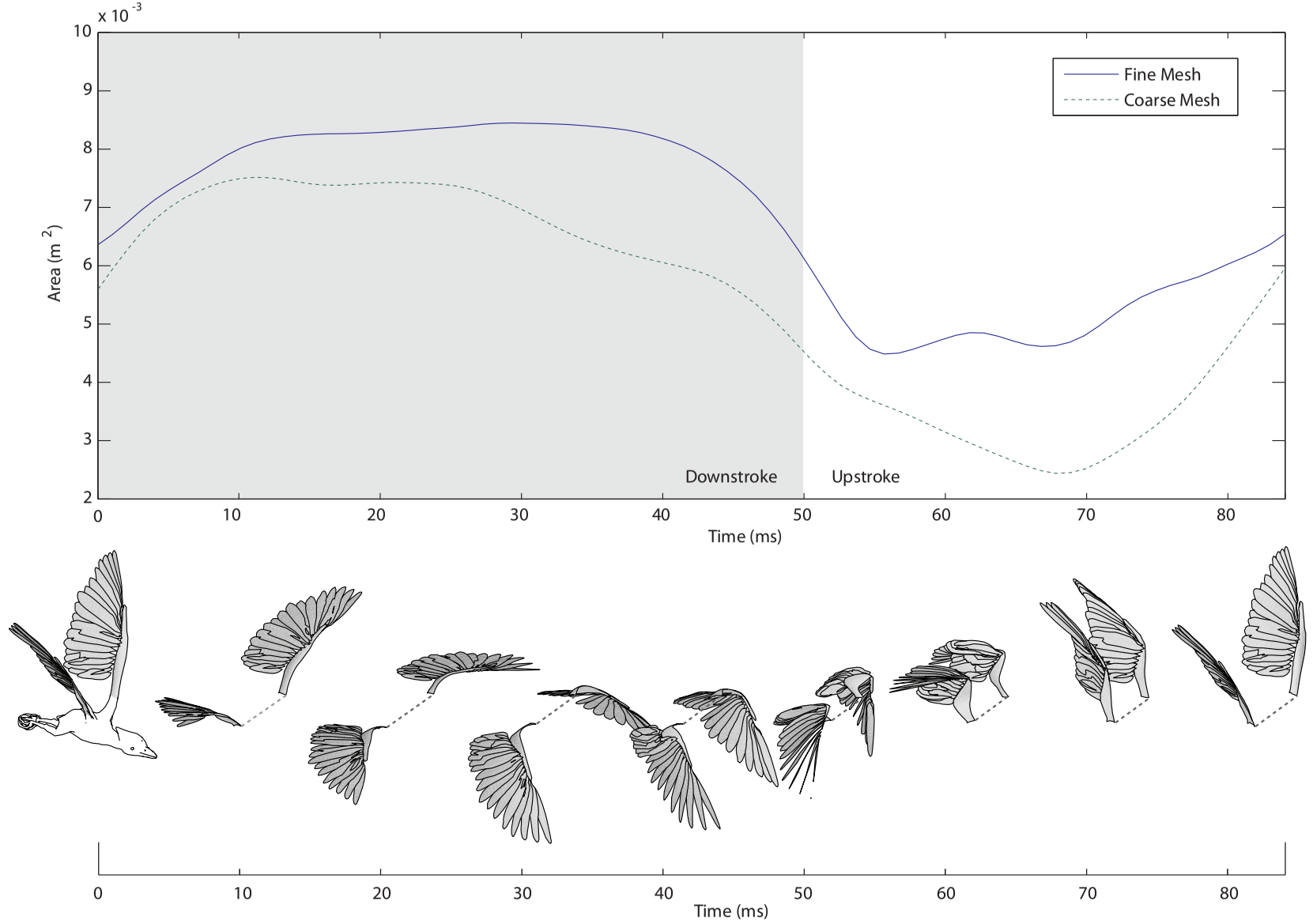

Figure 6.18: Total area of fine mesh compared with coarse mesh

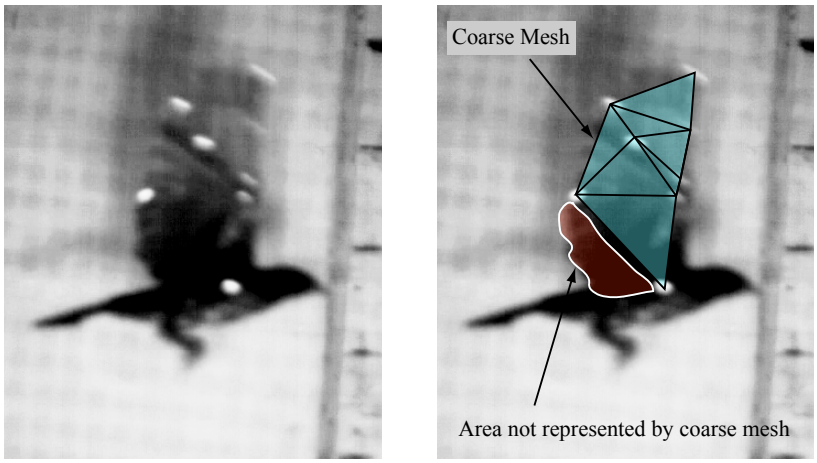

Figure 6.19: A reference frame from the high speed video showing the area of secondary feathers not represented by the coarse mesh model

intersection of feathers, each feather can have a greater angle of attack than a wide plane representing the feathers. We see that the fine mesh has a higher angle of attack in the downstroke, which is beneficial. Curiously though, we would expect to see the angle of attack minimized on the upstroke, but instead it hovers around twenty degrees on the upstroke of the fine mesh. The geometry of the feathers differs greatly from the coarse mesh on the upstroke, and the bird must move its wing through some lift-adverse poses in order to reach the top of the upstroke. Thus the higher-than-expected angle of attack on the upstroke may be a necessary sacrifice.

Figure 6.21 compares the mean speed of the fine mesh and coarse mesh. Both meshes exhibit high speed during the downstroke, and as well as a minima in speed at the beginning of the upstroke. The fine mesh has a comparatively lower speed during the downstroke. This can be attributed to the flexion of the elbow and wrist during the downstroke (refer to Figures 6.10, 6.12, and 6.13). The flexion of these two joints causes the feathers to close tighter together, and this motion reduces the absolute speed of the faces of these feathers. The irregularity of the speed during upstroke is due to the complex transformations of the feathers as

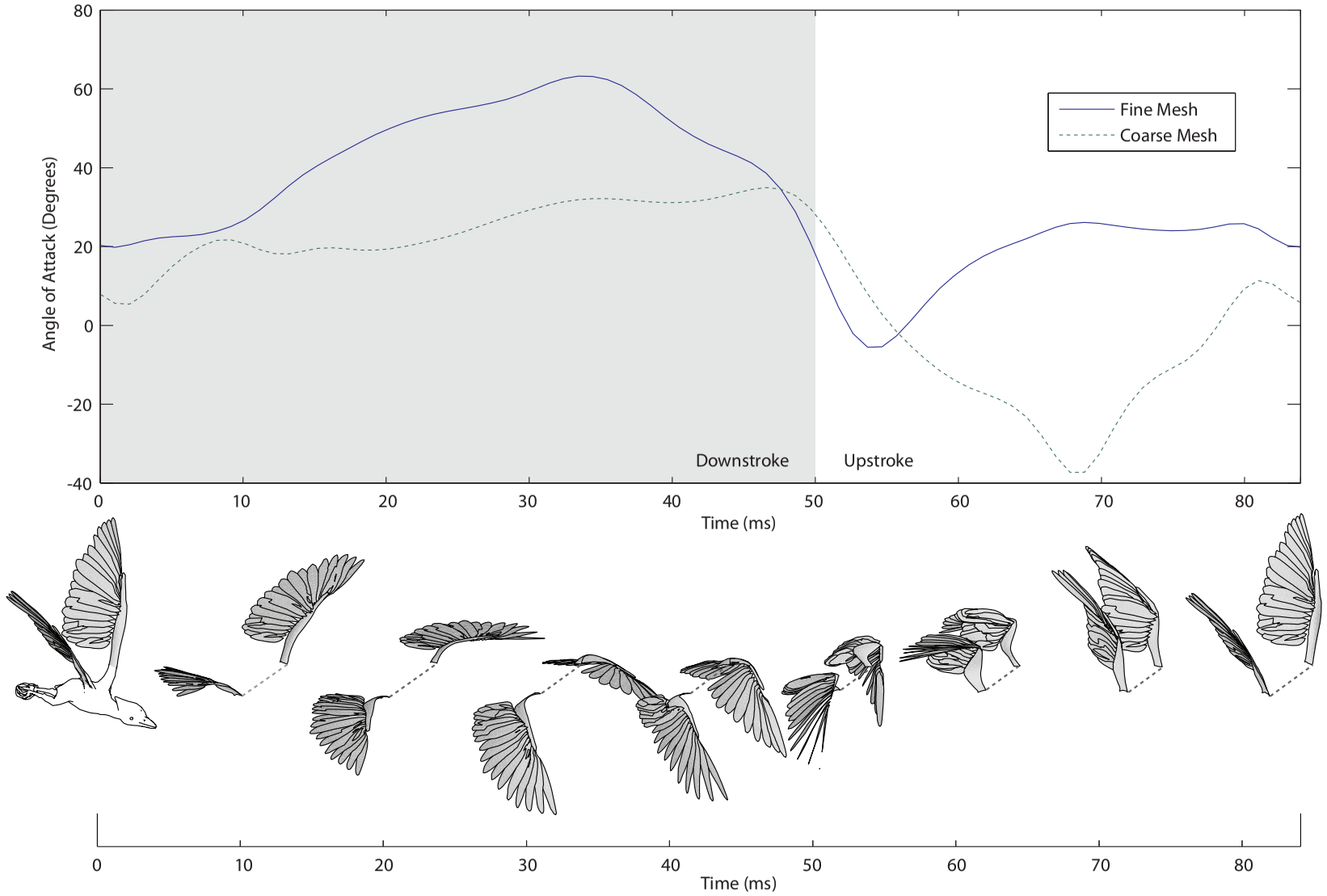

Figure 6.20: Instantaneous mean angle of attack of fine mesh compared with coarse mesh

compared the the coarse mesh.

Figure 6.22 shows the decomposition of the four force terms projected in the vertical direction. Again, the translational lift and drag terms provide the vast majority of the force. The unsteady terms, force due to added mass and rotational lift, play a comparatively smaller role in the fine mesh than in the coarse mesh. Of interest in this plot is the negative spike in drag force during the upstroke. The spreading of feathers due to wrist extension in preparation for the downstroke gives a momentary increase in vertical velocity to the feathers. The translational drag produces a net downward force in reaction to this movement of the feathers, explaining the spike.

Comparing the net combined force in the vertical direction of the fine mesh with that of the coarse mesh in Figure 6.23, we see the spike in drag on the upstroke mentioned above and we also notice that the three peaks in lift on the upstroke are smoothed out. Otherwise, the fine mesh and coarse mesh show similar trends.

Figure 6.24 shows the three dimensional components of the total instantaneous force. The vertical component is similar to that of the coarse mesh, as mentioned above. However, the side and forward axes show significant differences between the two meshes. In the forward direction, the major impulse comes at the end of the downstroke in the fine mesh, as opposed to the beginning of the downstroke in the coarse mesh. The side force in the distal direction (outward from the body of the bird) follows the same trend in the fine mesh as in the coarse mesh, but the peak around 70 milliseconds is greatly exaggerated in the fine mesh, enough so that it changes the sign of the integrated impulse. In this way, the each wing produces an outward impulse in the side axis as opposed to an inward impulse, although these impulses cancel out due to the opposing nature of the two wings.

Table 6.3 gives the computed force and impulse values for the fine mesh. In this

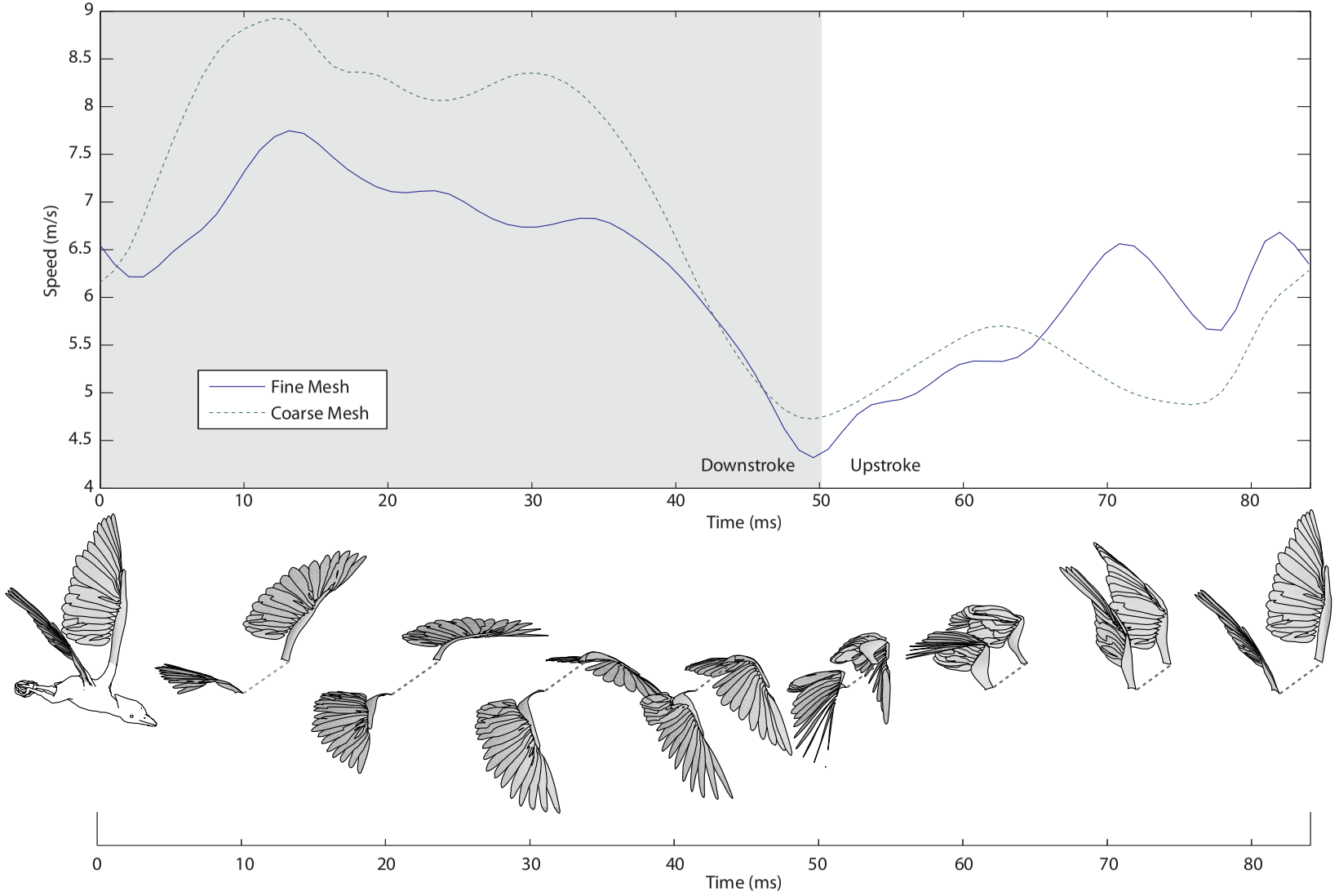

Figure 6.21: Instantaneous mean speed of fine mesh compared with coarse mesh

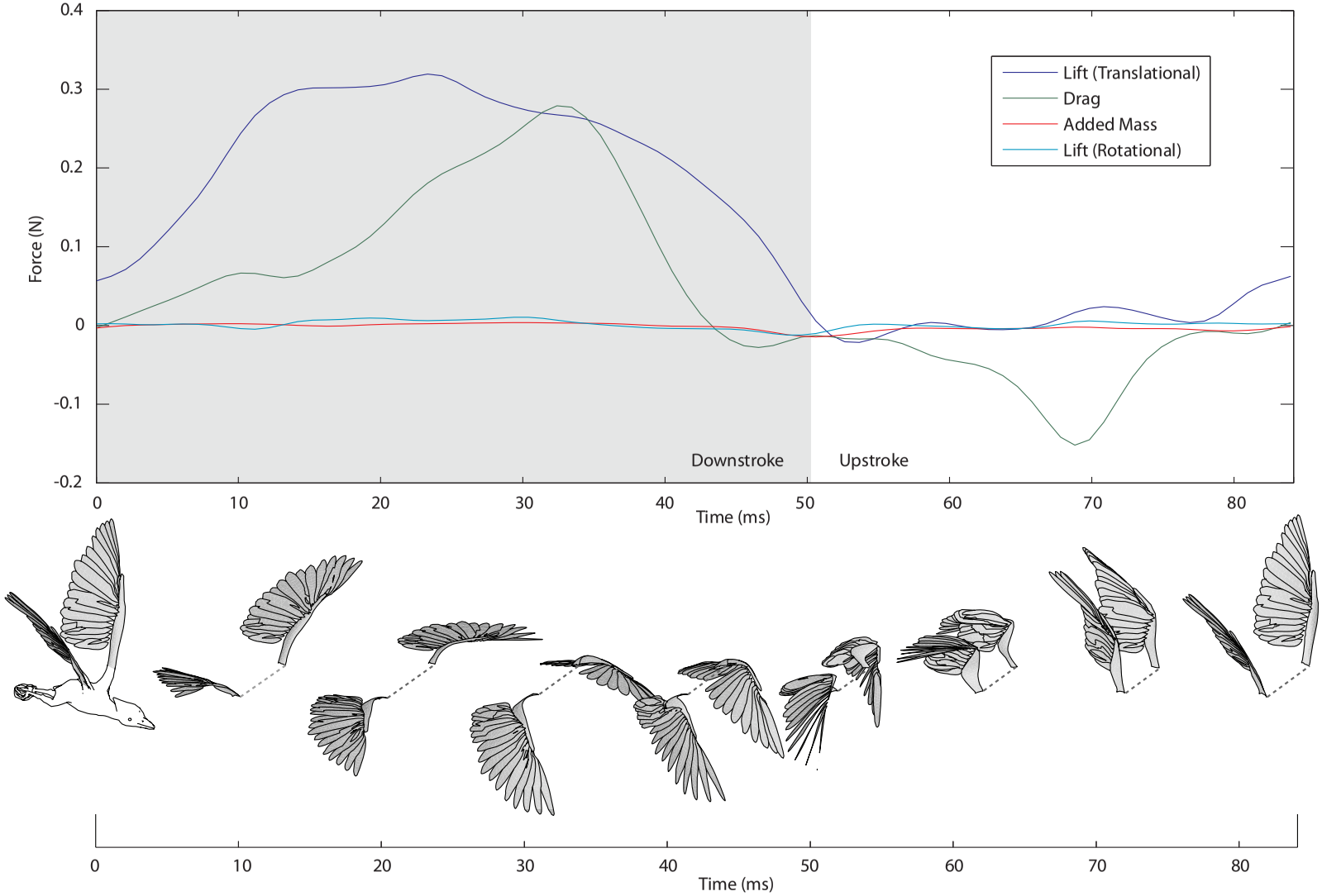

Figure 6.22: Components of instantaneous force in the vertical dimension of the fine mesh

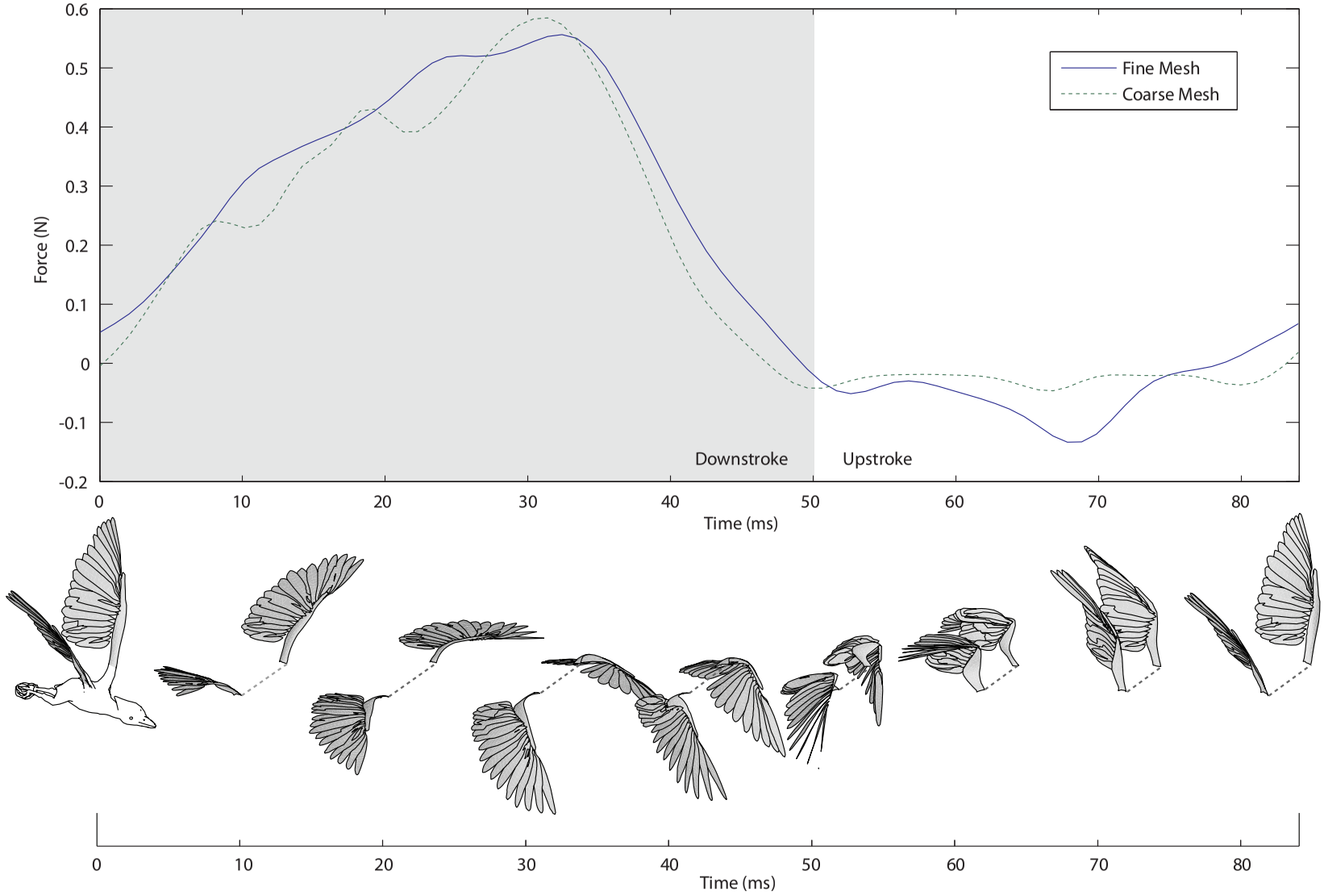

Figure 6.23: Total instantaneous vertical force of fine mesh compared with coarse mesh

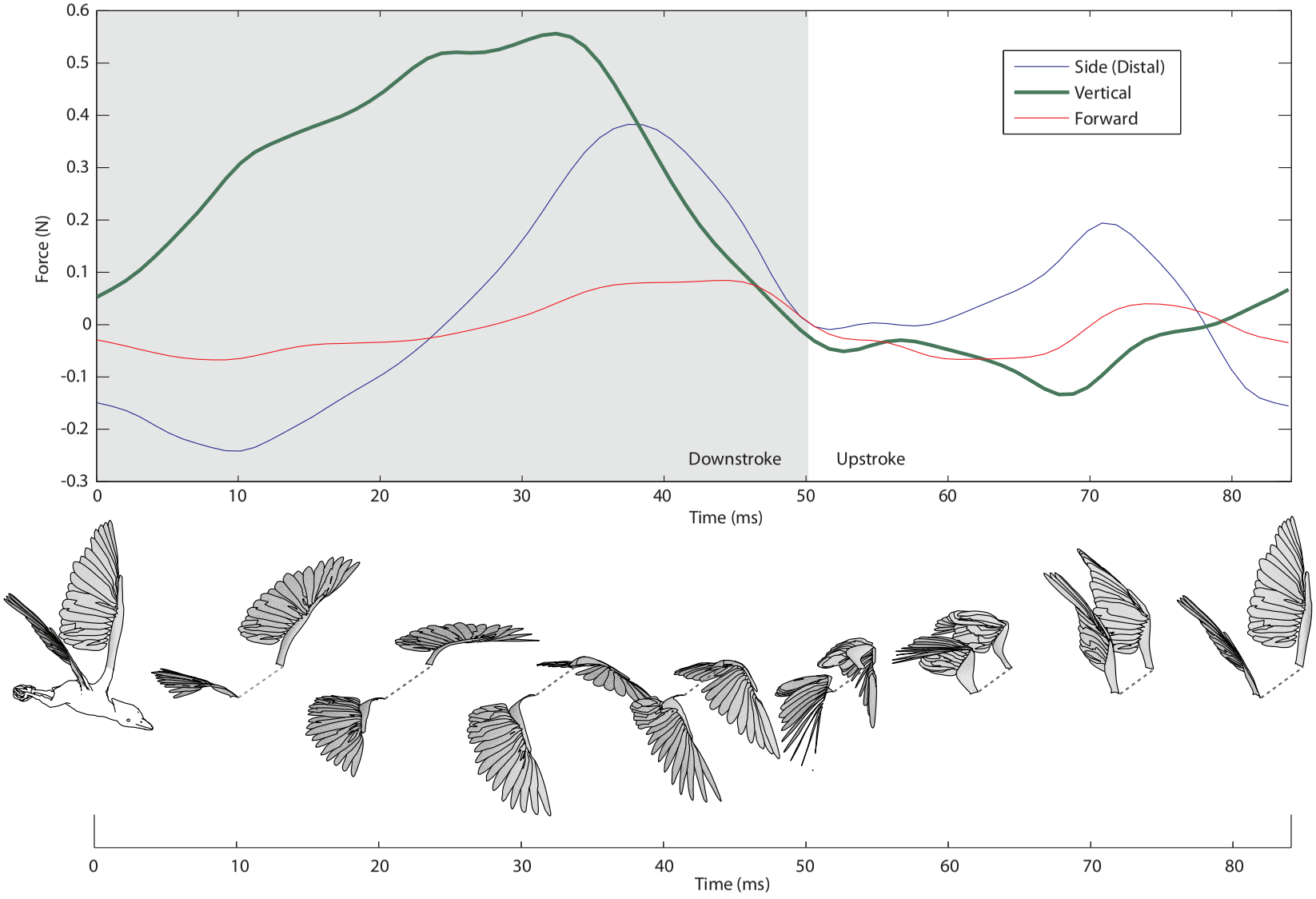

Figure 6.24: Total instantaneous force in three dimensions of the fine mesh

Table 6.3: Integrated impulse and average force values in three dimensions for one and both wings of the fine mesh

Term	Direction	Single Wing	Both Wings
Impulse I	**Vertical**	$I_y = 1.47 \times 10^{-2}\text{N} \cdot \text{s}$	$I_{y,bird} = 2.94 \times 10^{-2}\text{N} \cdot \text{s}$
	Forward	$I_x = 5.30 \times 10^{-4}\text{N} \cdot \text{s}$	$I_{x,bird} = 1.06 \times 10^{-3}\text{N} \cdot \text{s}$
	Side	$I_z = 2.89 \times 10^{-3}\text{N} \cdot \text{s}$	$I_{z,bird} = 0.00 \times 10^{-3}\text{N} \cdot \text{s}$
Average Force $\bar{F}$	**Vertical**	$\bar{F}_y = 1.77 \times 10^{-1}\text{N}$	$\bar{F}_{y,bird} = 3.54 \times 10^{-1}\text{N}$
	Forward	$\bar{F}_x = 6.39 \times 10^{-3}\text{N}$	$\bar{F}_{x,bird} = 1.28 \times 10^{-2}\text{N}$
	Side	$\bar{F}_z = 3.48 \times 10^{-2}\text{N}$	$\bar{F}_{z,bird} = 0.00 \times 10^{-2}\text{N}$

fine mesh simulation, $I_{y,bird}$ is slightly higher than in the coarse mesh simulation, and give a lift ratio of 83% (Equation 6.3), as compared with 76%.

$$r_{\text{lift}} = \frac{I_{\text{y,bird}}}{I^*} = \frac{2.94 \times 10^{-2}}{3.56 \times 10^{-2}} = 0.826 \tag{6.2}$$

6.6 Effects of Bend and Twist

The analysis of the fine mesh in Section 6.5 treats each feather as a rigid object. The arm deforms, but the feathers do not. While each whole feather undergoes translations and rotations, its shape is held constant. Actual feathers on a bird are not rigid, they bend and twist in complex ways. These non-linear deformations are difficult to simulate. One would need to know stiffness parameters of each feather such as the modulus of elasticity, spring coefficients, and damping coefficients. Furthermore, a soft-body simulation would also need to be run to resolve collisions between feathers and allow feathers in contact to exert forces on each other without intersecting. Finally, once those spring and collision models were implemented, an iterative solver would need to consider the interaction between the air and the feather and find a state for both the feather and the air which satisfies the conditions of the other. Such undertakings are the next logical step in this project,

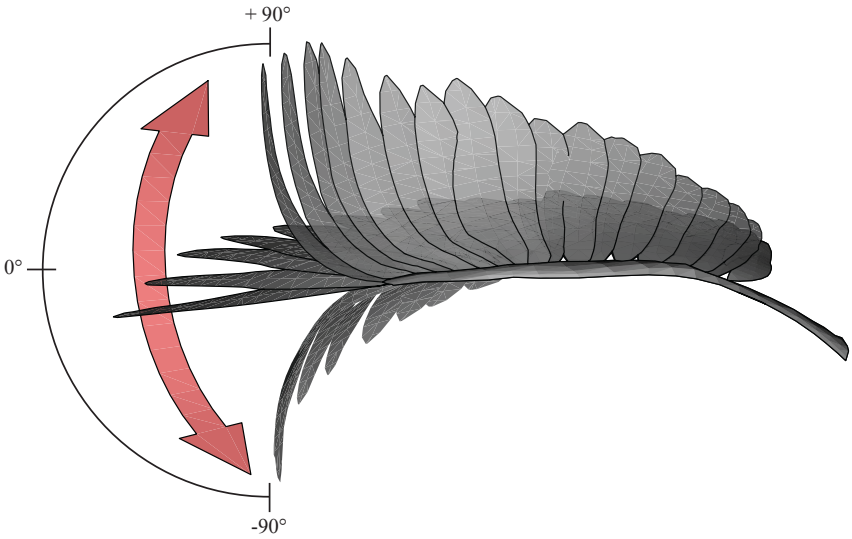

Figure 6.25: Non-rigid feathers deformed by bending

but here we limit ourselves to a preliminary investigation of the effects of user-defined feather bend and rotation.

This open-loop approach makes use of bend and rotation parameters which we built into the feather meshes. We interactively keyframe these parameters, using visual artistic evaluation to determine the amount of bend or rotation at each time step. This approach is distinct from a coupled feedback loop where the amount of bend or rotation would be determined by an optimization solver based on the external aerodynamic forces.

6.6.1 Bend

We first examine the effects of feather bend. We define feather bend as the degree of curvature beyond the feather's neutral state. For the wing, the ninth primary at the leading edge of the wing undergoes the full degree of bending, while the amount of bend falls off linearly among sequential feathers until it is zero at the ninth secondary at the base of the wing. This bend mimics the natural elasticity of the

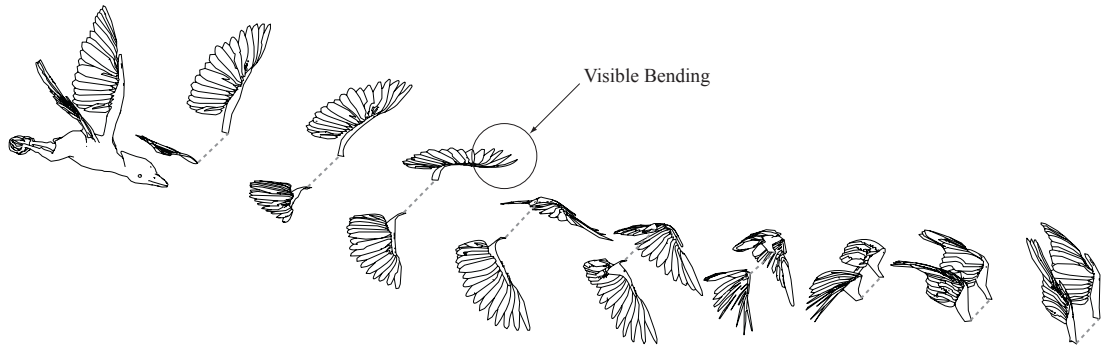

Figure 6.26: Perspective snapshots of fine mesh with bend. An area where feather bend is particularly evident is noted.

wing and provides a way to artificially recreate the deflection due to aerodynamic and inertial effects.

Figure 6.25 shows how the wing changes as it is bent from negative ninety degrees to positive ninety degrees. Figure 6.30 shows new snapshots of the bent feathers. Although there is some small degree of bending at each timestep, it is only evident in certain places, as indicated in the figure. Figure 6.27 shows the magnitude of bend throughout the wingbeat. As stated above, this amount of bend is a purely artistic interpretation based on the motion capture video and visual intuition. The results presented here are not intended to prove that the feathers actually bend in a particular way, but to give feedback as to how different types of deformation affect net force on the wing.

Figure 6.27 shows the particular bend motion which we tested. Here, we bend the wing during the downstroke to account for the strong forces of the air on the feathers. During the upstroke, we bend the wing in the opposite, negative, direction to account for the inertial bend as the wing changes direction. The peak and valley between 60 and 70 milliseconds accounts for a period during the upstroke where the wing speed fluctuates before accelerating in preparation for the downstroke around 80 milliseconds.

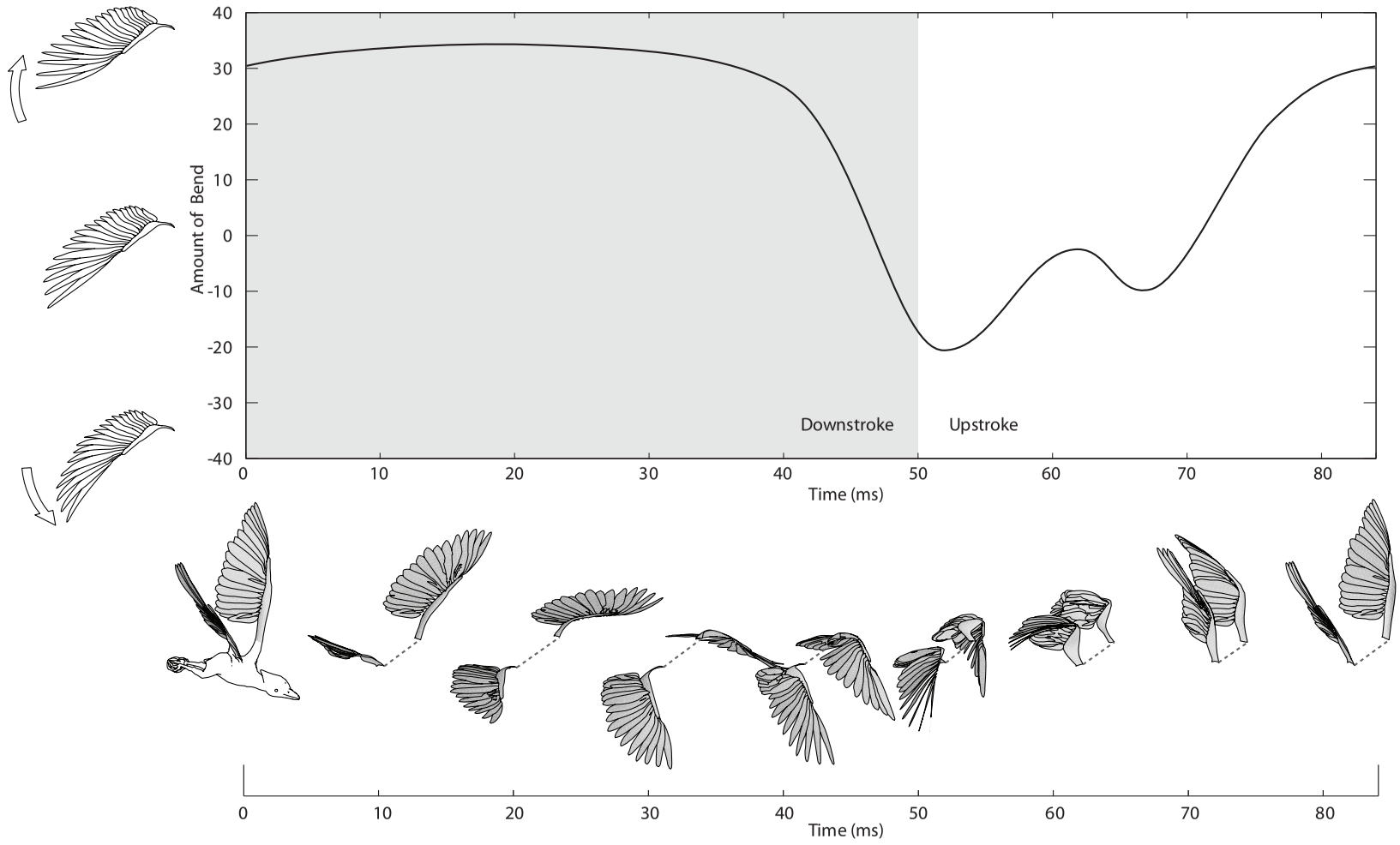

Figure 6.27: Animated feather-bend parameter over the wingbeat

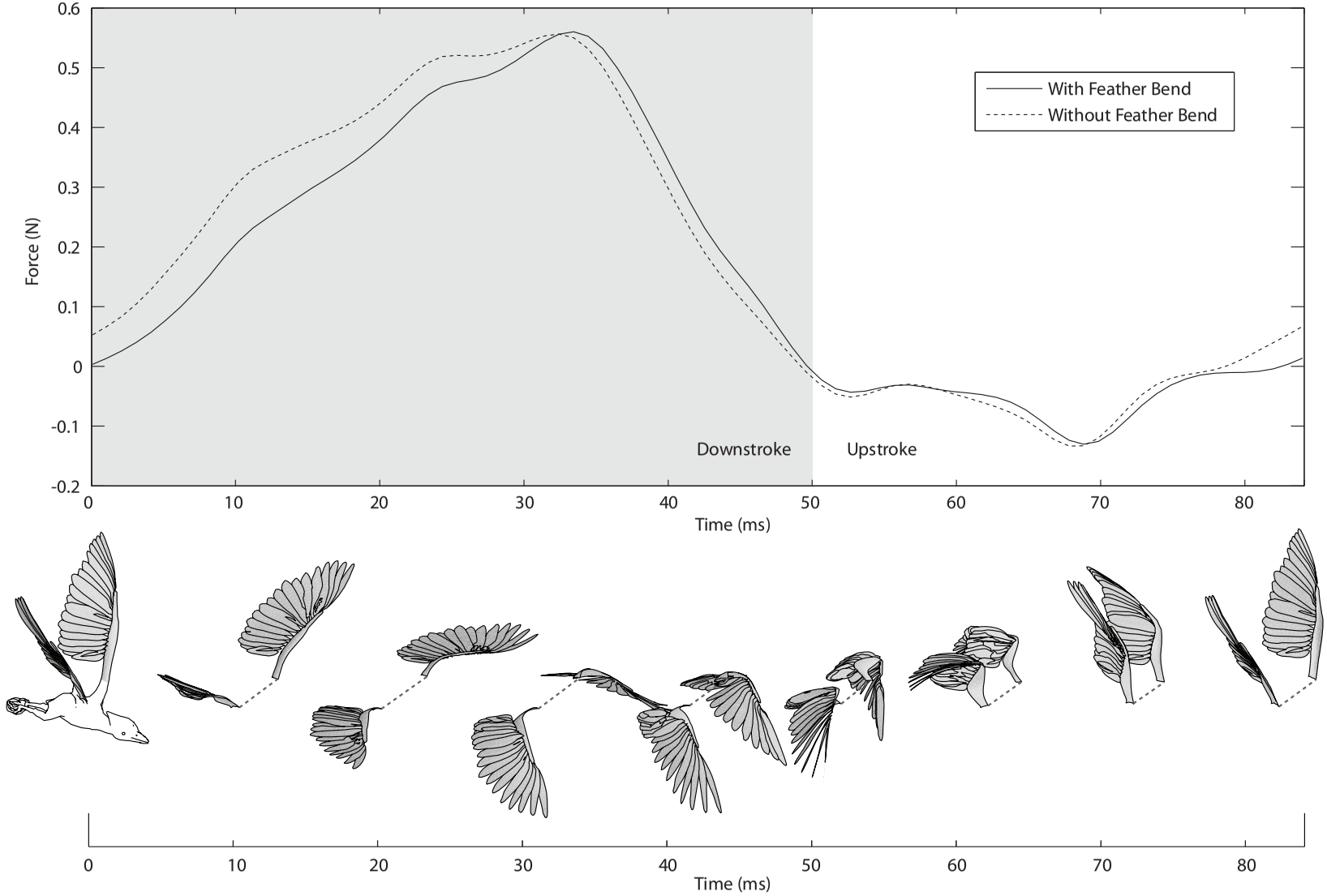

Figure 6.28: Total force resulting from wing with bending feathers versus rigid feathers

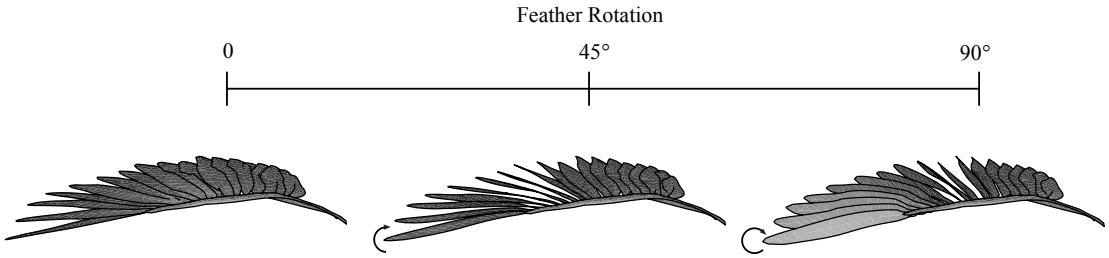

Figure 6.29: Feather rotation illustrated

$$r_{\text{lift}} = 0.739 \tag{6.3}$$

Figure 6.28 shows the resulting total vertical force for the bent wing versus the wing with rigid feathers. Contrary to expectations, the bend of the wing actually reduces lift during the downstroke, and has little effect during the rest of the wingbeat. Equation 6.3 shows that lift ratio drops by ten percent, from 83 to 73 percent. However, this is only one example of the infinite possible bend animations. In the future, one could implement a solver to determine the optimal bend profile for the wingbeat.

Lastly, it is worth noting that the marker positions from Holt's motion capture study are of course deformed to some degree by bending when they were recorded. Thus, the motion of the joints may already be reflecting a degree of spring or bend, and we may be attempting to add additional bend to a system which already contains this behavior.

6.6.2 Twist

In addition to bend, we also test the effects of feather rotation. The twist and rotation of each feather is not evident from the motion capture data, and thus far we have assumed that each feather is oriented as close to flat as possible with

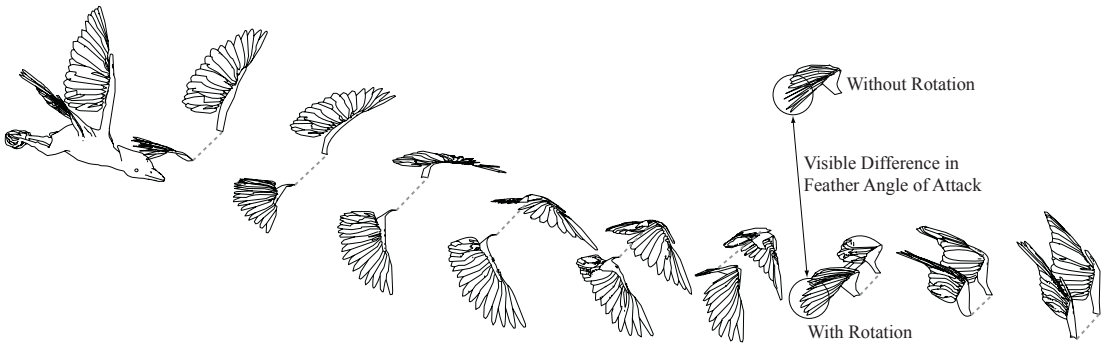

Figure 6.30: Perspective snapshots of fine mesh with animated feather rotations. An area where the difference is particularly visible is noted.

respect to the coarse mesh. However, each feather is held to the skin with a ligament which allows at least a small degree of rotation about the rachis. These rotations can affect the angle of attack of the feathers, especially the primary feathers. We define a feather rotation parameter that varies this orientation of each feather about its rachis, the long axis. Figure 6.29 shows the wing as the feather rotation parameter varies from zero to ninety degrees. Similar to the wing bend above, the ninth primary feather rotates the full amount specified, and then the amount of rotation falls off linearly until the ninth secondary feather does not rotate.

Figure 6.30 shows snapshots of the wing with rotations implemented, following the profile curve shown in Figure 6.31. This profile attempts to minimize drag on the upstroke by twisting the feathers to present less of a profile to the oncoming air, and then to maximize the angle of attack of the feathers on the downstroke.

$$r_{\text{lift}} = 0.879 \tag{6.4}$$

Figure 6.32 shows the resulting force from this feather rotation test. A distinct increase in lift occurs during the middle portion of the downstroke. We also see an unexpected increase in drag during the upstroke. This increase in lift on the

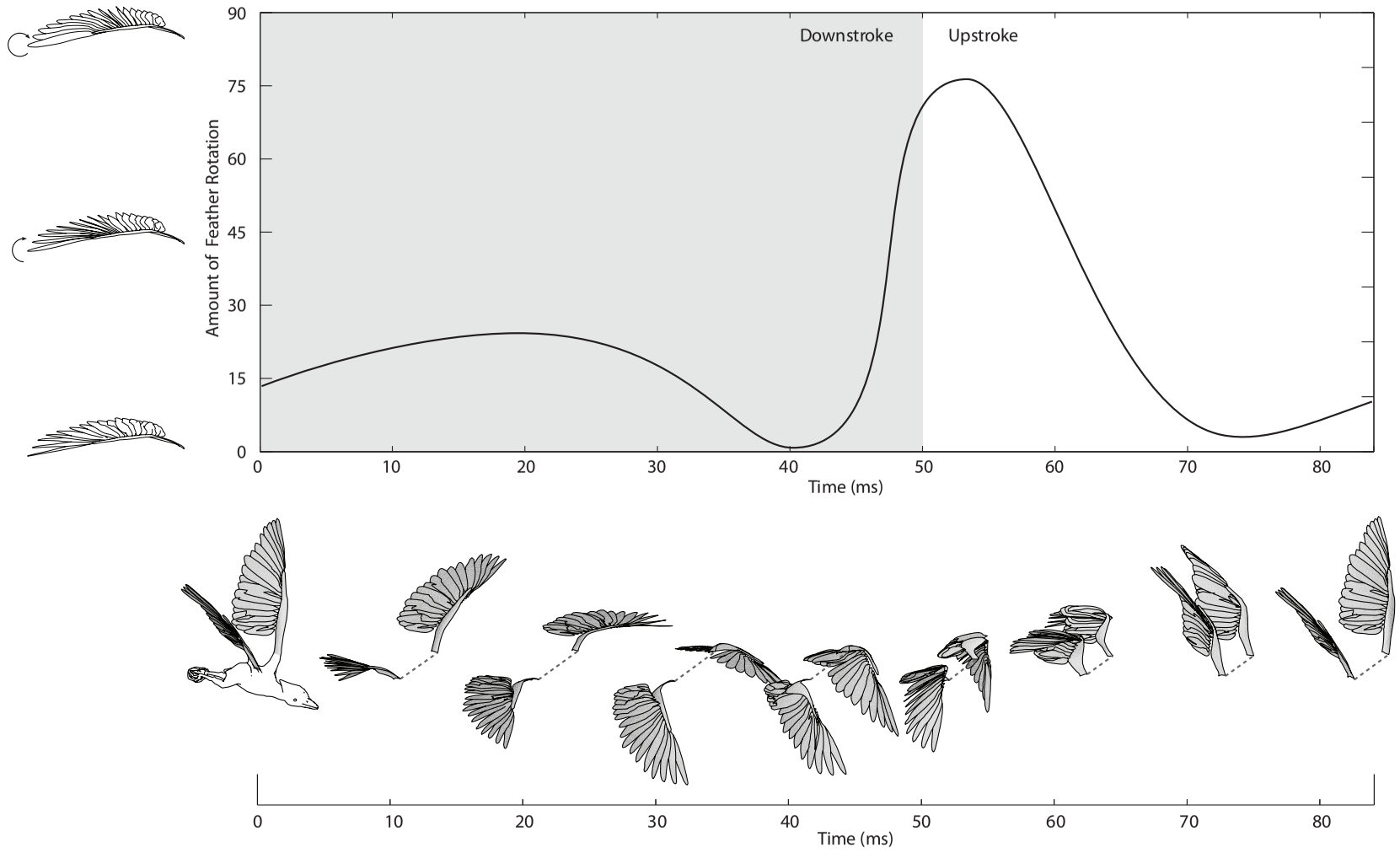

Figure 6.31: Feather rotation parameter animated throughout the wingbeat

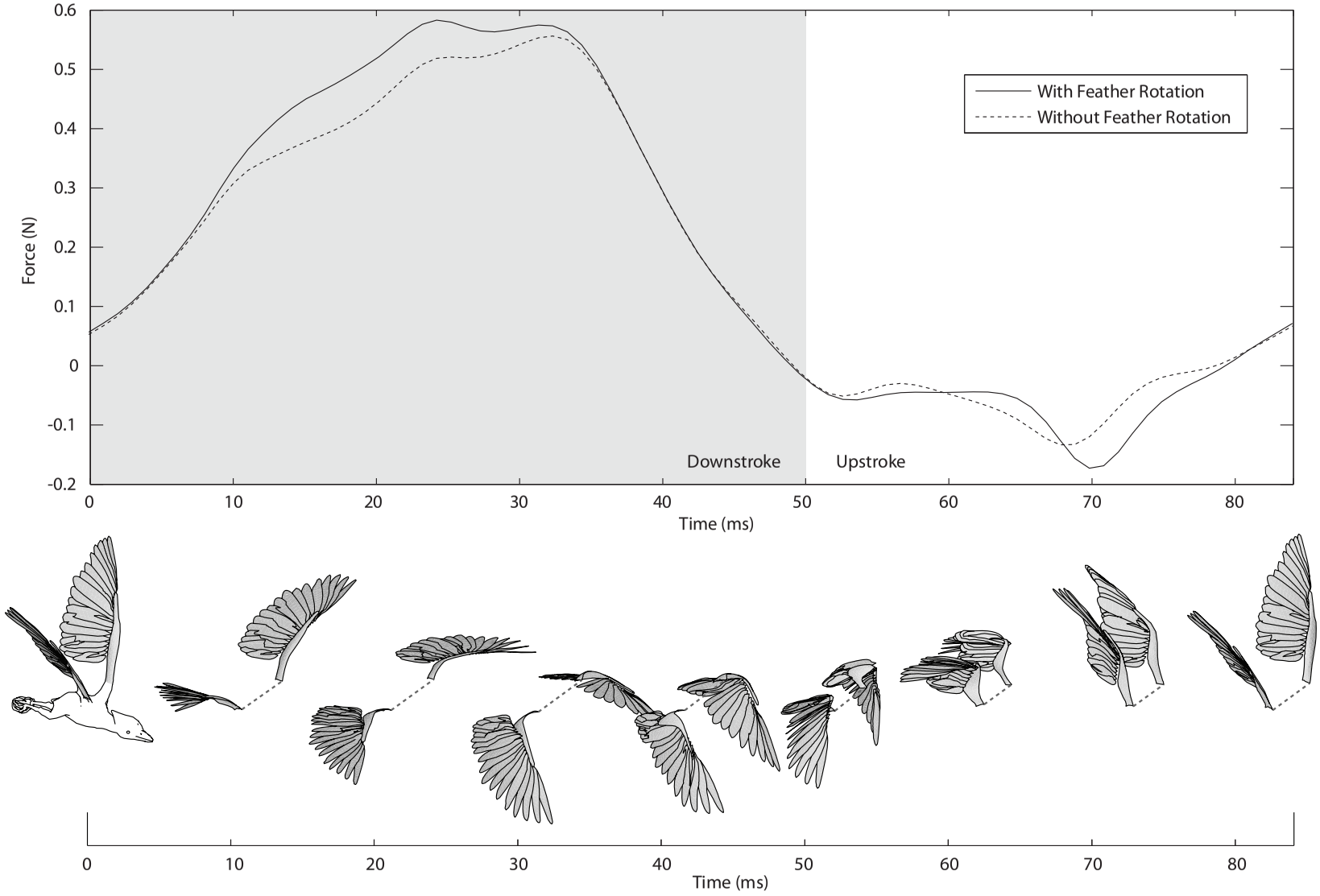

Figure 6.32: Total force resulting from wing with dynamic feather rotation versus static feather rotation

downstroke is enough to overcome the extra drag, however, and produces a lift ratio of 88 percent (Equation 6.4), five percent higher than the results from the rigid simulation without additional rotation.

These investigations of the effects of feather bend and rotation show that we can "tweak" the virtual model to produce more lift and approach the weight of the bird. However, more detailed data will be needed to determine the physical validity of these additions to the kinematic model.

CHAPTER 7

CONCLUSION

We have shown how we built and animated a digital Red-winged blackbird, and used aerodynamics to compute forces on the bird's wings for two different geometric cases: a coarse mesh providing an approximation of wing shape, and a fine mesh consisting of individual feathers. The impulse predicted by the coarse mesh case supported 76% of the weight of the bird. The fine mesh accounted for a slightly greater impulse, at 83% of the weight of the bird. We experimented with user controlled bend and rotation of feathers and achieved a slightly higher still impulse of 88% of the bird's weight.

It must be stressed, however, that these results represent only a first-order estimate of force. We make many assumptions to the aerodynamic model which detract from its precision, though not necessarily its accuracy. Further validation by comparison to other aerodynamic methods such as the lifting line method are needed. In addition, this work is built on motion capture data which contains inaccuracies, and even a small change to joint rotations can greatly affect angle of attack and therefore forces. However, the blade element model can produce macro-scale representative trends, even if the micro-scale values from face to face contain error. This work has a large qualitative, if not quantitative, potential to reveal masked features of flapping bird flight.

The data used to construct this wingbeat of a Red-winged blackbird is culled from different sources, and while each source is thorough, there is room for improvement when combined. The computer generated rigged model of the bird is based on Jeffery Wang's Ivory-billed woodpecker, which was developed from a CT scanned specimen. While woodpeckers and blackbirds share many traits, it would have been advantageous for our study, though impractical, to construct an

anatomically correct rigged model based on a Red-winged blackbird.

Brendan Holt's motion captured wingbeat provided a wealth of information and the basis of our animated motion. Although infeasible for Holt's work, it is possible to obtain better and more accurate data using more markers, more cameras, more time, and a more natural flying environment. With more markers we could have determined a more thorough picture of joint positions, feather orientation and bending, feather spread, and position of the body of the bird. Instead, we must guess at values like placement of the elbow joint. In addition, we would like to be able to capture the opposing wing's motion as well. We have assumed symmetry between the two wings, but this may not necessarily be the case even in straight and level flight. A longer capture time would allow us to capture more than one wingbeat and analyze how each flap deviates from the previous one. Lastly, although there is good evidence to support the fact that birds fly more naturally in the still air of a flight tunnel than the moving air of a wind tunnel [Ray94], we would still have preferred to record the bird flying in open setting to achieve the most natural flight movements possible.

Lastly, our model did not consider lift or drag on the body of the bird or the tail feathers. Motion capturing and simulating these parts of the bird would complete the task of simulating force on the entire bird instead of just the wings.

While the results presented in Chapter 6 are encouraging, there are no prior studies of measured instantaneous forces on bird wings with which to compare. In addition, it must be understood that we have made many aerodynamic simplifications which potentially affect the accuracy of the model. The blade element model and thin airfoil theory in general are designed to operate on simple geometry under steady-state conditions. The model assumes that flow conditions are steady or close to steady such that airflow around each blade, or slice of a wing, is similar

to airflow around a neighboring slice. Our model treats each blade independently, with no knowledge of what is happening elsewhere on the wing or previously in time.

We are certainly utilizing the blade element model in an unconventional way. Specifically, the assumption is that the represented geometry is projected onto a blade which extends from the leading edge of the wing to the trailing edge of the wing. In our model, each blade is a polygon whose leading and trailing edges do not correspond with the leading and trailing edges of the wing, but instead lie somewhere within the boundary of the wing as a whole.

The quasi-steady state nature of the blade element model also adds uncertainty to our model. Traditionally, the quasi-steady approximation has proved reasonable because the state of the wing changes slowly enough. However, our bird wing is undergoing rapid movements. We attempted to capture the unsteady effects by computing the transient forces due to added mass and rotational lift. However, our simulator produced less force than expected.

The blade element model is appropriate for most values of the Reynolds number. However, our additional force terms, forces due to added mass and rotational lift, are borrowed from insect flight studies. These studies examine airflow at much lower Reynolds numbers, and therefore these terms may not be applicable to our comparably higher Reynolds number flow. However, these forces end up being small in magnitude, especially in the fine mesh simulation, and therefore the question of Reynolds number is of little consequence.

Despite these simplifying assumptions, we find great value in this work when taken as a first-order of magnitude simulation and a description of general force trends. The strength of this project lies in its interactivity and its usefulness as a visualization tool. It gives scientists and artists alike a representative picture of

the forces in a simulation so that they can understand the effects of the system or make changes to the motion.

The potential for future work in the area of simulating bird flight is unlimited. The next logical addition to the model may be to implement physically-based feather bending. This would require measuring the stiffness of physical feathers. Several studies exist which have begun to document the material properties of feathers, including the modulus of elasticity and cross-sectional profile of the rachis [PV78, BP95]. Knowing these parameters, one could treat the feather as a cantilever beam, and determine flexure using bending equations from mechanical engineering.

Next, the addition of a soft-body collision simulator to the virtual feathers would be needed to prevent feathers from interpenetrating and allow them to exert force on each other. Additionally, distribution of mass measurements of feathers and the bird itself would allow inertial forces arising from the flapping motion to be taken into account when computing feather deformation and bending. A coupled solver would iteratively find the state at which the conditions of airflow, feather spring, and body inertia, are all satisfied.

Further wind tunnel and CFD testing should not be discounted. The wind tunnel can be used to experiment on physical specimen wings to determine how they differ from numerical simulations in the steady state. CFD software is constantly evolving and may soon be able to process the complex geometry and time-dependent deformation of a flapping wind. The advantage of CFD's highly accurate numerical method cannot be ignored. Also worth considering in the future are vortex panel methods, a quasi-numeric simulation technique using potential flow equations to compute flow conditions around airfoils [SWW96, KP01].

There are many directions to build upon this work. Visualizing three-dimensional

data such as the force on a bird wing is a challenging problem, and new display techniques are always emerging. Applying our method to other species of birds, and even aquatic swimming animals would be an interesting endeavor. We have built a framework which is based on discreet geometric elements and can therefore be extended to make use of new techniques and be used in new experiments. The possibilities are unlimited.

BIBLIOGRAPHY

[AAK71] Y. I. Abdel-Aziz and H. M. Karara. Direct linear transformation from comparator coordinates into object space coordinates in close-range photogrammetry. *Proceedings of the Symposium on Close-Range Photogrammetry*, pages 1–18, 1971.

[And00] John D. Anderson. *Introduction to Flight.* McGraw-Hill, 2000.

[And01] John D. Anderson. *Fundamentals of Aerodynamics.* McGraw-Hill, 2001.

[APW05] A. Andersen, U. Pesavento, and Z. Jane Wang. Unsteady aerodynamics of fluttering and tumbling plates. *Journal of Fluid Mechnics*, 541:65–90, 2005.

[BP95] Richard H. C. Bonser and Peter P. Purslow. The young's modulus of feather keratin. *The Journal of Experimental Biology*, 198(4):1029–1033, 1995.

[BW07] Gordon J. Berman and Z. Jane Wang. Energy-minimizing kinematics in hovering insect flight. *Journal of Fluid Mechnics*, 582:153–168, 2007.

[Cha43] Frank Wilbut Chamberlain. *Atlas of Avian Anatomy.* Hallenbeck Printing Company, 1943.

[DD04] William B. Dickson and Michael H. Dickinson. The effect of advance ratio on the aerodynamics of revolving wings. *Journal of Experimental Biology*, 207:4269–4281, 2004.

[DG93] Michael H. Dickinson and Karl G. Gotz. Unsteady aerodynamic performance of model wings at low reynolds numbers. *Journal of Experimental Biology*, 174:45–64, 1993.

[DJJ91] Kenneth P. Dial, G. E. Goslow Jr., and Farish A. Jenkins Jr. The functional anatomy of the shoulder in the European starling (*Sturnus vulgaris*). *Journal of Morphology*, 207(3):327–344, 1991.

[Ell84a] C. P. Ellington. The aerodynamics of hovering insect flight. i. the quasi-steady analysis. *Philosophical Transactions of the Royal Society of London. Series B, Biological Sciences*, 305(1122):1–15, 1984.

[Ell84b] C. P. Ellington. The aerodynamics of hovering insect flight. iii. kinematics. *Philosophical Transactions of the Royal Society of London. Series B, Biological Sciences*, 305(1122):1–15, 1984.

[Ell84c] C. P. Ellington. The aerodynamics of hovering insect flight. ii.morphological parameters. *Philosophical Transactions of the Royal Society of London. Series B, Biological Sciences*, 305(1122):17–40, 1984.

[Ell84d] C. P. Ellington. The aerodynamics of hovering insect flight. iv. aeorodynamic mechanisms. *Philosophical Transactions of the Royal Society of London. Series B, Biological Sciences*, 305(1122):79–113, 1984.

[Ell84e] C. P. Ellington. The aerodynamics of hovering insect flight. v. a vortex theory. *Philosophical Transactions of the Royal Society of London. Series B, Biological Sciences*, 305(1122):115–144, 1984.

[Ell84f] C. P. Ellington. The aerodynamics of hovering insect flight. vi. lift and power requirements. *Philosophical Transactions of the Royal Society of London. Series B, Biological Sciences*, 305(1122):145–181, 1984.

[FLL+05] John W. Fitzpatrick, Martjan Lammertink, Jr. Luneau, M. David, Tim W. Gallagher, Bobby R. Harrison, Gene M. Sparling, Kenneth V. Rosenberg, Ronald W. Rohrbaugh, Elliott C. H. Swarthout, Peter H. Wrege, Sara Barker Swarthout, Marc S. Dantzker, Russell A. Charif, Timothy R. Barksdale, Jr. Remsen, J. V., Scott D. Simon, and Douglas Zollner. Ivory-billed woodpecker (campephilus principalis) persists in continental north america. *Science*, 308(5727):1460–1462, 2005.

[Goo92] David Goodnow. *How Birds Fly.* Periwinkly Books Incorporated, Columbia, Maryland, 1992.

[Hed08] Tyson L. Hedrick. Software techniques for two- and three-dimensional kinematic measurements of biological and biomimetic systems. *Bioinspiration & Biomimetics*, 3:1–6, 2008.

[Hol09] Brendan Alec Holt. Motion capture of a red-winged blackbird in free flight. Master's thesis, Cornell University, 2009.

[HTB02] Tyson L. Hedrick, Bret W. Tobalske, and Andrew A. Biewener. Estimates of circulation and gait change based on a three-dimensional kinematic analysis of flight in cockatiels (*Nymphicus hollandicus*) and

ringed turtle-doves (*Streptopelia risoria*). *The Journal of Experimental Biology*, 205:1389–1409, 2002.

[HUB04] Tyson L. Hedrick, James R. Usherwood, and Andrew A. Biewener. Wing inertia and whole-body acceleration: an analysis of instantaneous aerodynamic force production in cockatiels (*Nymphicus hollandicus*) flying across a range of speeds. *The Journal of Experimental Biology*, 207:1689–1702, 2004.

[Jr.07] John B. Dunning Jr., editor. *CRC Handbook of Avian Masses*. CRC Press, Boca Raton, FL, 2nd edition, 2007.

[KBD35] T. Von Karman, J. M. Burgers, and W. F. Durand. *Aerodynamic Theory: Vol. 2*. Springer, Berlin, 1935.

[KP01] Joseph Katz and Allen Plotkin. *Low-Speed Aerodynamics*. Cambridge University Press, 2nd edition, 2001.

[Lig73] M. J. Lighthill. On the weis-fogh mechanism of lift generation. *Journal of Fluid Mechnics*, 60(1):1–17, 1973.

[LS72] Alfred M. Lucas and Peter R. Stettenheim. *Avian Anatomy: Integument, Part I*. U.S. Government Printing Office, 1972.

[Max79] T. Maxworthy. Experiments on the weis-fogh mechanism of lift generation by insects in hovering flight. part1. dynamics of the 'fling'. *Journal of Fluid Mechnics*, 93(1):47–63, 1979.

[MBG05] Andrew I. March, Charles W. Bradley, and Ephrahim Garcia. Aerodynamic properties of avian flight as a function of wing shape. *ASME Conference Proceedings*, pages 955–963, November 2005.

[MHD99] Sanjay P. Sane Michael H. Dickinson, Fritz-Olaf Lehmann. Wing rotation and the aerodynamic basis of insect flight. *Science*, 284(5422):1954–1960, June 1999.

[MSS92] D Meyers, S Skinner, and K Sloan. Surfaces from contours. *ACM Transactions on Graphics*, 11(3):228–258, 1992.

[Nor90] Ulla M. Norberg. *Vertebrate Flight*. Springer-Verlag, 1990.

[NTT04] Robert L Nudds, Graham K. Taylor, and Adrian L. R. Thomas. Tuning of strouhal number for high propulsive efficiency accurately predicts how wingbeat frequency and stroke amplitude relate and scale with size and flight speed in birds. *Proceedings: Biological Sciences*, 271(1552):2071–2076, 2004.

[PL93] Noble S. Proctor and Patrick J. Lynch. *Manual of Ornithology: Avian Structure and Function*. Yale University Press, New Haven and London, 1993.

[PV78] P. P. Purslow and J.F. V. Vincent. Mechanical properties of primary feathers from the pigeon. *The Journal of Experimental Biology*, 72:251–260, 1978.

[Ray79a] J. M. V. Rayner. A vortex theory of animal flight. part 1. the vortex wake of a hovering animal. *Journal of Fluid Mechnics*, 91(4):697–730, 1979.

[Ray79b] J. M. V. Rayner. A vortex theory of animal flight. part 2. the forward flight of birds. *Journal of Fluid Mechnics*, 91(4):731–763, 1979.

[Ray94] Jeremy M. V. Rayner. Aerodynamic corrections for the flight of birds and bats in wind tunnels. *Journal of Zoology*, 234(4):537–5636, 1994.

[RW99] Balajee Ramakrishnananda and Kok Cheong Wong. Animating bird flight using aerodynamics. *Visual Computer*, 15(10):494–508, 1999.

[SD01] Sanjay P. Sane and Michael H. Dickinson. The control of flight force by a flapping wing: Lift and drag production. *Journal of Experimental Biology*, 204(2607-2626), 2001.

[SD02] Sanjay P. Sane and Michael H. Dickinson. The aerodynamic effects of wing rotation and a revised quasi-steady model of flapping flight. *Journal of Experimental Biology*, 205:1087–1096, 2002.

[Sed65] L. I. Sedov. *Two-Dimensional Problems in Hydrodynamics and Aerodynmics*. Interscience Publishers, 1965.

[SFF91] M. R. Stytz, G. Frieder, and O. Frieder. Three-dimensional medical imaging: algorithms and computer systems. *ACM Comput. Surv.*, 23(4):421–499, 1991.

[Spe86] G. R. Spedding. The wake of a jackdaw (corvus monedula) in slow flight. *Journal of Experimental Biology*, (125):287–307, 1986.

[Spe87] G. R. Spedding. The wake of a kestrel (falco tinnunculus) in flapping flight. *Journal of Experimental Biology*, (127):59–78, 1987.

[Spe03] G.R. Spedding. On the significance of unsteady effects in the aerodynamic performance of flying animals. In A. Y. Cheer and C. P. van Dam, editors, *Fluid Dynamics in Biology*, volume 141 of *Contemporary Mathematics*, pages 401–420. American Mathematical Society, 2003.

[SRP84] G. R. Spedding, J. M. V. Rayner, and C. J. Pennycuick. Momentum and energy in the wake of a pigeon (columbia livia) in slow flight. *Journal of Experimental Biology*, (111):81–102, 1984.

[SWW96] M. Smith, P. Wilkin, and M. Williams. The advantages of an unsteady panel method in modelling the aerodynamic forces on rigid flapping wings. *The Journal of Experimental Biology*, 199(5):1073–1083, 1996.

[TD96] Bret W. Tobalske and Kenneth P Dial. Flight kinematic of black-billed magpies and pigeons over a wide range of speeds. *Journal of Experimental Biology*, (199):263–280, 1996.

[THB03] Bret W. Tobalske, Tyson L. Hedrick, and Andrew A. Biewener. Wing kinematcis of avian flight across speeds. *Journal of avian biology*, (34):177–184, 2003.

[TNT03] Graham K. Taylor, Robert L Nudds, and Adrian L. R. Thomas. Flying and swimming animals cruise at a strouhal number tuned for high power efficiency. *Nature*, 425(6959):707–711, 2003.

[Tob07] Bret W. Tobalske. Biomechanics of bird flight. *The Journal of Experimental Biology*, 210(18):3135–3146, 2007.

[UE02] James R. Usherwood and Charles P. Ellington. The aerodynamics of revolving wings ii: Propeller force coefficients from mayfly to quail. *Journal of Experimental Biology*, 205:1565–1576, 2002.

[UHB03] James R. Usherwood, Tyson L. Hedrick, and Andrew A. Biewener. The aerodynamics of avian take-off from direct pressure measurements in Canada geese (*Branta canadensis*). *The Journal of Experimental Biology*, 206(22):4051–4056, 2003.

[UHMB05] James R. Usherwood, Tyson L. Hedrick, Craig P. McGowan, and Andrew A. Biewener. Dynamic pressure maps for wings and tails of pigeons in slow, flapping flight, and their energetic implications. *The Journal of Experimental Biology*, 208(2):355–369, 2005.

[Ush09] James R. Usherwood. The aerodynamic forces and pressure distribution of a revolving pigeon wing. *Experiments in Fluids*, 46(5):991–1003, 2009.

[Wan07] Jeffrey M. Wang. Animating the ivory-billed woodpecker. Master's thesis, Cornell University, 2007.

[WBD04] Z. Jane Wang, James M. Birch, and Michael H. Dickinson. Unsteady forces and flows in low reynolds number hovering flight: two-dimensional computations vs robotic wing experiments. *Journal of Experimental Biology*, 207:449–460, 2004.

[WBL+08] Jeffrey M. Wang, Kimberly Bostwick, Martjan Lammertink, John Fitzpatrick, Fola Akinola, Daniel Lepage, and Donald P. Greenberg. Pattern matching an ivory-billed woodpecker model to single view video footage. Work in Progress, Cornell University, 2008.

[WF72] Torkel Weis-Fogh. Energetics of hovering flight in hummingbirds and in drosophila. *Journal of Experimental Biology*, 56:79–104, 1972.

[WF73] Torkel Weis-Fogh. Quick estimates of flight fitness in hovering animals, including novel mechanisms for lift production. *Journal of Experimental Biology*, 59:169–230, 1973.

[Whi02] Frank M. White. *Fluid Mechanics*. McGraw-Hill, 5th edition, 2002.

[Wit81] Philip C. Withers. An aerodynamic analysis of bird wings as fixed airfoils. *Journal of Experimental Biology*, 90:143–162, 1981.

[WP03] Jia-chi Wu and Zoran Popović. Realistic modeling of bird flight animations. In *SIGGRAPH '03: ACM SIGGRAPH 2003 Papers*, pages 888–895, New York, NY, USA, 2003. ACM.

[WS84] A. J. Ward-Smith. *Biophysical aerodynamics and the natural environment*. Wiley, 1984.